CHALMERS

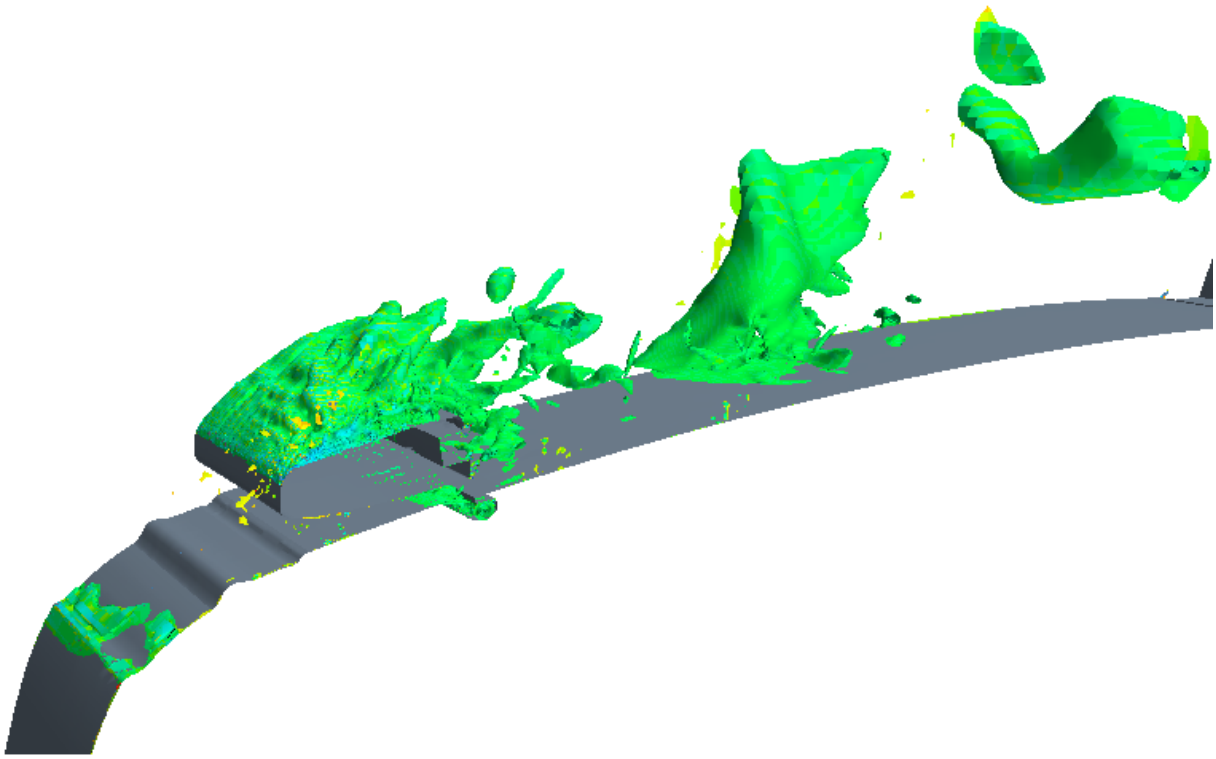

Aeroacoustic study on roof bow

CFD generation of input data for hybrid approach

Master's thesis in Solid and Fluid Mechanics

JOHAN TELL

Department of Applied Mechanics
Division of Fluid Dynamics
CHALMERS UNIVERSITY OF TECHNOLOGY
Gothenburg, Sweden 2012
Master's thesis 2012:56

MASTER'S THESIS IN SOLID AND FLUID MECHANICS

Aeroacoustic study on roof bow

CFD generation of input data for hybrid approach

JOHAN TELL

Department of Applied Mechanics
Division of Fluid Dynamics
CHALMERS UNIVERSITY OF TECHNOLOGY

Gothenburg, Sweden 2012

Aeroacoustic study on roof bow
CFD generation of input data for hybrid approach
JOHAN TELL

Master's thesis 2012:56
ISSN 1652-8557
Department of Applied Mechanics
Division of Fluid Dynamics
Chalmers University of Technology
SE-412 96 Gothenburg
Sweden
Telephone: +46 (0)31-772 1000

Cover:
Total pressure on iso surfaces on top of a 150[mm] slice of a truck cabin

Chalmers Reproservice
Gothenburg, Sweden 2012

Aeroacoustic study on roof bow
CFD generation of input data for hybrid approach
Master's thesis in Solid and Fluid Mechanics
JOHAN TELL
Department of Applied Mechanics
Division of Fluid Dynamics
Chalmers University of Technology

Abstract

Aeroacoustics means noise induced by flow, which is a growing field of interest in todays automotive industry. This study was carried out at Volvo Group Trucks Technology with the purpose to learn about the aeroacoustics around a roof bow in combination with cavities as well as looking into methodologies.

This Master's thesis is focused on the first part of a two step hybrid approach for noise simulation, meaning to simulate the flow using computational fluid dynamics (CFD). Both stationary and transient simulations with aeroacoustic treatment were performed. Different turbulence models such as large eddy simulations (LES), detached eddy simulations (DES) and unsteady Reynolds averaged Navier Stokes (URANS) were tested. Acoustic sources were looked upon with help of acoustical analogies such as Curle and Proudman, both derived from Lighthill's analogies.

It was realized that the bow studied introduces broad banded noise, which could be related to its shedding frequency. Also the cavities seemed to produce broad banded noise, particularly at higher frequencies. The results reveals that LES is costly and requires approximately twice the computation time of DES and a considerably denser mesh.

Keywords: Aeroacoustics, CFD, hybrid approach, LES, DES, URANS, Truck, cavities

Preface

This Master's thesis was carried out as a one semester project at the department of cabin analysis at Volvo Group Trucks Technology (GTT), Gothenburg. The project constitute the authors final part of the master's programme in applied mechanics at Chalmers University of Technology. This thesis is further thought of as a multidisciplinary field where both structural and fluid dynamic knowledge is valuable for communication. *Ph.D.* Zenitha Chronéer, *analysis engineer CFD*, has been the supervisor at Volvo and *Prof.* Lars Davidson at the division of fluid dynamics, department of Applied mechanics at Chalmers the examiner.

Acknowledgements

I am so happy that I was given the possibility to come out in the industry and do such an interesting work. So first of all I would like to direct a great thanks to all them who made it possible and believed in me, no-one mentioned no-one forgotten.
I am heartily thankful to my supervisor Zenitha Chronéer for guiding me throughout the project and opening my eyes for industrial CFD engineering. I would also like to show my largest appreciations to Lars Davidson for beliving in me and for helpful support and thoughts. A jointly gratitude goes to all my collegues at Volvo GTT, Cab Analysis, for their interest in my work and for giving me a great time, not least during coffee breaks. Special thanks for input and discussions in the, for me, unexplored field of acoustics goes to Anders Hedlund, Ulrika Ohlsson, Lars Nordström, Thomas Englund, Fabien Acher and Jonas Klein all at Volvo GTT/Renault Trucks.
My final thanks goes to my family and friends for support and giving me a great time.

Nomenclature

Roman upper letters

A_c	cross-section cavity area
A_n	Neck area
C	Courant number, dimensionless constant
C_d	coefficient of drag
C_{DES}	modelling constant in DES
C_l	coefficient of lift
Ma	Mach number
Re_x	local Reynolds number
$\bar{S}_{ij}$	rate of strain tensor for resolved scales
S^d_{ij}	velocity gradient tensor
St	Strouhal number
T_{ij}	Lighthill tensor
W_{ref}	reference acoustical power
W	acoustical power

Roman lower letters

a	speed of sound
a_∞	ambient speed of sound
c_w	model constant, WALE subgrid model
$f_{Helmholtz}$	Resonance frequency, Helmholtz
$f_{Rossiter}$	Shedding frequency, Rossiter feedback model
$f_{max,steady}$	max gridresolved frequency based on steady data
h_n	height of neck
h_{nl}	length for additional lower mass of Helmholtz neck
h_{nu}	length for additional upper mass of Helmholtz neck
l	longitudinal integral length scale of the velocity
$\tilde{l}_{DES}$	DES length scale
l_0	length of the open cavity
m	number of vortices in the opening
$\mathbf{n}$	outward facing surface normal
p_{static}	static pressure
p_{ij}	compressive stress tensor
p_∞	ambient pressure
r	distance from source to observer
s_n	length of cavity
u_{rms}	root mean square velocity
u_*	friction velocity at nearest wall
u_{vc}	transport velocity of the vortex in the shear layer
u_x	local velocity
$\mathbf{x}$	observer location

y	distance to nearest wall
$\mathbf{y}$	source location
y^+	non-dimensional wall distance

Greek upper letters

$\Delta x, \Delta y, \Delta z$	grid spacings
Δt	time step

Greek lower letters

α	shape constant of longitudinal velocity correlation $f(r)$
δ	Boundary layer thickness
δ_{ij}	Kronecker delta
γ	adiabatic index
γ	empirical constant for a phase shifting vortex initiation
ν	local kinematic viscosity
ω	angular velocity
ρ_{static}	mean density
ρ_∞	ambient density
τ_{ij}	viscous stress tensor

Acronyms

CFD Computational Fluid Dynamics.

DDES Delayed Detached Eddy Simulation.

DES Detached Eddy Simulation.

DFT Discrete Fourier Transform.

DNS Direct Numerical Simulation.

FEM Finite Element Method.

FFT Fast Fourier Transform.

FSI Fluid Structure Interaction.

FT Fourier Transform.

GTT Group Trucks Technology.

IDDES Improved delayed Detached Eddy Simulation.

LES Large Eddy Simulation.

RMS Root Mean Square.

SPL Sound Pressure Level.

URANS Unsteady Reynolds-Averaged Navier-Stokes.

URF Under Relaxation Factor.

WALE Wall-Adapting Local Eddy Viscosity.

Contents

"Just as a stone flung into the water becomes the centre and cause of many circles, and as sound diffuses itself in circles in the air; so any object, placed in the luminous atmosphere, diffuses itself in circles, and fills the surrounding air with infinite images of itself."
-Leonardo da Vinci
Quoted in Irma A Richter (ed) Selections from the Notebooks of Leonardo da Vinci (1977).

1 Introduction

Today's truck and car manufacturers constantly strive for a more quiet and comfortable occupant environment. Techniques for reducing flow-induced noise has become more important than ever, simulations of it becomes even more popular with today's increasing computer capacities. They have come a long way in the right direction but there is still room for improvements. A lot of parameters have to be considered when designing vehicles, if they can be simulated on forehand it would be a great advantage and maybe save some money from testing and expensive late design changes.

Back in the 1970s Stapleford & Carr [53] sorted this flow-induced noise into:

- Unpitched noise caused by air rushing past the vehicle exterior
- Monotone noise caused by sharp edges and gaps on the exterior of the vehicle
- Acoustic resonance directly influencing the compartment noise level caused by flow excitation of openings in the vehicle, such as side windows and sunroof.

The first point in this list, also referred to as *air-rush noise*, generates a broad banded noise[1] and makes considerably impact on sealed bodies at speeds above 100[km/h]. This *air-rush-noise* is then divided into two main causes: the *aspiration*, which is leakages for mass transportation and *shape-noise* which is structural noise.

When mounting a roof bow onto a truck cabin an increase in sound pressure level (SPL) at the drivers ear has been observed. This bow which is intended to support extra lights and horns is mounted close to a slot belonging to the roof hatch, see cover picture and fig 3.11.1. This slot is perpendicular to the main flow direction and is assumed to give rise to flow-induced noise, which can be hard to measure without disturbing the flow.

Objective

The aim of this thesis is to investigate the way Volvo Group Trucks Technology (GTT) cab department can analyse the fluid dynamic part of aeroacoustics around a bow and other exterior details and gain some knowledge about flow past cavities.

Delimitations

This project is limited in time to 20 weeks full time studies for one Master of Science student. Focus area is the roof bow region, see fig: 1.0.1. This project will further only deal with flows outside the cabin and far field noise will not be investigated. Just one way Fluid Structure Interaction (FSI) will be performed, meaning no response input from structures (vibrating roof for instance). Computer resources are limited to what Volvo GTT, Gothenburg can afford. No physical testing will be performed, which means that results will be left un-validated.

Focus will be on fluid dynamics which will be simulated with criteria for capturing sound. The sound investigated in this thesis is therefore limited to airbourne sound. Sound and vibration theory and implementations will therefore be shallow.
Only one operating speed (25[m/s]) of a truck in zero yaw will be investigated meaning subsonic conditions. Only one cab type will be regarded: the lower model[2].

Figure 1.0.1: *Roof bow carrying lights on top of a truck. Picture from AB Volvo Groups official gallery, with permission.*

[1] For more info, please visit chapter 2.1.3
[2] See for instance a home page of Volvo Trucks

2 Theory

This theory part is meant to help readers to better understand the results and methodology. Since aeroacoustics is a field joining acoustics and fluid dynamics, presumed readers will be of both disciplines. This theory part will therefore treat little of each, and not go really deep into details, which otherwise would make this theory part unrealistic long. For deeper knowledge readers are referred to corresponding specialist literature.

2.1 Sound

Acoustical sensations can according to [25] be divided into:

- **Sound**: "A disturbance in an elastic medium resulting in an audible sensation. Noise is by definition "unwanted sound" ".
- **Vibration**: "A disturbance in a solid elastic medium which may produce a detectable motion."

These two are often related to each other. For instance a vibrating solid emitting sound through acoustical energy radiation. This acoustical energy can according to [25] simultaneously be described by three properties:

- **Level or magnitude**: Measure of acoustical energy
- **Frequency or spectral content**: Energy as frequency composition.
- **Time or temporal variations**: Describes acoustic energy time dependence.

2.1.1 Sound definitions

Sound pressure is the pressure fluctuation from normal condition in a point. This normal condition is static air and the fluctuation can have several causes, for instance gas transportation. Instant sound pressure is therefore time dependent variations in total pressure as:

$$p_{tot}(t) = p(t) + p_{static}(t) \tag{2.1.1}$$

Both parts at RHS of (2.1.1) are as seen time depent, but the variations in p_{static} are much slower and therefore often regarded as a constant. For the effective sound pressure a Root Mean Square (RMS) value is used.
The speed of sound, a, is dependent of the media in which it spreads according to:

$$\mathrm{a} = \sqrt{\frac{\gamma p_{static}}{\rho_{static}}} \tag{2.1.2}$$

where: p_{static} is the static pressure , ρ_{static}: mean density and γ the adiabatic index[1] defined as the ratio of specific heats: $\frac{c_p}{c_v}$. According to [32] the speed of sound is "the rate of propagation of a pressure pulse of infinitesimal strength through a still fluid." At ground level in 20°C the speed of sound is around 340[m/s]. The dimensionless Mach number is defined as the ratio between the actual speed, v, and the local speed of sound as:

$$Ma = \frac{v}{\mathrm{a}} \tag{2.1.3}$$

2.1.2 What is vortex sound

M. S. Howe [31] defines vortex sound as "The sound produced as a by-product of unsteady fluid motions. It is part of the more general subject of aerodynamic sound." Aerodynamic sound is a wider subject that includes for example jet engines, explosions, combustions, conventional loudspeakers and so forth.

[1] * also known as heat capacity ratio

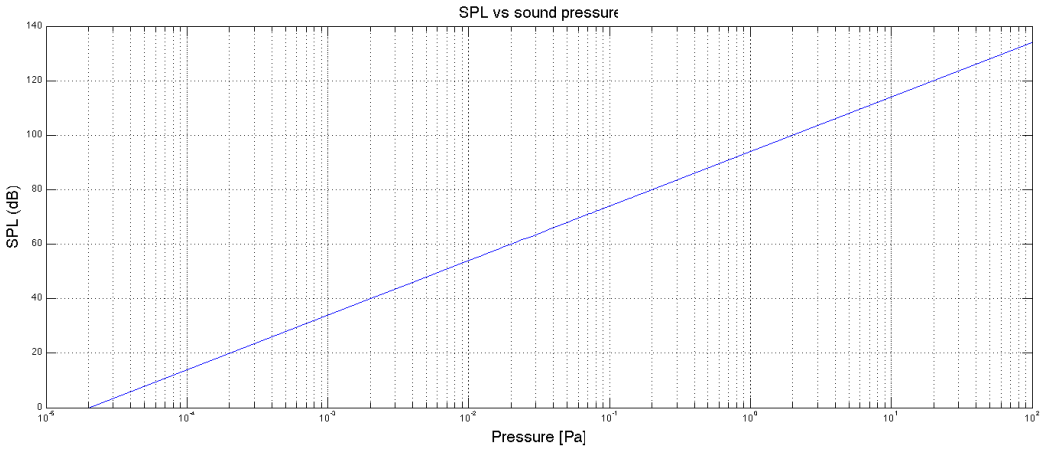

Figure 2.1.1: *Sound pressure level vs pressure*

2.1.3 Basic acoustics

There are some different ways to describe and quantify acoustics, presented here are some of them used in this thesis.
Broad band: When mentioning broad band noise, one have in mind a continuous spectrum where the acoustic energy is spread at all frequencies in a certain wide range.
Narrow band: Opposed to broad band noise, the acoustic energy in a narrow band is distributed in a relatively small section in the frequency range.

The spectrum that can be heard by human ears lies within roughly 20-20000[Hz] [36].

Levels in acoustics are often presented using the decibel scale, dB. This is a measure that logarithmically expresses the ratio of power as [37]:

$$dB = 10 \cdot \log_{10}\left(\frac{P_1}{P_2}\right) \tag{2.1.4}$$

where P_2 is the absolute value of the reference power and P_1 the absolute value of the evaluated value[2]. So dB is actually not a unit, it is just a *level* which tells you how far away from the reference state you are. Please also note the logarithmic scaling!

Sound pressure level (SPL) quantifies what people hear. Sound Pressure Level (SPL) is (2.1.4) customized to pressures as:

$$SPL = 10 \cdot \log_{10}\left[\left(\frac{p^{rms}}{p_{ref}}\right)^2\right] = 20 \cdot \log_{10}\left[\left(\frac{p^{rms}}{p_{ref}}\right)\right] \tag{2.1.5}$$

where p_{ref} is the reference pressure and p^{rms} is the measured root mean square value. The reason why it's squared is that pressures squared are proportional to power, which is desirable. The reference pressure, p_{ref}, is often set to $20 \cdot 10^{-6}$[Pa] for air, which is the lower threshold for human hearing. This threshold will result in a unity ratio and thereby a level of 0dB. To give an idea about how small the pressure deviations are (compared to standard atmospheric pressure $101.325k$[Pa]) and the logarithmic behaviour, (2.1.5) is visualized in fig. 2.1.1 on the facing page.

Sound power level Sound power is an absolute measure of the emitted sound energy[3] per second from an acoustical source. The sound power level is defined as [4]:

$$L_W = 10 \log_{10}\left(\frac{W}{W_{ref}}\right) \tag{2.1.6}$$

[2] The evaluated values needs to be of the same units
[3] energy associated with vibrations

where in most countries W_{ref} is taken as 10^{-12}[W], [4].

2.1.4 Monopole, dipole and quadrupole

Hirschberg and Rienstra [26] describes these phenomena in an easy simile using a boat: If **one** person jumps up and down in a boat, there will be an unsteady supply of volume which generates a monopole wave pattern surrounding the boat. Similar to this is the presentation of dipole which can be regarded as **two** people playing with a ball in the same boat. When exchanging the ball it makes the boat oscillate, which gives the dipole wave field around it. Quadrupoles are more irregular and can be seen as **two** people fighting in the boat. This indicates that quadrupoles are less effective in creating waves than the monopoles or dipoles.

2.2 Turbulence modelling

Presented in this section are some ways to treat and model turbulent flow. The models presented are all for unsteady flow purposes. The LES is computationally demanding, but still not as demanding as Direct Numerical Simulation (DNS). This thesis deals with walls and high Reynolds numbers. Near walls the eddies get smaller which makes resolvement by LES very computationally demanding. Presented are therefore detached eddy models which treats these boundaries with "cheaper" models and applies LES outside the boundary layers.

2.2.1 Large Eddy Simulation, LES

Large eddy simulation is just as the name reveals, simulation of the large eddies. The idea is to accurately compute the largest turbulent eddies down to a certain cutoff width. The smaller eddies below this cutoff is more isotropic and modelled with subgrid scale models. This gives more accurate results than RANS models and is especially good to use in three-dimensional, unsteady, massively separated flows particularly when sound emissions are of interest [41]. So instead of time averaging, Large Eddy Simulation (LES) make use of filtering the Navier Stokes equations. It then filters out eddies with smaller length scale(associated with higher frequencies) than the cutoff width[4] in the unsteady simulation. The information of the smaller eddies are then lost, and their contribution will instead be described by the SGS model.

The spatial filter function for LES is according to [57] defined as:

$$\bar{\phi}(\mathbf{x},t) = \int_{-\infty}^{\infty}\int_{-\infty}^{\infty}\int_{-\infty}^{\infty} G(\mathbf{x},\mathbf{x}',\Delta)\phi(\mathbf{x}',t)dx_1'dx_2'dx_3' \tag{2.2.1}$$

where:

$$\begin{aligned} G(\mathbf{x},\mathbf{x}',\Delta): &\ \text{filter function} \\ \bar{\phi}(\mathbf{x},t): &\ \text{filtered function}[5] \\ \phi(\mathbf{x},t): &\ \text{unfiltered function} \\ \Delta: &\ \text{filter cutoff width} \end{aligned}$$

Most common filters for LES purposes are [57]: Top-hat(or box filter), Gaussian filter and Spectral cutoff filter.

The cutoff width for three-dimensional meshes is often taken as the cube root of the cell volume, $\Delta = \sqrt[3]{\Delta x \Delta y \Delta z}$ [57].

For the subgrid scales, this thesis uses a Wall-Adapting Local Eddy Viscosity (WALE) subgrid scale model for modelling of the turbulent viscosity μ_t.

For the wall treatment no assumptions are made, since the sublayer is considered to be well resolved. Hence the low y+ treatment in StarCCM+ is chosen.

The WALE subgrid model The WALE subgrid model proposed by [34] is a more advanced model than the Smagorinsky one to model the turbulent viscosity as:

$$\nu_t = (c_w\Delta)^2 \frac{(S_{ij}^d S_{ij}^d)^{3/2}}{(\bar{S}_{ij}\bar{S}_{ij})^{5/2} + (S_{ij}^d S_{ij}^d)^{5/4}} \tag{2.2.2}$$

with the velocity gradient tensor S_{ij}^d defined as:

$$S_{ij}^d = \frac{1}{2}\left(\bar{g}_{ij}^2 + \bar{g}_{ji}^2\right) - \frac{1}{3}\delta_{ij}\bar{g}_{kk}^2 , \qquad \bar{g}_{ij} = \frac{\partial \bar{u}_i}{\partial x_j} \tag{2.2.3}$$

[4] Can be compared to a low pass filter in signal processing
[5] note that $^-$ denotes filterspacing and not time average!

and the rate of strain tensor for resolved scales $\bar{S}_{ij}$ as:

$$\bar{S}_{ij} = \frac{1}{2}\left(\frac{\partial \bar{u}_i}{\partial x_j} + \frac{\partial u_j}{\partial x_i}\right) \tag{2.2.4}$$

In (2.2.2) c_w is a model constant and Δ a characteristic length (filterwitdth). According to [34] the *WALE* model should be a further development of the classical Smagorinsky formulation in aspect that it can handle both local strain rates and rotation rates. In case of a wall: the eddy-viscosity will go to zero, it will also go to zero for pure shear movements.

2.2.2 Detached Eddy Simulation, DES

The Detached Eddy Simulation (DES) is a hybrid approach. It models the boundary layer near walls using Reynolds averaged Navier-Stokes (RANS) and applies large eddy simulation (LES) for the unsteady separated regions. For the Spalart-Allmaras one equation model this transition between Spalart-Allmaras model and its LES counterpart, the SGS model, is based on the grid size by help of the DES length scale[6]:

$$\tilde{l}_{DES} = min\left(d_w, C_{DES}\Delta\right) \tag{2.2.5}$$

which then shifts between RANS length scale, d_w, and LES length scale, $C_{DES}\Delta$. d_w is the distance to the closest wall, $C_{DES}\Delta$ is dependent on the grid size as: $\Delta = max\left(\Delta x, \Delta y, \Delta z\right)$ and C_{DES} is a model constant. So when $d_w < (C_{DES}\Delta)$ in (2.2.5) the RANS modelling will be applied and vice versa. From (2.2.5) it can be noticed that the function is independent of the solution.

Improved delayed detached eddy simulation, IDDES

There are some difficulties in determining the subgrid length scale in DES simulations, and there might be problems when the cells are highly anisotropic, as may be the case close to the wall. Further the LES will work fine when the grid size is much smaller than the distance to the nearest wall ($C_{DES}\Delta < d_w$) and the RANS will work fine close to te wall, so there will unfortunately be a region with a mismatch. This mismatch may according to [35] result in a 15 percent to low skin-friction coefficient. So a model that deals with this layer mismatch is proposed by [48]. The idea is somewhat to make a generalization of Delayed Detached Eddy Simulation (DDES) to also be able to treat unsteady turbulent inflow. It will automatically change subgrid length scale, dependent on which conditions that is present, and where you are in the boundary layer. It uses a blending function to combine these two different branches (DDES and WMLES). The interested reader is directed to [48] for formulas and deeper description.

2.2.3 The unsteady Reynolds-Averaged Navier-Stokes, URANS

Unsteady Reynolds-Averaged Navier-Stokes (URANS), also known as transient RANS (TRANS), uses *Reynolds decomposition* [44]. Meaning to decompose into a mean part and a fluctuating part[7].
This will after insertion to instantaneous equations(continuity, momentum) result in the RANS equations (here on incompressible form). The RANS equations are made unsteady through keeping the transient term $\frac{\partial \overline{U_i}}{\partial t}$ during computation.

$$\frac{\partial \overline{U_j}}{\partial x_j} = 0 \tag{2.2.6}$$

$$\left[\frac{\partial \overline{U_i}}{\partial t} + \overline{U_j}\frac{\partial \overline{U_i}}{\partial x_j}\right] = -\frac{1}{\rho}\frac{\partial \overline{P}}{\partial x_i} + \nu\frac{\partial^2 \overline{U_i}}{\partial x_j \partial x_j} - \frac{\partial}{\partial x_j}(\overline{u_i u_j}) \tag{2.2.7}$$

The dependent variables(U, P, $\overline{u_i u_j}$) are besides spatial depence also time-dependent.

[6] This can be extended to other models as well proposed by [3], for instance the $k-\omega$ Menter-SST model, which then applies as $\tilde{l}_{DES} = min(l_{k-\omega}, C_{DES}\Delta$ with $l_{k-\omega} = k^{1/2}/(\beta^*\omega)$

[7]
$$u_i = \bar{u}_i + u_i'$$
$$p = \bar{p} + p'$$

2.3 Boundary layer thickness

The boundary layer thickness, δ, is defined as the height where the flow has reached 99% of the free stream velocity u_∞. Since the flow in this thesis are of high Reynolds numbers, the boundary layer is estimated using flat plate theory for turbulent flow. According to [32] there is no exact solution, but there are some nice empirical model for the eddy viscosity. The formula for turbulent flat plate boundary thickness reads, please see [32] for derivation:

$$\frac{\delta}{x} \approx \frac{0.16}{Re_x^{1/7}} \tag{2.3.1}$$

where the *local Reynolds number* is computed as:

$$Re_x = \frac{Ux}{\nu} \tag{2.3.2}$$

where:

x : distance to plate edge
ν : kinematic viscosity of the fluid
U : characteristic flow speed

Seen from (2.3.1) the boundary layer grows fast with distance x, actually as $x^{\frac{6}{7}}$. Which is way faster than its laminar counterpart which grows as $x^{\frac{1}{2}}$.

2.4 Mesh theory

There are different guidelines depending on what simulation that will be performed.
For wall-resolved large eddy simulations to be accurately resolved the mesh has to follow the recommendation written in [19] saying $y^+ \sim 1$, $s^+ \sim 30$ and $l^+ \sim 100$. Where y^+ is the non-dimensional wall distance defined as: $y^+ = \frac{u_* y}{\nu}$ with u_* as wall friction velocity, y: distance to nearest wall and ν the local kinematic viscosity. In the same way for the wall parallel s^+ and l^+, span wise and lengthwise non-dimensional distance respectively, seen in fig 2.4.1. This will make it possible to capture near-wall turbulent structures in the viscous sublayer and streak processes in the bufferlayer. This resolution requirement is the reason for the extensive cost of large eddy simulations. For DES which uses RANS models in the boundary layer, it will adapt RANS rules. This means that a y^+ below 2 is good and that not much is gained from going below one as well as allowing the wall parallel non-dimensional numbers to be larger than in LES.

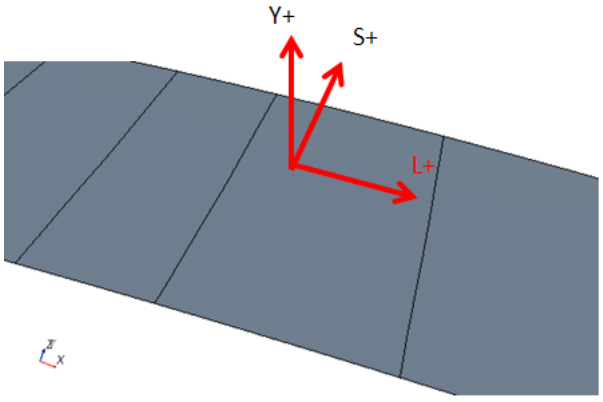

Figure 2.4.1: *Visualization of direction for non-dimensional numbers: y^+, s^+ and l^+*

2.5 Acoustic analogies

An approach for analysing aeroacoustics is to make the assumption that flow and acoustics can be decoupled. In other words: the noise generated by the flow, does not influence the flow. This was pioneered by James Lighthill back in the early 1950s. His idea is to write the governing equations for flow on wave form to combine them with acoustics. Lighthill's analogies laid the foundation for further developments such as Curle's and Proudman's analogies.
As pointed out earlier this thesis focus on the near field, so far field formulations will thereby be omitted.

2.5.1 Lighthill

One idea is to use an analogy from turbulent flow to acoustics, in this case a quadrupole distribution. Lighthill [27] started with the continuity equation for compressible flow [2]:

$$\frac{\partial \rho}{\partial t} + \frac{\partial \rho u_i}{\partial x_i} = 0 \tag{2.5.1}$$

and the momentum equation (conservative form):

$$\frac{\partial \rho u_i}{\partial t} + \frac{\partial \rho u_i u_j}{\partial x_j} = -\frac{\partial p}{\partial x_j} + \frac{\partial \tau_{ij}}{\partial x_j} \tag{2.5.2}$$

with the viscous stress tensor as:

$$\tau_{ij} = \mu \left(\frac{\partial u_i}{\partial x_j} + \frac{\partial u_j}{\partial x_i} - \frac{2}{3} \frac{\partial u_k}{\partial x_k} \delta_{ij} \right) \tag{2.5.3}$$

When taking time derivative of (2.5.1) and subtracting the divergence of (2.5.2) from it one obtains [2]:

$$\frac{\partial^2 \rho}{\partial t^2} - \frac{\partial^2 \rho u_i u_j}{\partial x_i x_j} = -\frac{\partial}{\partial x_i} \left(-\frac{\partial p}{\partial x_j} + \frac{\partial \tau_{ij}}{\partial x_j} \right) \tag{2.5.4}$$

Rearranging (2.5.4) using the chain rule and the Kronecker delta function[8], δ_{ij}, leads to:

$$\frac{\partial^2 \rho}{\partial t^2} = \frac{\partial^2}{\partial x_i \partial x_j} \left(\rho u_i u_j + p\delta_{ij} - \tau_{ij} \right) \tag{2.5.5}$$

further knowing that $a_\infty^2 = \frac{\partial p}{\partial \rho}$ can form:

$$a_\infty^2 \frac{\partial^2 \rho}{\partial x_i^2} - \frac{\partial^2 p \delta_{ij}}{\partial x_i \partial x_j} = 0 \tag{2.5.6}$$

To obtain Lighthill's equation with this one have to subtract (2.5.6) from (2.5.4) [2] to make the inhomogeneous wave equation:

$$\frac{\partial^2 \rho}{\partial t^2} - a_\infty^2 \frac{\partial^2 \rho}{\partial x_i^2} = \frac{\partial^2 T_{ij}}{\partial x_i \partial x_j} \tag{2.5.7}$$

Lighthill's equation (2.5.7) is exact and has the wave operator on the left hand side and the acoustic source term, T_{ij} on the right. T_{ij} is the Lighthill stress tensor, defined as:

$$T_{ij} = \rho u_i u_j - \tau_{ij} + (p - a_\infty^2 \rho)\delta_{ij} \tag{2.5.8}$$

where:

$$\begin{aligned} \tau_{ij} &: \text{describes shear generated sound} \\ \rho u_i u_j &: \text{is the Reynolds stress (or unsteady convection)} \\ (p - a_\infty^2 \rho)\delta_{ij} &: \text{describes the non-linear processes for acoustic generation} \end{aligned}$$

[8] δ_{ij} equals 1 when indices are equal and 0 otherwise

When looking outside the turbulent region the state is assumed to be at rest governed by ambient states ρ_∞, p_∞ and a^2_∞. The acoustics will therefore be represented by fluctuations ($'$) around this state of rest as [2]:

$$\begin{aligned} \rho &= \rho_\infty + \rho' \\ p &= p_\infty + p' \end{aligned} \tag{2.5.9}$$

Described as a homogeneous wave by: $\frac{\partial^2 \rho'}{\partial t^2} - a^2_\infty \frac{\partial^2 p'}{\partial x_i^2} = 0$ makes (2.5.7) able to be written in terms of density fluctuations ($\rho - \rho_\infty$) as the inhomogeneous wave equation [2]:

$$\frac{\partial^2 \rho'}{\partial t^2} - a^2_\infty \frac{\partial^2 \rho'}{\partial x_i^2} = \frac{\partial^2 T_{ij}}{\partial x_i \partial x_j} \tag{2.5.10}$$

where Lighthills stress tensor, T_{ij}, now is converted to:

$$T_{ij} = \rho u_i u_j + (p' - a^2_\infty \rho')\delta_{ij} - \tau_{ij} \tag{2.5.11}$$

So when the two terms describing the wave in the LHS of (2.5.10) are out of balance with each other means that T_{ij} will pulsate, typically in the turbulent area.

Note that Lighthill's equation (2.5.7) is exact (theoretically) but requires that the flow field is known everywhere at all times! So when trying to solve (2.5.7) for an unbounded domain one make use of Greens free-space integration, which make use of retarded times[9] to obtain:

$$\rho'(\mathbf{x}, t) = \frac{1}{4\pi a^2_\infty} \frac{\partial^2}{\partial x_i \partial x_j} \int_V \underbrace{\left[\frac{T_{ij}}{r}\right]}_{\text{retarded time}} d\mathbf{y} \tag{2.5.12}$$

where $\mathbf{y}$ is source location and $\mathbf{x}$ observer location. One can see (2.5.12) as four separate source fields infinitely close to each other, summing up to a quadrupole field. Another way to see this is to immediately treat it as distributed quadrupoles. To do this one has to make use of convolution products[10] to change from spatial to time derivatives and obtain Lighthill's integral formulation:

$$\rho'(\mathbf{x}, t) = \frac{1}{4\pi a^2_\infty} \int_V \underbrace{\left[\frac{1}{r} \frac{\partial^2 T_{ij}}{\partial y_i \partial y_j}\right]}_{\text{retarded time}} d\mathbf{y} \tag{2.5.13}$$

For clarification it may be mentioned that Lighthill's equations presented above will not be solved for, they are presented to understand the foundation of analogies in upcoming sections.

2.5.2 Curle

Curle's analogy [15] is a further development of Lighthill's analogies which introduces and deals with solid boundaries. The way this is done is to set up several mathematical control surfaces that is deformed to coincide with the actual surface. Lighthill's inhomogeneous wave equation (2.5.7) can be treated with general theories such as the Kirchoff formula from for instance [55] to form:

$$\rho' = \rho - \rho_0 = \frac{1}{4\pi a^2_\infty} \int_V \frac{\partial^2 T_{ij}}{\partial y_i \partial y_j} \frac{d\mathbf{y}}{|\mathbf{x} - \mathbf{y}|} + \frac{1}{4\pi} \int_S \left\{ \frac{1}{r} \frac{\partial \rho}{\partial n} + \frac{1}{r^2} \frac{\partial r}{\partial n} \rho + \frac{1}{a_\infty r} \frac{\partial r}{\partial n} \frac{\partial \rho}{\partial t} \right\} dS(\mathbf{y}) \tag{2.5.14}$$

Please note that the equation is evaluated at retarded time[11] and that the distance, r, is calcualted as $|\mathbf{x} - \mathbf{y}|$. So if one omits the surface term in (2.5.14), in other word: disregard solid surfaces, one will end up with Lighthill's integral formulation (2.5.13). By applying the divergence theorem twice on the volume intregral

[9] evaluated at $t - \frac{|\mathbf{x}-\mathbf{y}|}{a_\infty}$

[10] convolution is also know as "faltung" which is german for folding

[11] retarded time:$t - \frac{r}{a_\infty}$

of (2.5.14), transforming the surface part, see [16] for derivation, assuming fixed boundaries (or at least not moving in their normal directions) and substituting for T_{ij} one end up with [16]:

$$\rho - \rho_0 = \frac{1}{4\pi a_\infty^2}\frac{\partial^2}{\partial x_i \partial x_j}\int_V \frac{T_{ij}\left(\mathbf{y}, t - \frac{r}{a_\infty}\right)}{r} d\mathbf{y} - \frac{1}{4\pi a_\infty^2}\frac{\partial}{\partial x_i}\int_S \frac{P_i\left(\mathbf{y}, t - \frac{r}{a_\infty}\right)}{r} dS(\mathbf{y}) \tag{2.5.15}$$

where

$$P_i = -n_j p_{ij} = -n_j(p\delta_{ij} - \tau_{ij}) \tag{2.5.16}$$

gives Curle's formulation:

$$\rho'(\mathbf{x}, t) = \frac{1}{4\pi a_\infty^2}\frac{\partial^2}{\partial x_i \partial x_j}\int_V \frac{1}{r}\underbrace{[T_{ij}]}_{\text{retarded time}} dV(\mathbf{y}) - \frac{1}{4\pi a_\infty^2}\frac{\partial}{\partial x_i}\int_S \frac{n_j}{r}\underbrace{[p\delta_{ij} - \tau_{ij}]}_{\text{retarded time}} dS(\mathbf{y}) \tag{2.5.17}$$

N. Curle about (2.5.15):

> "In it, the surface integral, representing the modification to Lighthill's theory, is exactly equivalent to the sound generated in a medium at rest by a distribution of dipoles of strength P_i per unit area, and by (2.5.16), P_i is exactly the force per unit area exerted on the fluid by the solid boundaries in the x_i direction. Physically, therefore, one can look upon the sound field as the sum of that generated by a volume distribution of quadrupoles and by a surface distribution of dipoles."

2.5.3 Proudman

Proudman's analogy [43] is also derived from Lighthill's analogies and approximates the sound power from statistically homogeneous and decaying isotropic turbulence, for the case of low Mach number and high Reynolds number. The acoustics is assumed to not give any feedback to the turbulence. From this analogy one can see (in the far field) the noise from a turbulent flow as a volume distribution of acoustical sources (quadrupoles). Proudman [43] found a relationship for the local acoustical power per unit mass as:

$$P = \alpha \frac{u^3}{l}\frac{u^5}{a_0^5} \tag{2.5.18}$$

where:

a_0 : far field speed of sound
u_{rms} : root mean square velocity
α : shape constant of longitudinal velocity correlation f(r)
l : longitudinal integral length scale of the velocity

For the interested reader, Sarkar and Hussaini [52] tried to determine α with help of DNS and found it to be smaller than Proudmans analytical result.

2.6 Flow past cavities

Flow past cavities may give rise to cavity noise. The sound is distinct and the only moving part is the fluid itself, which also acts as the source of sound.

The phenomena described in this thesis will be Helmholtz resonators and Rossiter's model, which both give dominant frequencies but unfortunately no source strengths. Much of this theory is based on the paper of [59].

Helmholtz resonators theory is a method that describes the dominant frequency in flow past cavities, such as for instance flow past open bottles. The resonant frequency of a Helmholtz resonator is described as [59]:

$$f_{Helmholtz} = \frac{a}{2\pi}\sqrt{\frac{A_n}{V \cdot h_n}} \tag{2.6.1}$$

where:

a : speed of sound
A_n : neck area
V : Volume
h_n : neck lenght

When having a short neck, like in this thesis (approximated as the thickness of the hatch), the mass of the air beneath the neck will move and therefore have a certain momentum. Mass can not be neglected in this case and is therefore included as [59]:

$$f_{Helmholtz} = \frac{a}{2\pi}\sqrt{\frac{s_n}{A_c \cdot (h_{nu} + h_n + h_{nl})}} \tag{2.6.2}$$

where $(h_{nu} + h_n + h_{nl})$ can be approximated by: $h_n + \frac{\pi}{2}s_n$ where s_n is the length of the opening, A_c, the cross-section cavity area and h_n is height of neck according to fig 2.6.1. Unfortunately (2.6.2) will only give the frequency, not the amplitude nor the radiation.

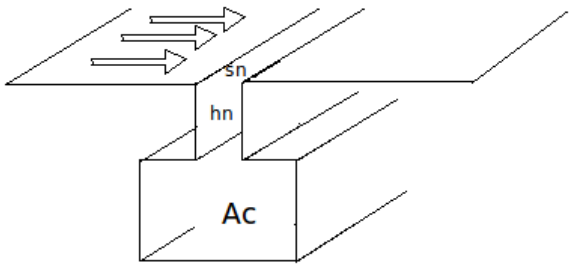

Figure 2.6.1: *Schematic figure of Helmholtz resonator in 2D, delineated from [59]*

Rossiter's model for periodic vortex shedding is a model that is not dependent on low Mach numbers [46]. It uses the time it takes for a vortex to pass the cavity opening plus the time for the pressure pulse to travel back from trailing edge to leading edge with sonic speed. The pressure wave returns which induces a new shedding, see fig 2.6.2. This Rossiter's vortex shedding frequency is calculated as [59]:

$$f_{rossiter} = \frac{U_\infty (m - \gamma)}{l_0 \left(\frac{U_\infty}{u_{vc}} + Ma\right)} \tag{2.6.3}$$

where:

m : number of vortices in the opening
γ : empirical constant for a phase shifting vortex initiation
u_{vc} : transport velocity of the vortex in the shear layer
Ma : Mach number
l_0 : length of the open cavity

In this thesis the cavity length is considered short and the time for pressure waves to return (at sonic speed) is therefore neglected, simplifying (2.6.3) to [59]:

$$f = \frac{u_{vc} \cdot (m - \gamma)}{l_0} \tag{2.6.4}$$

Brennberger [7] found out during his sun-roof buffeting investigation that γ usually is zero. Rossiter's model will in similarity with the Helmholtz model not give any predictions of strength of the source.

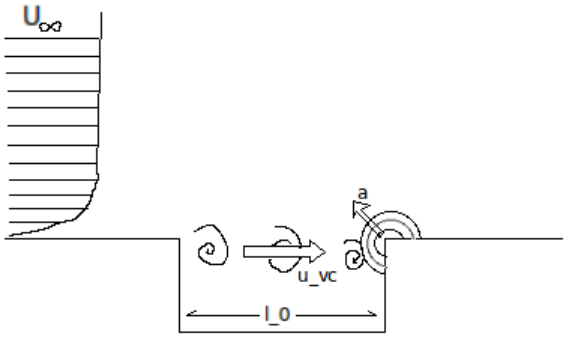

Figure 2.6.2: *Schematic figure of Rossiter's feedback model in 2 dimensions, delineated from [59].*

2.7 Mesh Frequency Cutoff

The mesh frequency cutoff function is a tool in Star CCM+ that tries to predict the frequencies resolved by the mesh in transient simulations. It uses turbulent kinetic energy and mesh properties from steady state simulation to approximately calculate the influence of the local grid size, Δ. According to [58, chapter 6.8] the smallest captured turbulent length scale is twice the cell dimension given the local turbulent kinetic enery, k. The isotropic fluctuation velocity at this place is described by: $\sqrt{\frac{2}{3}k}$. The maximum frequency ($[1/s]$) corresponding to these data can be calculated as [58, chapter 6.8]: $f_{max,steady} = \sqrt{(2/3)k}/2\Delta$.

2.8 Fourier transform

Fourier transform is a mathematical way to convert a time signal into its amplitude and phase (frequency components). It is defined in one dimension as [47]:

$$F(\omega) = \hat{f}(\omega) = \int_{-\infty}^{\infty} f(t) e^{-i\omega t} dt \tag{2.8.1}$$

Assuming that $f(t)$ is piece-wise differentiable and absolutely integrable on the inteval $-\infty < t < \infty$.
Fast Fourier Transform (FFT) is an efficient way of calculating the Discrete Fourier Transform (DFT) well suited for computer algorithms.

2.9 Non-dimensional numbers

Non-dimensional numbers can be great to quantify and give guidelines. Presented here are the Courant number and the Strouhal number.

The Courant number is a measure of how many times the flow passes through the cell each time step[12]. It is defined in one dimension as [50]:

$$\Delta t \frac{u_x}{\Delta x} = C \tag{2.9.1}$$

where:

Δt : time step
u_x : local velocity
Δx : local grid size
C : Courant number, dimensionless constant

The higher values that can be used will give faster solutions. Local Courant values above unity means that the flow passes more than one cell at that location. This put a heavy restriction on the allowable time step. Seen from (2.9.1), a decrease in cell size will increase the Courant number.

Strouhal number The Strouhal number describes oscillating flows, and is calculated as [32]:

$$St = \frac{\omega L}{U} \tag{2.9.2}$$

where:

ω : angular velocity[13]
L : Characteristic size of body
U : Free Stream velocity

Strouhal numbers are reported to be around 0.2 for cylinders. The frequency describes here the vortex shedding frequency. So the Strouhal number can be regarded as a ratio of vibration speed and flow velocity.

2.10 Software coupling

This section is more devoted for understanding the later work (if there will be any), namely the second part of the hybrid strategy described under section 3.1 on the next page.
This is how commercial code Actran does it:
The main idea here is to integrate the energies (rather than interpolating them, which might generate errors unless certain care is taken) from CFD cells onto corresponding Finite Element Method (FEM) nodes [13]. For formulas please see [13].

[12] or if you rather want: how many cells that are passed each time step
[13] frequency f could also be used [23]

3 Methodology

Direct Numerical Simulations (DNS) are clearly out of reach due to time and computational effort, so other alternatives are looked into. This industrial case is considered to have a complex geometry, inhomogeneous flow and flow-induced noise radiation, therefore the hybrid approach using LES or DES for noise source estimation is preferred.

3.1 Hybrid approach

In the hybrid approach the sound-generation process and the sound-propagation process are decoupled. The sound-generation process refers to the aerodynamics which is simulated with help of Computational Fluid Dynamics (CFD). These sources found by CFD will then serve as input for the sound-propagation and radiation process handled by FEM-simulations. The supply of different aeroacoustic solvers are limited, noticeable commercial programs are for instance ACTRAN aeroacoustics by *Free Field Technologies* and Vnoise by *Scientific and Technical Software*.

3.2 Workflow

Since these CFD simulations still are considered heavy and time consuming, an efficient way of producing relatively accurate results will be sought for. The work therefore followed the flow chart in fig. 3.2.1. The main idea is to do faster steady calculations with the built-in correlation models [28] to find a good start and set up for the heavy transient calculation. This pre-process is done in order to avoid as many pit falls as possible. The boxes in fig. 3.2.1 will be described more thorough below.

Figure 3.2.1: *Flow chart for this thesis aeroacoustic CFD simulations*

3.3 Domain generation

Make the mesh around the whole cabin highly resolved is desirable, but clearly out of practical reach. A focus region must be decided, fig. 3.3.1 shows a schematic view of this. A complete truck was modelled using a large domain which completely surrounded the truck . Inside this *large* domain a subdomain is made up. The size of this focus region is not obvious and this thesis uses a rule of thumb saying that the width of the domain should be at least two times the height of the object you want to study [17]. In this case the sum of roof bow thickness and duct height. With some safety margin it was decided that the domain would extend 75[mm] from each side of the cabin transversal centerplane. This will hopefully cover all essential flow features. Regarding height and length, the height is regarded as more crucial in this case. Test with lower rectangular shape was done with unsatisfactory results. What happened was that the speed above the air-directioner was increased to unrealistic values (compared with full truck simulation), see fig. 3.3.3 on the next page. The new domain extends to around 4[m] above the cab and can be seen in fig. 3.3.2 on the following page.

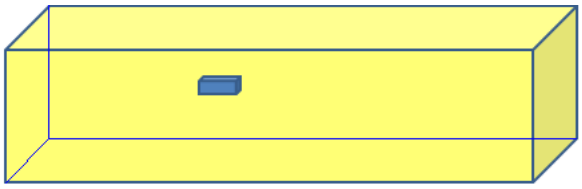

Figure 3.3.1: *Schematic view of domain and subdomain*

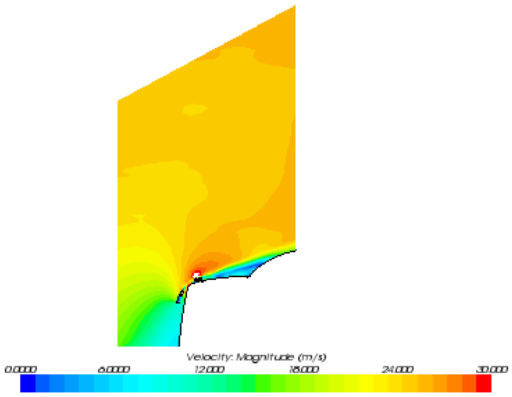

Figure 3.3.2: *Velocity field, New domain*

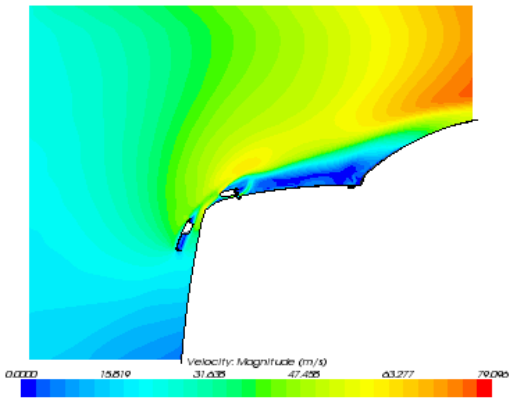

Figure 3.3.3: *Velocity field, Old "low" domain*

Geometry creation

The geometry was cut and cleaned with the commercial program ANSA[1]. In order to make it easer for customization of the mesh in the CFD-program, the surfaces building up the geometry were divided into smaller parts with appropriate names. More exactly 55 pieces, see fig. 3.3.4 where different colors indicate different PIDs. The geometry was exported from ANSA in pro-STAR Shell Input File (.inp)-format. Leakages were sealed to make wrapping work and small unevenesses removed.

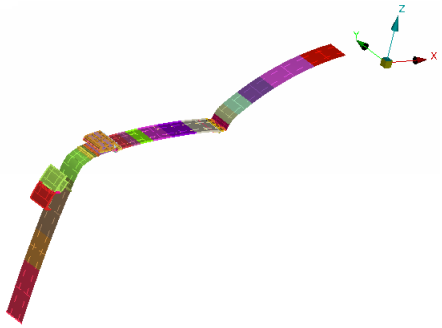

Figure 3.3.4: *Different PIDs marked with different colors in ANSA*

Surface wrapping

The fastest way to get a sealed mesh is to use the surface wrapper tool on the geometry imported as a surface mesh from the .inp-file. There will only be one media (air), so only one region was created and all boundaries belongs to this region. The wrapper was tuned to nicely follow surface curvature and prevent contact between undesired surfaces, with a search floor of around 1[mm]. Surface growth rate was set to 30%. The surface sizes were then customized where it was needed to get the curvature right.

3.4 Boundary conditions

Boundary conditions are crucial for accurate results. Acoustics needs special treatment since reflection of pressure waves in boundaries can give inaccurate results. The target was to simulate a free field surrounding the truck. There are different methods for this, one can for instance have a buffer region which numerically kills these pressure waves and thereby prevents them from coming back. StarCCM+ has a built in free stream boundary condition which is good to use for acoustics, which is then what were used in this thesis. It is recommended that the boundaries are far away with almost no gradients. The domain in this thesis is not large enough for that (which otherwise would require a complete truck), but free stream would according to

[1] version 13.2.1 by *Beta CAE systems S.A* [5]

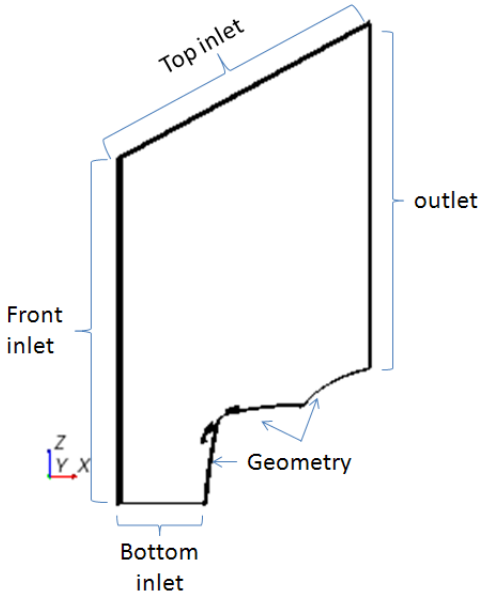

Figure 3.4.1: *View of boundaries, seen from left side*

Table 3.4.1: Boundary conditions

Boundary	Boundary condition type	Mapped
bottom inlet	free stream	✓
front inlet	free stream	✓
top inlet	free stream	✓
right side	free stream	✓
left domain	free stream	✓
outlet	pressure outlet alt free stream	yes, in free stream case
geometry	wall	✘

the software developer support still be the best choice. The boundaries of the subdomain is presented with corresponding names in fig. 3.4.1. The type of boundary used for each one of them is presented in table 3.4.1, please note the sides as well. The simulation is of a truck travelling in 90[km/h]=25[m/s], so the inlet of the *large domain* is then set to homogenous velocity inlet 25[m/s] in longitudinal direction, no yaw or pitch. The outlet for the *large domain* is a pressure outlet with zero gauge.

Boundary condition mapping First attempt was only mapping the front inlet, while the longitudinal sides and top inlet were set to symmetrical boundaries and outlet to a pressure outlet. It was then realized that symmetrical boundaries do not let mass through, meaning that as a consequence of continuity, flow had to compensate with higher mass flow (thereby flow speed) at the outlet. Next approach was to map even more boundaries, but still keeping in mind that the flow eventually could be over-prescribed if all faces (except wall) were mapped. So the outlet was first set to a pressure outlet with zero gauge. Later it was also tested to put a mapped free stream boundary condition on the outlet as well, table 3.4.1. Please see results chapter (4.5) for comparison and table 3.4.1 for final boundary conditions.

The free stream boundaries were fed with data mapped on surfaces from full truck simulations. The data from this full truck simulation was mapped in StarCCM+ on stereo-lithography (stl) faces imported from ANSA. The mapped data output format is comma separated values (csv)-files. Important is of course to use the same surfaces in both the *full* simulation and *part* simulation and to keep track of the units! The data mapped is presented in table 3.4.2 on the current page.

Table 3.4.2: Mapped values

mapped	unit
velocity (i,j,k) and velocity magnitude	[m/s]
turbulent dissipation rate	–
turbulent kinetic energy	[J/kg]
pressure	[Pa]
temperature	[K]
Mach number	–
location (X,Y,Z)	[m]

Note: The reason for exporting both velocity and Mach number is that no other way of defining flow direction in than taking the velocity vector was found.

3.5 Mesh generation

At first a relatively coarse mesh was generated, following ordinary RANS recommendations. A steady state simulation was ran on this mesh to find further improvement regions and then conversion to more acoustic requirements took place, see section 3.6 for more info.

The CFD program used does not provide any measure of s^+ and l^+ neither a function for tabulating cell edge sizes. So the way this was done was the hard way. A spread sheet was tailored to make a table of non-dimensional values, the u_* values were read from a centered[2] planar scalar scene in StarCCM+. The mesh should follow the recommendation of at least 20 cells per acoustical wave length when using higher order schemes [28, 56]. $\lambda = \frac{a}{f}, \Delta = \frac{\lambda}{20} = \frac{\frac{a}{f}}{20}$, which then explicitly says that a frequency of 6 000[Hz] requires $\Delta \leq 2.9$[mm].One can of course also make use of the built-in cut off frequency field function (section 2.7 on page 13) to estimate cell sizes, fig. 3.6.3. This at the same time as following best practice aerodynamics, meaning smooth separations.

DES mesh For the DES mesh generation Spalarts guidelines [51] were used. The domain was therefore divided into fictitious regions that should obey different rules. These regions are described in table 3.5.1 and pointed out in fig. 3.5.1 on the facing page.

Tools To form regions of higher density mesh (typically wakes) the trimmer wake refinement-tool in StarCCM+ was used. The volume-shape tool in cooperation with volumetric control was used to change the aspect ratios of the cells. From fig. 3.5.3 one can see the difference in boundary layer resolution at the front of the bow for DES and LES. As seen from the same figure, the cell width in DES mesh is approximately 16 times wider than LES case. It should be pointed out that this is one of the worst areas though, located at the top front of the bow. In the same figure regions with larger cells can also be seen, it should be mentioned that these cells are still very small.

Cheating During the mesh generation of the LES-grid it was realized that doing fully wall resolved boundary layer along the whole wall-boundary part would cost an awfully lot. An attempt resulting in about 30 million cells was done. It was therefore decided that areas with presumed separation and thereby much large scale turbulence, should be coarsened. To try find out where separation may occur u_* were checked along the geometry surfaces. Further the slots with their inner tongues required a lot of cells. The inner tongues were thereby cut in both front and rear slot, according to fig. 3.5.4. This single action saved about 10 million cells. When looking into (2.6.2) this slightly smaller cross section area, A_c, means that one could expect a somewhat higher resonance frequency. To avoid simulating the flow under the air-directioner, the gap between the roof and the air-directioner was sealed.

[2] middle of domain in longitudinal direction

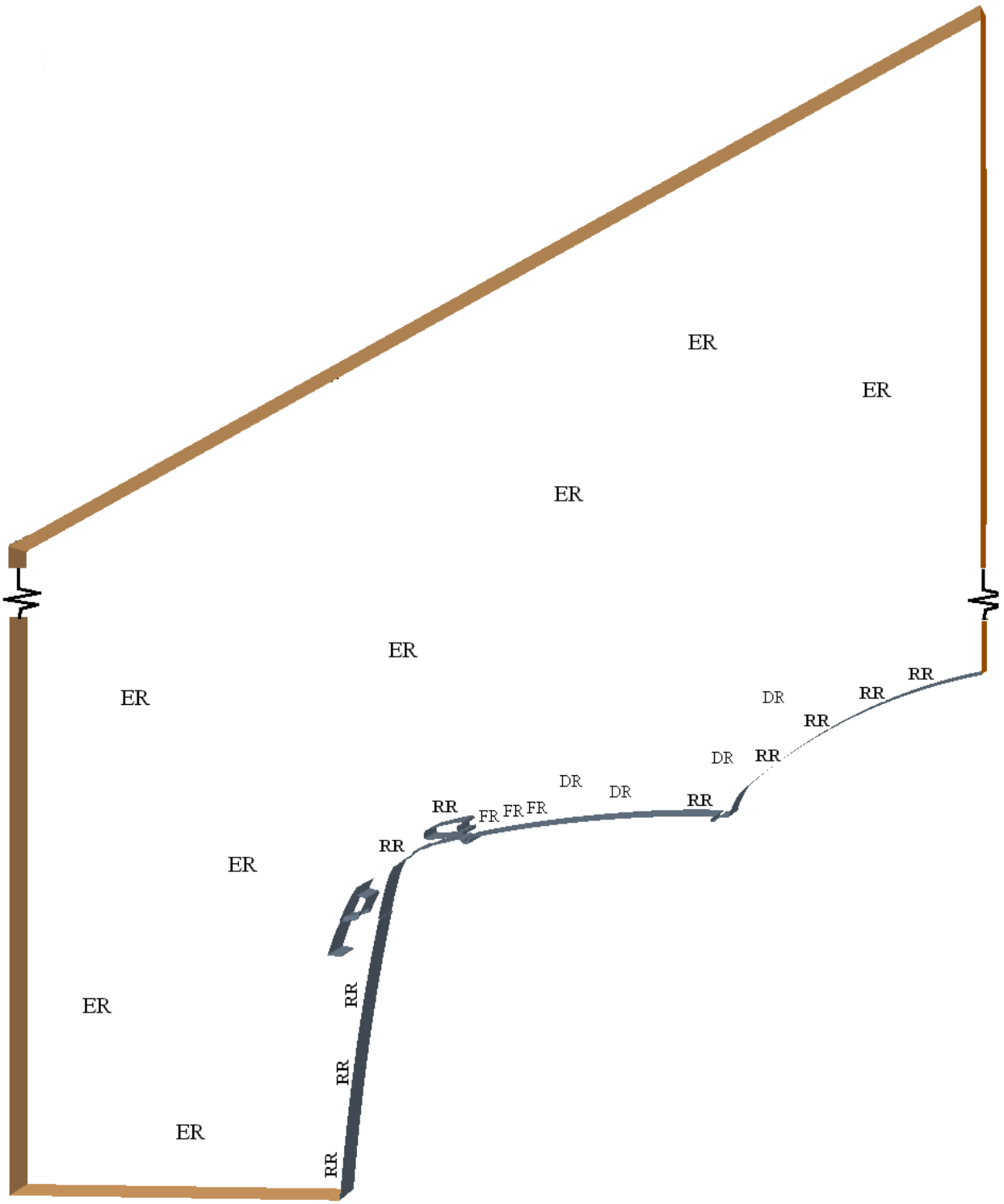

Figure 3.5.1: *Applied DES mesh layout, note that the domain is lowered (broken) in this picture to make room for important regions.*

Table 3.5.1: Mesh regions

Region	Characteristics/treatment
ER: Euler region	Does not hold turbulence, coarse and almost isotropic mesh covering large volumes but with a small share of the gridpoints.
RR: RANS region	Boundary layer, apply RANS rules
VR: Viscous region	Both in RANS and LES mode. y^+ ∼2 or less and a streching of ∼ 25%, unrestricted in wall plane units.
OR: Outer region	Wall normal spacing is set to 10% of boundary layer thickness. Boundary layer thickness can safely be overestimated, out to Euler region. To be on the "right" side.
FR: Focus region	Where the flow is turbulent and needs to be well resolved, put a grid spacing Δ and keep it throughout FR. Decide how big FR needs to be, i. e. where DR starts. Rule of thumb for start of DR: "can a particle propagate from this point to an important flow region?" For safety: overestimate FR somewhat
DR: Departure region	DR is to make a smooth transition for DES out to ER.

3.6 Steady state

In order to roughly find the acoustic sources steady state simulations were performed. These steady state simulations were ran with aerodynamic solver settings with acoustic add-ons. The settings were then: Reynolds averaged Navier-Stokes, two-layer all y^+ wall treatment, standard $k-\epsilon$ two-layer, coupled energy[3] with broadband noise source for aeroacoustics regarding Curle or Proudman models enabled (one at a time), figs. 3.6.1 and 3.6.2. One has to be aware of that Curle and Proudman models in steady state are based on RANS and therefore miss large eddy behaviour such as vortex sheddings [28]. In this thesis they are used to give a hint of where the mesh should be refined prior to transient simulation. To estimate the frequency resolved by the mesh, a frequency cutoff field function were used, fig. 3.6.3 on page 28 shows an example of such a scene. The mesh contours can be seen and the mesh dependency is linear, meaning a split of cell width into two doubles the resolved frequency [28], for more info please see section 2.7 on page 13.

3.7 Transient

In order to do a spectral analysis of the aeroacoustic sources and acoustics phenomena such as resonance, time accurate simulations has to be done. Since it is not known whether the spectrum is narrow-banded (tones) or broad-banded, turbulence models capable of resolving broad-banded noise are being preferred. Important in LES is to have a well resolved wall layer to capture near-wall pressure gradient separation in a good way for a truck like geometry. In [1, 8] they showed, that unsteady RANS models was not as good as DES in predicting broad-banded noise.

Time advancement The timestep is the time increment of temporal marching, which is important to consider in aeroacoustics. It should be sufficient small to capture frequencies of interest, produce a converging solution and at the same time be as large as possible to speed up the calculations. There are therefore several ways to determine the time step.

Nyquist sampling theorem[4] from signal processing is insufficient for capturing acoustic amplitudes, where

[3] To reach convergence faster the simulations were started with the coupled solver, where energy was coupled. Then switched to segragated solver regarding temperature.

[4] Nyquist sampling theorem also known as Nyquist-Shannons sampling theorem states that a sampling frequency of twice the highest frequency in the signal is necessary to avoid aliasing.

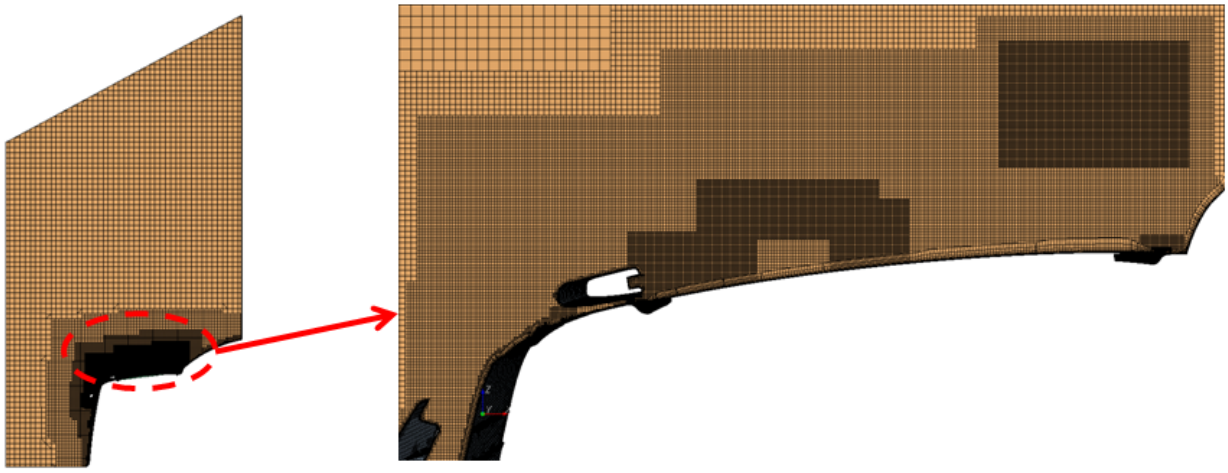

Figure 3.5.2: *DES mesh with bow, assumed source regions have fine mesh while propagation regions have somewhat coarser.*

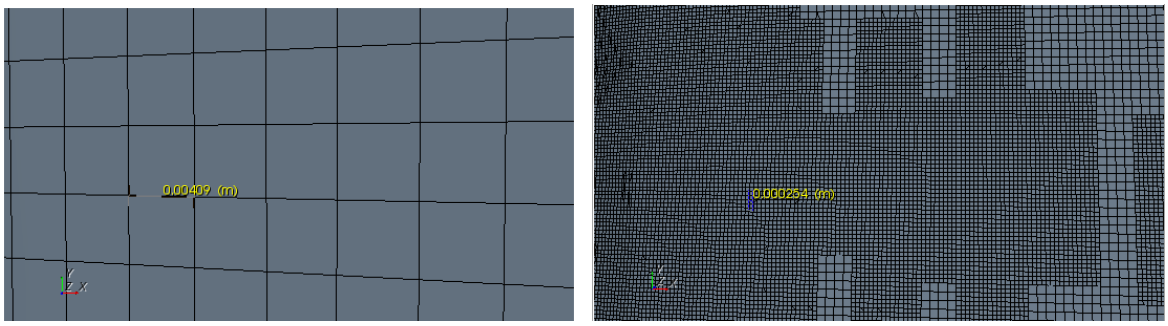

(a) DES mesh (b) LES mesh

Figure 3.5.3: *Difference in cell-size in boundary layer top of bow*

instead around 15 cells (10-20) per wavelength is recommended [10], meaning $\Delta t \leq \frac{1}{15 \cdot f}$. A frequency of 6 000[Hz] then requires $\Delta t \leq 1.1e^{-5}$[s]. This thesis is mainly based on keeping the convective Courant number[5] (2.9.1) below unity which is common and recommended in [30], with frequency resolution in mind. One can also consider other alternatives not presented here. Upon these alternatives one should choose the one requiring the lowest time step, if it is considered worth it.

3.7.1 Total physical time

The total physical time for transient simulations in this thesis is divided into two parts. One part for tune in (for achieving fully developed flow) and one for sampling. The *tune in* phase works as a transition between the steady state and transient simulation. The simulated times in this thesis are estimated using a time scale from free-stream velocity and a length scale as: $T = L/U_{inflow}$. A rule of thumb is then taking 5-10T for tune in and another 5-10T for data sampling [17]. This thesis uses the length of the hatch for L which gives an approximate time of 0.25[s] for tune in and another 0.25[s] for sampling, meaning a total physical time of 0.5[s].

It is hard to judge whether transient flows are tuned in or not. Just looking at pressure plots is hard, since they have a strongly oscillating behaviour. Therefore this thesis **also** uses lift- and drag coefficients, C_l and C_d respectively, for judging convergence. These coefficients are considered more stable and of higher engineering interest.

[5] Note that the convection of acoustic waves is not considered since these spread as $|u| + a$, and therefore almost requires explicit schemes

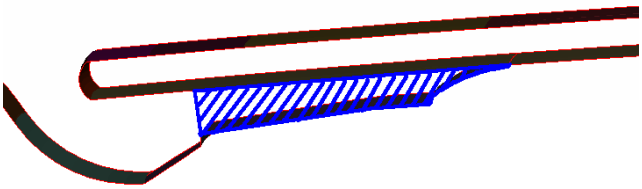

Figure 3.5.4: *The front cavity inner tongue, blue striped area, were removed as a geometry simplification.*

3.7.2 Pit stop

After tune in the recordings were started, meaning setting up new scenes for animation purposes, for example total pressure. The program was then instructed to capture pictures with a certain sampling frequency and export to a certain destination. Depending on frequency resolution of interest and length of sampling period, a resize of captured pictures may be necessary in order to save a lot of disk space.

3.8 Java scripting

When doing repetetive chores it may be a good idea to reduce the time for set-up and risk of forgetting some action by automating the work. StarCCM+ can be instructed by Java scripts, which quite easily can be recorded in the StarCCM+ environment and customized in an editor of your choice. In this thesis macros were used for instance for setting up probes, converting from steady to transient mode, post-processing and to run the cluster.

3.9 Animation creation

Animations were made to visualize the transient behaviour of the flow. These animations are simply pictures captured from a fixed angle with a sampling frequency of every 11^{th} time step during the sampling period, see pit stop section above. These pictures are then piled up with time spacing as a .gif animation using linux command for batch:

```
convert -delay 10 -loop 0 *.png name_of_animation.gif
```

Eventually the pictures first has to be resized using the *mogrify* command in linux. Captured pictures were pics of total pressure and velocity. If one wants to save space and make it easier for movie creation the *ffmpeg*-command in linux can be used to produce for instance .avi files.

3.10 Solver settings

The fluid used in this thesis is compressible air, for specific properties the reader is referred to the material database for air in StarCCM+ Version 6.6.11, [14]. The DES uses Spalart-Allmara's model with 2^{nd} order convection, with coefficients $C_t = 1.63$ and $C_l = 3.55$. A Bounded Central Difference (BCD) scheme[6] is used for the advection since it showed to be the best approach when using DES in the side mirror investigation of [2]. Further in LES it should try to avoid unphysical wiggling effects. The BCD in this thesis uses an upwind blending factor of 0.15.

For the temporal description a 2^{nd} order implicit scheme[7] is used. The timesteps Δt used are presented for each case in table 3.10.1 on the following page. For a more "fail-safe" transitions between RANS and LES in DES, the Improved delayed Detached Eddy Simulation (IDDES) formulation were used. The Under Relaxation Factors (URFs)[8] used are quite high and presented in table 3.10.2 on the next page.

[6] "The bounded central differencing scheme is a composite NVD scheme that consists of a pure central differencing, a blended scheme of the central differencing and the second-order upwind scheme, and the first-order upwind scheme. The first-order scheme is used only when CBC is violated."[24]

[7] according to [24]: $\phi^{n+1} = \frac{4}{3}\phi^n - \frac{1}{3}\phi^{n-1} + \frac{2}{3}\Delta t F\left(\phi^{n+1}\right)$

[8] The under relaxation factor (α) determines how much correction that is added

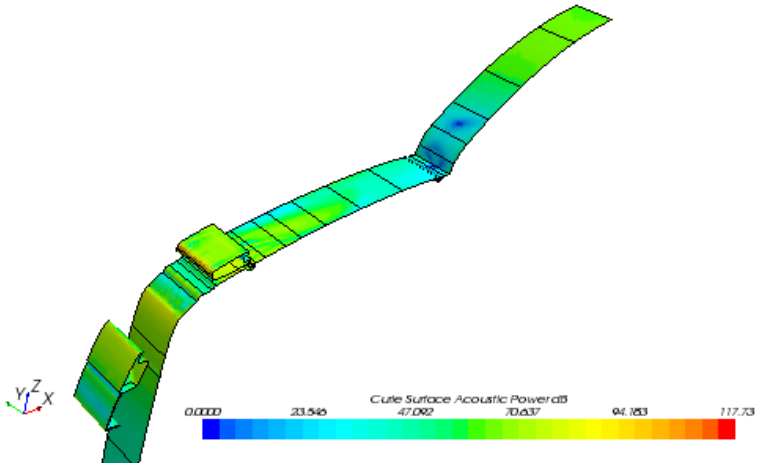

Figure 3.6.1: *Curle shows the acoustical power on surfaces*

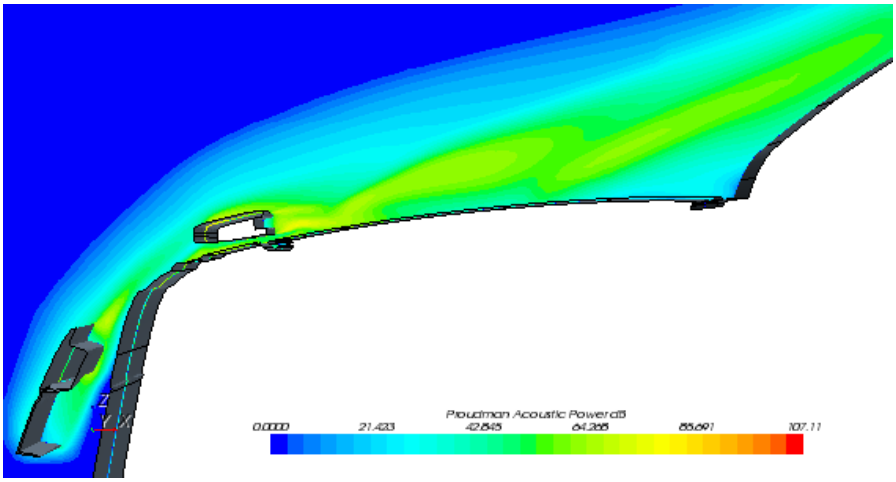

Figure 3.6.2: *Proudman shows the acoustical power in the volume*

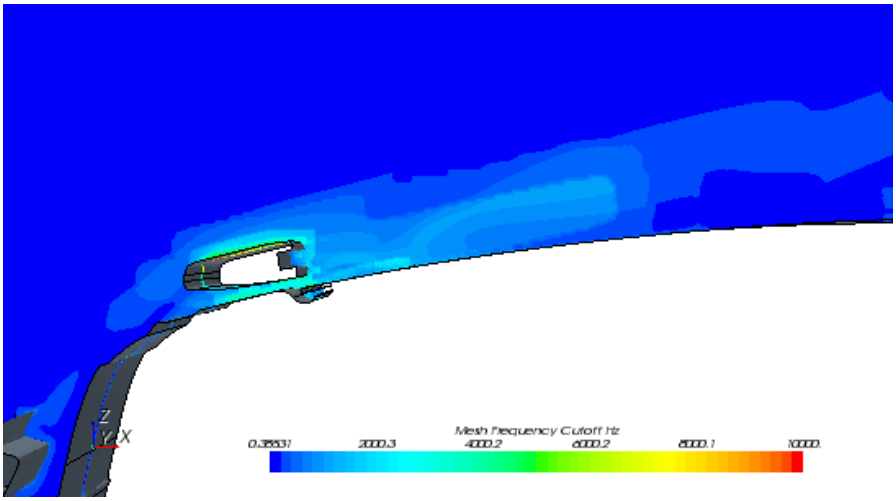

Figure 3.6.3: *Estimated cutoff frequency*

Table 3.10.1: Time steps for different simulations

Simulation	Δt [s]
LES-bow	$1.5 \cdot 10^{-5}$
LES-no bow	$2.0 \cdot 10^{-5}$
DES-bow	$1.5 \cdot 10^{-5}$
DES-no bow, free stream	$2.0 \cdot 10^{-5}$
DES-no bow, pressure outlet	$2.0 \cdot 10^{-5}$
DES-bow, no slots	$2.0 \cdot 10^{-5}$
URANS-bow	$2.0 \cdot 10^{-5}$

Table 3.10.2: Under-relaxation factors for different solvers

	URF, pressure	URF, velocity
LES	0.9	0.95
DES	0.7	0.7

3.11 Probe placement

The probes are positioned where presumed interesting flow phenomena would occur and measurements were performed. These ideas aboout interesting spots are partly influenced by flows around cylinders and side rear view mirrors. Structural interaction and excitations are also interesting to predict in the future, so surface pressure fluctuations are also measured on specific spots. Important here is to get them in the right height in normal direction of the geometry, which would be close to the surface. At least not under it! The distance between the probes on the hatch, seen in fig. 3.11.1, is around 25[cm].

3.12 Average of several probes

Just doing point-wise comparisons is a bit unstable/inaccurate. A better approach would be to spread some points in the region of interest and take a mean of them. This should then be done with great care. Taking the mean of a time signal would mean that it comes with a certain phase as well. When adding these phases they can unfortunately extinguish each other. Take for instance a large amount of stochastically spread numbers and sum them up to receive something close to zero.

So the thing here is to convert them into frequency domain, using for instance FFT. Then do a power mean of them. Do this logarithmically not arithmetically! With the power measure as SPL it will look like:

$$\overline{SPL}(p^2) = 10 \cdot \log_{10}\left(\frac{\bar{p^2}}{(2 \cdot 10^{-5})^2}\right) \tag{3.12.1}$$

where $\bar{p^2}$ for N values is computed as:

$$\bar{p^2} = \frac{\sum\limits_N p_i^2}{N} = \frac{\sum\limits_N 10^{\left(SPL(p_i^2)/10\right)} \cdot (2 \cdot 10^{-5})^2}{N} \tag{3.12.2}$$

This mean will put more "weight" on the higher values since squared. So the mean curve will come with an offset from the amplitude middle in the plot when compared to their values in un-averaged form.

3.13 Exporting data

Exporting solution data to another program is preferably done with a built-in auto-export function. Depending on the required resolution, different settings can be applied, such as the output frequency. In this thesis it is set to each 11^{th} time step. Exported was the volume data for velocity vector and density together with the mesh into a CD-Adapco CCM file(.ccm). One can also just export surface data using the surface fft files (.trn). It

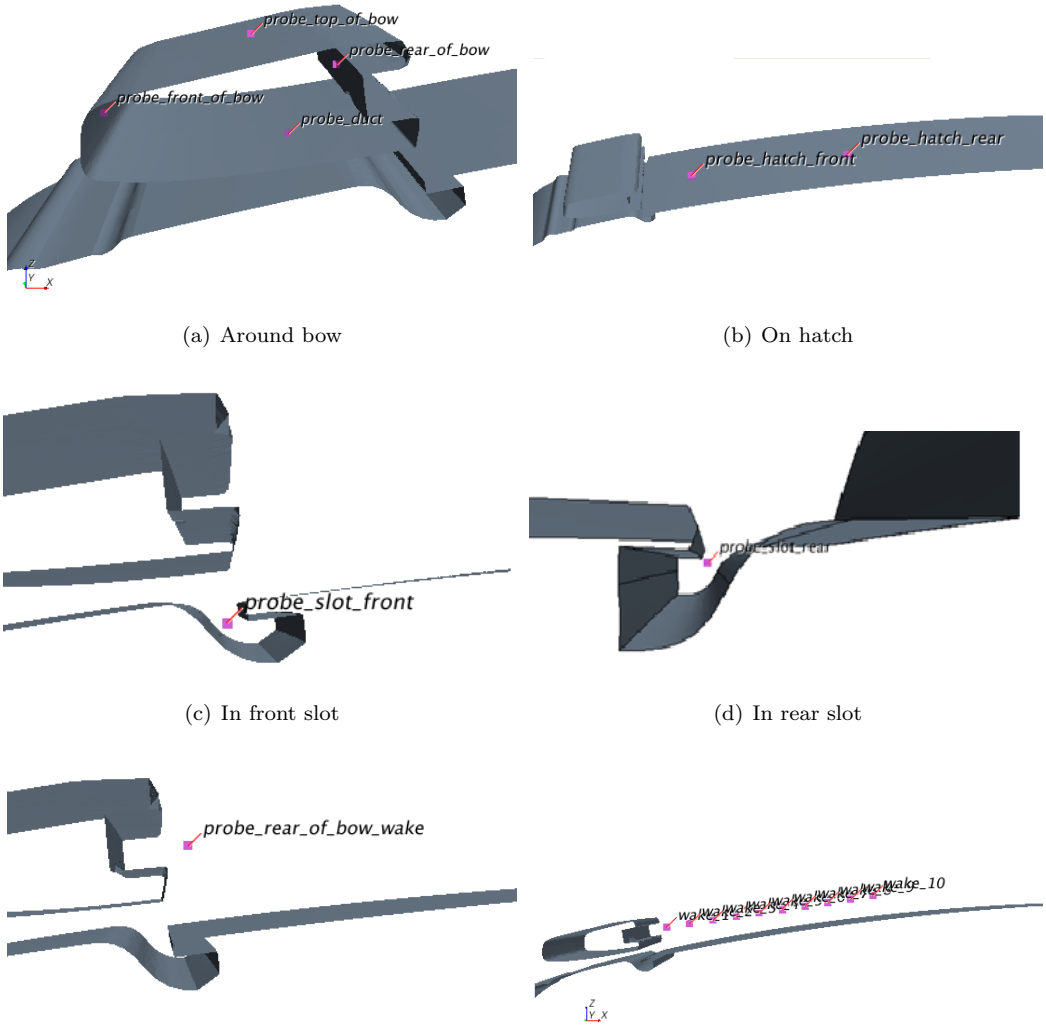

(a) Around bow

(b) On hatch

(c) In front slot

(d) In rear slot

(e) In wake

(f) In wake

Figure 3.11.1: *Pressure probe placements*

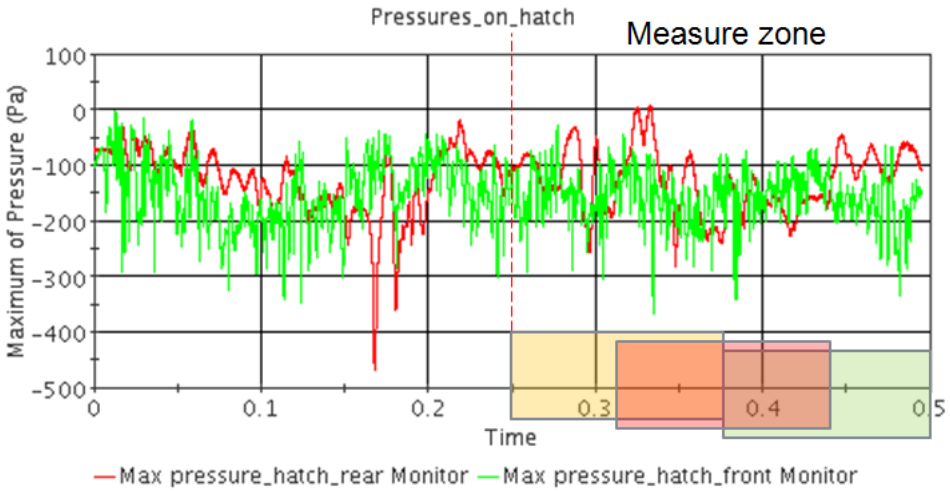

Figure 3.14.1: *Sampling of 2^{nd} half of the simulation and analyzing with 50% overlapping blocks.*

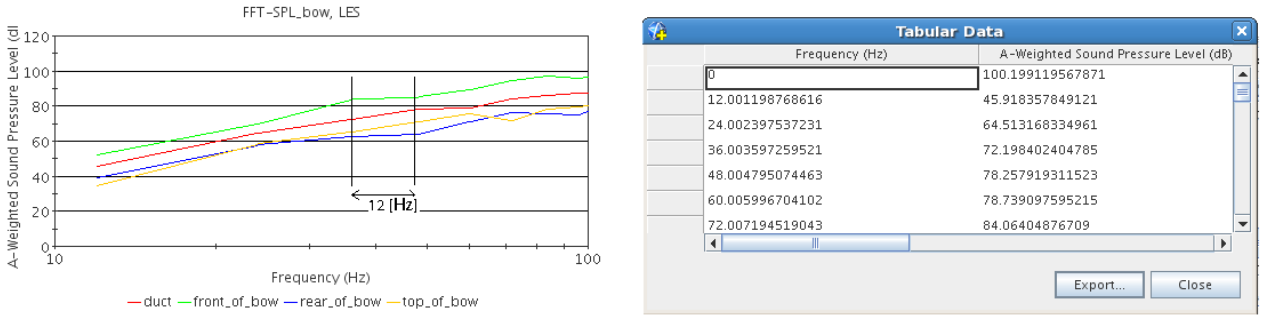

Figure 3.14.2: *Frequency resolution of ∼12[*Hz*]*

may be mentioned though that when exporting was tested, it was realized that it takes a tremendous amount of disk space.

3.14 FFT set up

In this thesis time Fourier transform was used to point-wise analyze the SPL-spectrum at different spots. Time Fourier transform convert time signals to frequency domain, in order to try to find dominant modes in the signals.

How the FFT is set up will influence the results, and thereby the shape of the plots produced. The transient sampling time of 0,25[s] was split up into 3 analysis blocks with 50% overlap according to fig. 3.14.1 on page 30. This corresponds to a frequency resolution of close to 12[Hz][9]. It works like this: when the first buffer has come to the overlap of 50% the second buffer starts to collect. When the first buffer is done it delivers its result to the Fourier Transform (FT) averaging. When the second buffer is done it will also output to FT averaging and so on. FT assumes periodic input, trying to achieve that, window functions are used to try minimize this leakage. Hanning window was chosen in this thesis since it has a good combination of high resolution and dynamic range. The 50% overlap was selected to (try) prevent the Hann window function from introducing too much errors (it is made for constant signals, but these are transients) as well as better utilize the sampling duration. Without overlap the window function multiplying to the time signal would force it to go down to zero at start and end, fig. 3.14.3 and (3.14.1). Meaning you have to await next cycle (box) to capture interesting values[10], meaning longer data acquisition time needed for averaging. The Hanning window function[11] is defined

[9] The number of bins used by FFT must be a multiple of 2
[10] or risk to miss some signatures located at the attenuated part of the window function
[11] Sometimes called Hann window function after Julius Hann (1839-1921)

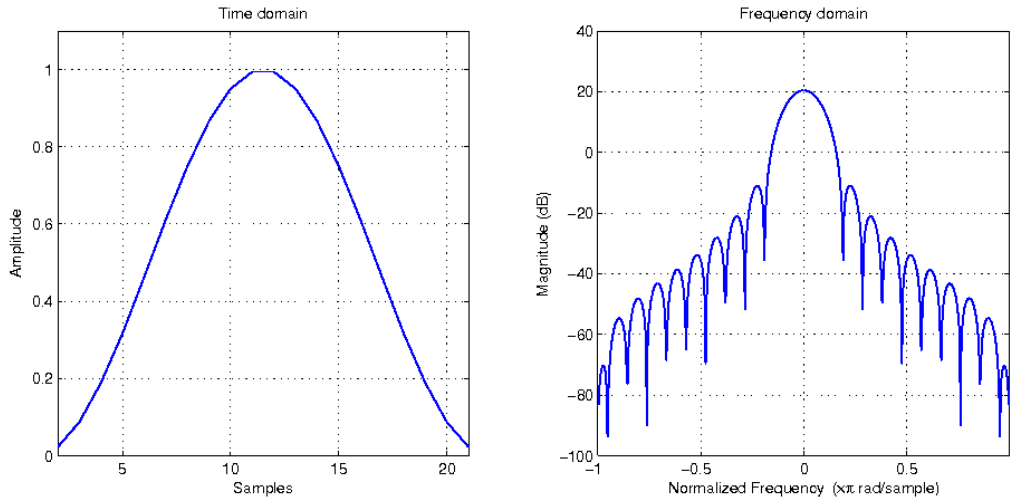

Figure 3.14.3: *Shape of hanning window function in time and fequency domain, 21 samples*

as [39]:

$$\omega(n) = \begin{cases} 0.5 \cdot (1 + \cos\left(\frac{\pi n}{M}\right)), & -M \leq n \leq M \\ 0, & \text{otherwise} \end{cases} \tag{3.14.1}$$

where: $-M \leq n \leq M$ is the time window for the box. From (3.14.1) the window function can be seen as one period of a raised cosine function, meaning it is larger than or equal to zero in its operation region and zero elsewhere (out of M), see fig. 3.14.3. This also means zero slope at the end points (zero-points) which according to [49] means that the discontinuities leaving the region is in the 2^{nd} derivative.

The Fourier transform in this thesis is updated at every time step and the frequency representation is set to just frequency (i.e no octave band) to make it easier to compare with other publications.

The amplitude function is set to A-weighted SPL, since this weighting is common in noise control, regulations and environmental standards. Some may argue that A-weighting is not best representing such high SPL that this thesis deals with, but the future aim is to dampen this SPL through the roof into cabin, where hopefully applicable A-weighting range is present. The "interior" and "exterior" curves will then hopefully have more similar shapes than other exterior sound weighting would give.

3.15 Compressibility

Compressible flow is used to be able to directly capture the interaction between the expected periodic flow features around for instance the bow and in the cavities and their associated geometry based acoustics. This interaction (acoustic waves) is lost when using an incompressible solver (where only the hydrodynamics are captured). Since the domain in this thesis contains a wall, reflections of acoustics may not be negligible. This project deals with Mach numbers around 0.1, which seems low and under most compressible phenomena ($Ma > 0.3$), but one shall remember that acoustics is compressible. Further according to [2] there may be problems with sound radiation from incompressible approach such as:

- elliptic pressures, meaning that distortions will almost spread over the whole domain almost immediately.
- sharp edges can cause oscillations, since it can only be compensated with change in flow speed or change in pressure.
- Flows with few dominant structures may suffer from errors in the acoustical signals due to lack of compressibility.

4 Results

Contents

The idea with this results chapter is to confide the obtained results and observations. The layout will be to first present the different cases as they are, looking into fairly same things. Then do comparisons. This since plotting to much in a single plot would be just confusing and may drown the results. For sampling positions please see fig. 3.11.1 on page 29. The CFD results in this thesis were produced by the commercial software StarCCM+ version 6.6.11.

4.1 Mesh

The sizes of the different meshes used is presented in table 4.1.1. The largest one is the LES mesh for cab without bow. DES where slots are removed requires least amount of cells. Noticeable is that the difference in number of cells between LES and DES cases is around 8 million, which is then "saved". This "saving" constitute not less than around 60% of the number of cells in a LES mesh! The difference in mesh sizes between free stream and pressure outlet case for LES is a result of refinement in propagation region.

Table 4.1.1: Mesh sizes for different cases

Case	Number of cells	Number of faces
LES-bow - pressure	12 365 669	12 824 424
LES-bow - freeStream	12 574 104	37 568 977
LES-no bow - pressure	12 936 624	38 679 664
DES-bow - free stream	4 436 683	13 231 911
DES-no bow - pressure	4 688 316	13 972 994
DES-no bow - free stream	4 688 316	13 972 994
DES-no slots - free stream	3 288 482	9 831 657
URANS-bow	4 439 505	13 236 838

4.2 LES

LES was used for both with and without bow. Results for both of them are presented below.

4.2.1 Bow mounted

This is the "base configuration" case, which contains what is thought of as problem areas. Both free stream outlet as well as pressure outlet boundary conditions were tested, to see if there would be any significant difference in results and whether it works to map all boundaries or not.

Free stream outlet From fig. 4.2.1 one can see that the front probe shows highest SPL and that the lowest SPL is found rear of bow, which is somewhat expected (according to Curle, fig. 3.6.1). The difference is noticeable large around 200[Hz], where it is around 20dB. Above 1 000[Hz] the SPL monotonically decreases for all probes except for the one rear of bow, which have a broad band bump[1] in the frequency band ~2 000[Hz]-6 000[Hz]. The jump at high frequencies for the rear_of_bow-probe is believed to be numerical error.

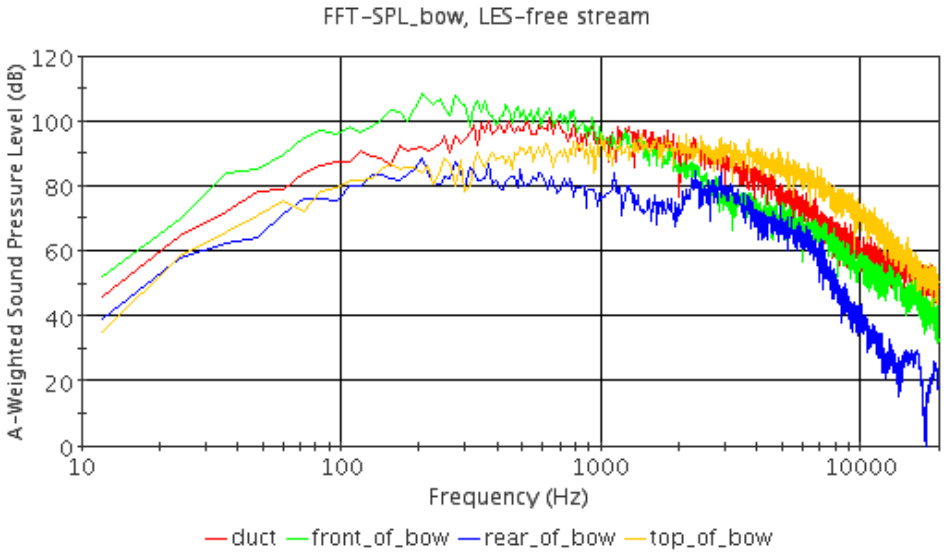

Figure 4.2.1: *SPL(A-weighted) around bow, LES-free stream outlet*

Three probes measured the pressures close to the surface on the hatch. Their recordings are visualized in fig. 4.2.2. From this figure it can be seen that their curves almost coincide at ~70[Hz]. Thereafter the front probe measures the highest SPL. The SPL decreases with distance from front probe location. The shape of their corresponding curves is though somewhat similar. For the slots (probes) it seems to be more activity in the front slot, red curve in fig. 4.2.3 on page 34, with a maximum SPL of ~100dB at 600[Hz]. In the rear slot something happens at ~1 100[Hz] and ~2 500[Hz]. These peaks are located in a band of higher levels which range from ~1 000[Hz]-7 000[Hz].
The force coefficients seems to fluctuate around ~0,36 for C_d and ~0,15 for C_l. The magniute of the fluctuations are larger in C_l than in C_d. Figure of this can be found in appendix B, fig. B.0.3.

[1] A bulge in the curve, meaning higher values in a certain range

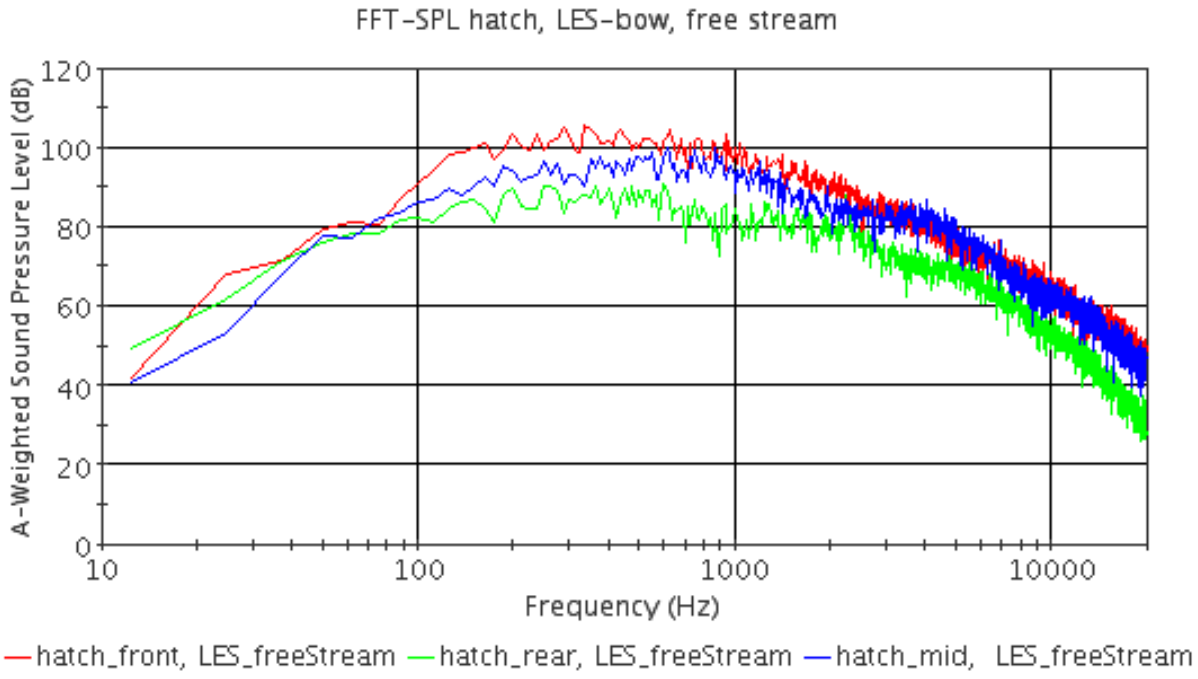

Figure 4.2.2: *SPL(A-weighted) for hatch probes , LES-free stream outlet*

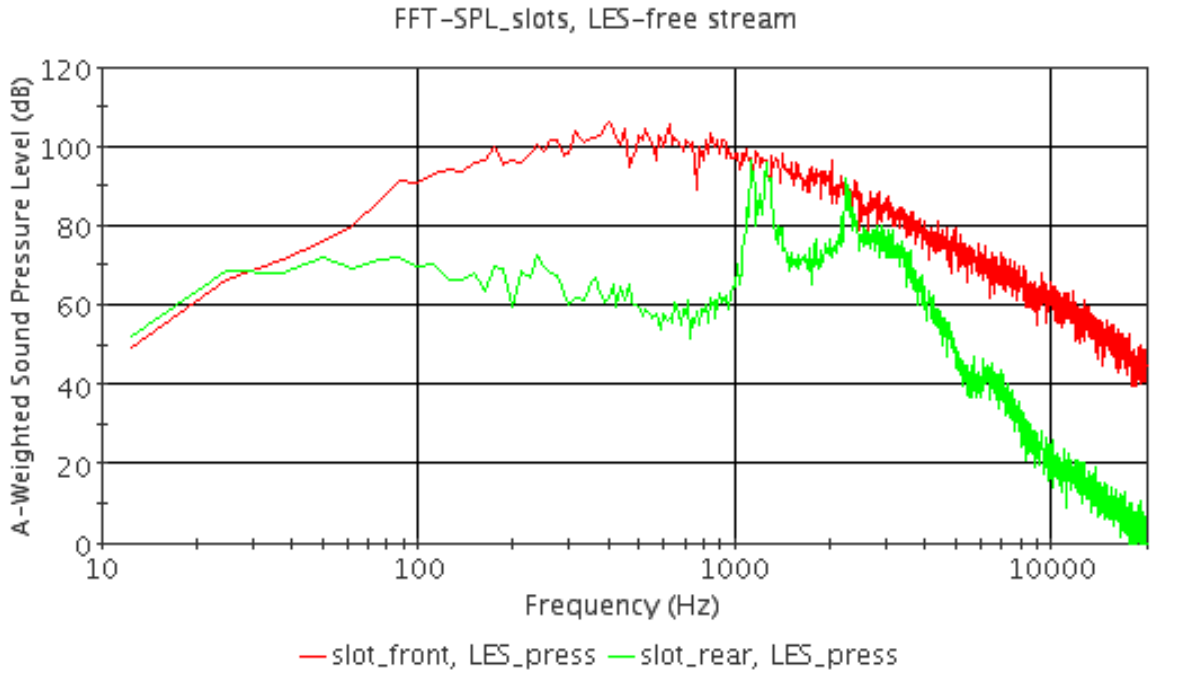

Figure 4.2.3: *SPL(A-weighted) in slots, bow, LES-free stream outlet*

Pressure outlet The SPL around the bow for the case with pressure outlet can be seen in fig. 4.2.4. The highest SPL levels are found above and below the bow, in the duct, which is the channel between the bow and the roof. Probes upstream and downstream the bow often shows lower SPL levels, the difference between these and the probes below and above is especially remarkable around ∼1 000[Hz], fig. 4.2.4. The front and rear probe has a more significant "bump" which makes them reach the levels of the duct at ∼4 000[Hz]. Only small peaks in the "top_of_bow" probe reaches above 100dB at around 500[Hz], which is maximum.

Moving to the hatch will also give levels that are around maximum 100dB above ∼200[Hz] for the front probe. The rear probe reaches its maximum of 95dB at 160[Hz] and therefore starts its decrease in SPL at lower frequencies, fig. 4.2.5. The two curves intersects at 110[Hz].

When going further down into the slots, fig. 4.2.6 on page 38 reveals that the front slot experiences higher levels than the rear slot, up to about 20dB at 1 000[Hz]. In the region 2 000[Hz]-10 000[Hz] the curve for the rear slot rises to higher levels in a "bump". For the front slot this "bump" is not as wide as for the rear and seems to be divided into two peaks; one peak at ∼3 000[Hz] and the other at ∼7 000[Hz]. So the difference between free stream and pressure outlet regarding SPL around the bow at first glance seems to be the differences at ∼1 000[Hz], where pressure outlet predicts lower values. This behavoiur is also found when comparing for the hatch.

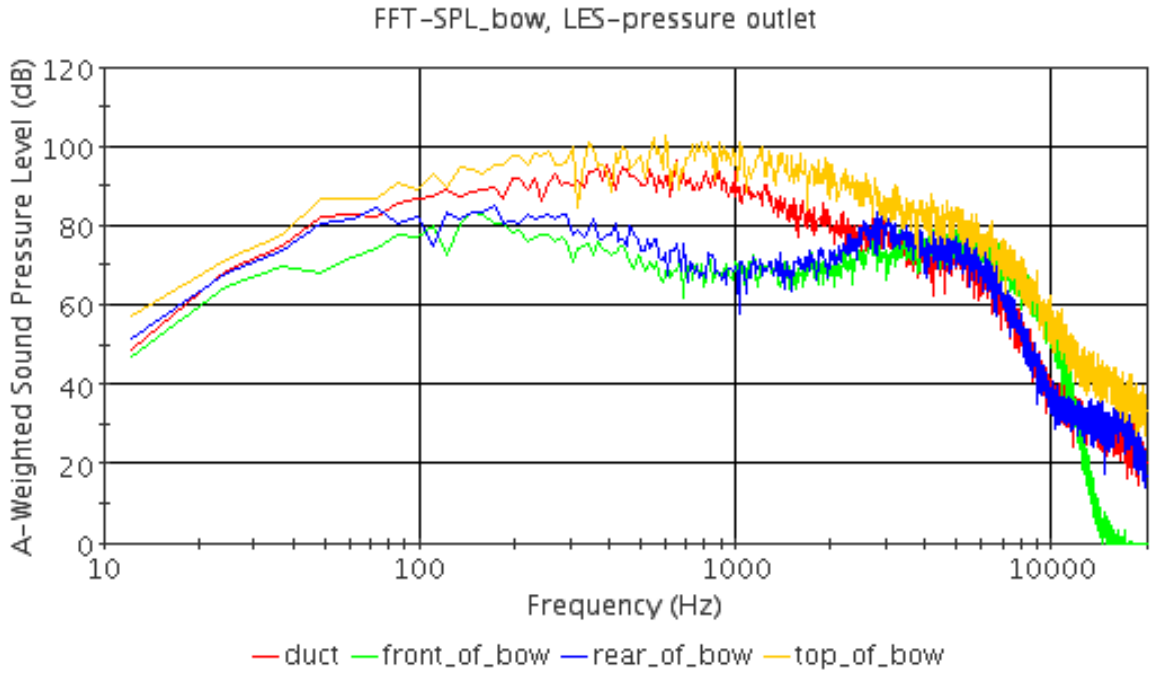

Figure 4.2.4: *SPL(A-weighted) around bow, LES-pressure outlet*

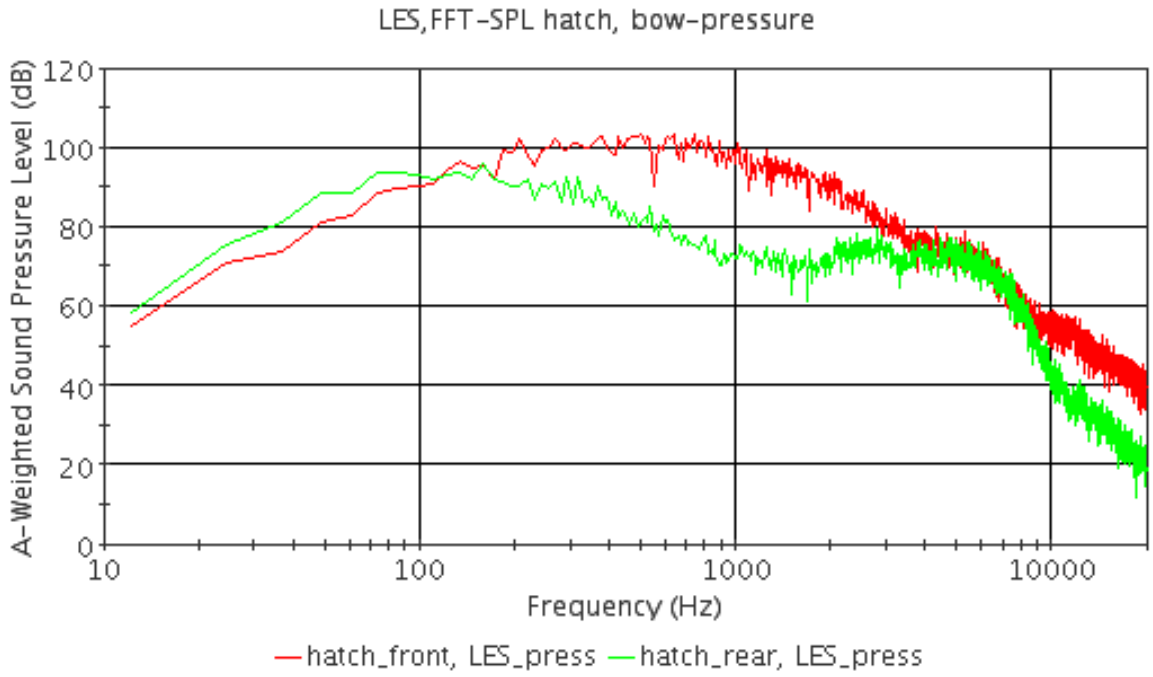

Figure 4.2.5: *SPL(A-weighted) on hatch, bow, LES-pressure outlet*

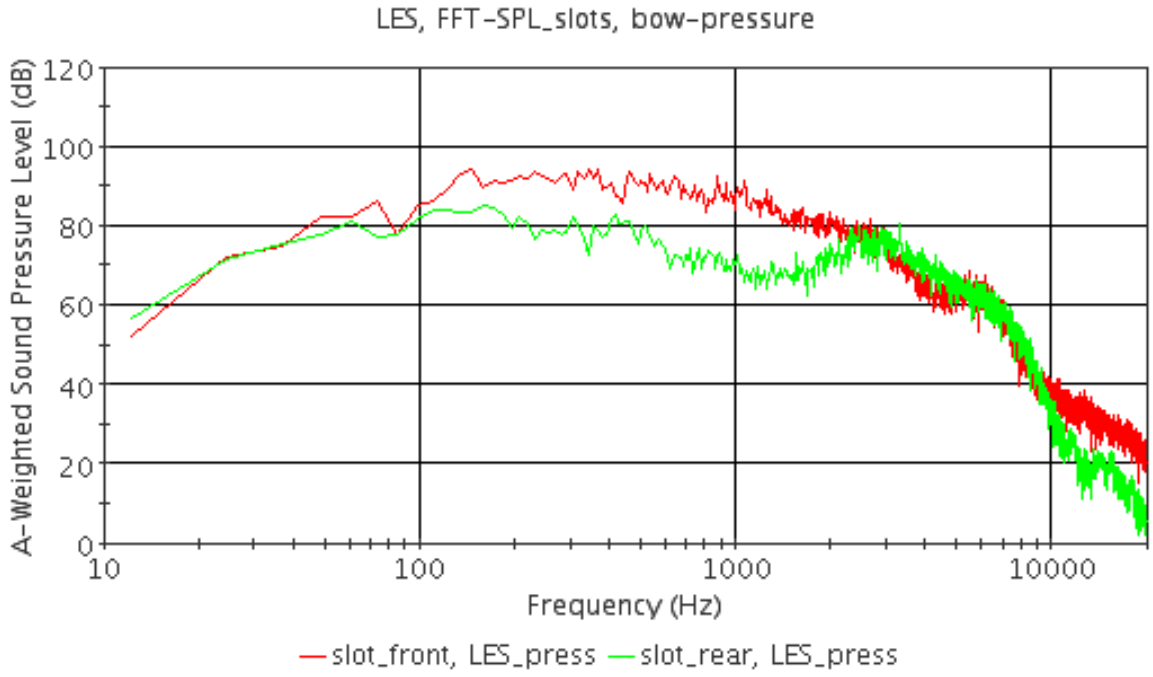

Figure 4.2.6: *SPL(A-weighted) in slots, bow, LES-pressure outlet*

4.2.2 Without bow

The simulation without the roof bow using LES, was due to high cost only performed with pressure outlet boundary condition.

Pressure outlet Maximum SPL on the hatch is achieved at around 100[Hz] where the front probe reaches ∼90dB, fig. 4.2.7. Also here a "bump" can be observed which starts at ∼1 000[Hz] for the front probe and at the doubled frequency (∼2 000[Hz]) for the rear probe. The frequency width of this "bump" is almost 8 000[Hz]. Up to ∼400[Hz] the curves for the hatch probes show quite the same behaviour. Then they start to deviate from each other to reach a difference of almost 20dB at ∼1 000[Hz].

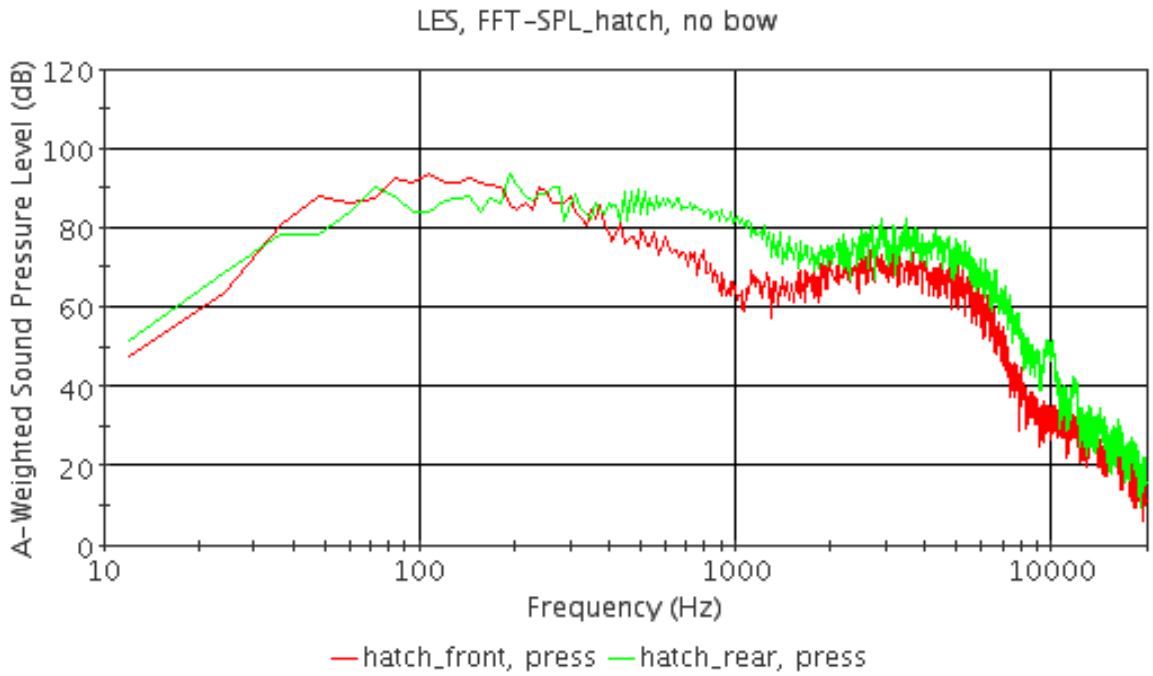

Figure 4.2.7: *SPL(A-weighted) on hatch, for case without bow using LES-pressure outlet*

When looking into the slots, the curves in fig. 4.2.8 seems to be different. The difference is large: up to about 20dB. There are some interesting peaks as well. The rear slot have one at 3 000[Hz], while the front one seems to have two. The first at the same frequency as the peak of the rear slot (3 000[Hz]) and the second one at 5 000[Hz]. The peaks do not indicate single tones though, since they are not that distinct.
Fig. 4.2.9 shows the SPL for the wake probes and tells that the level is higher and the spread is wider when approaching the front of the cab roof.

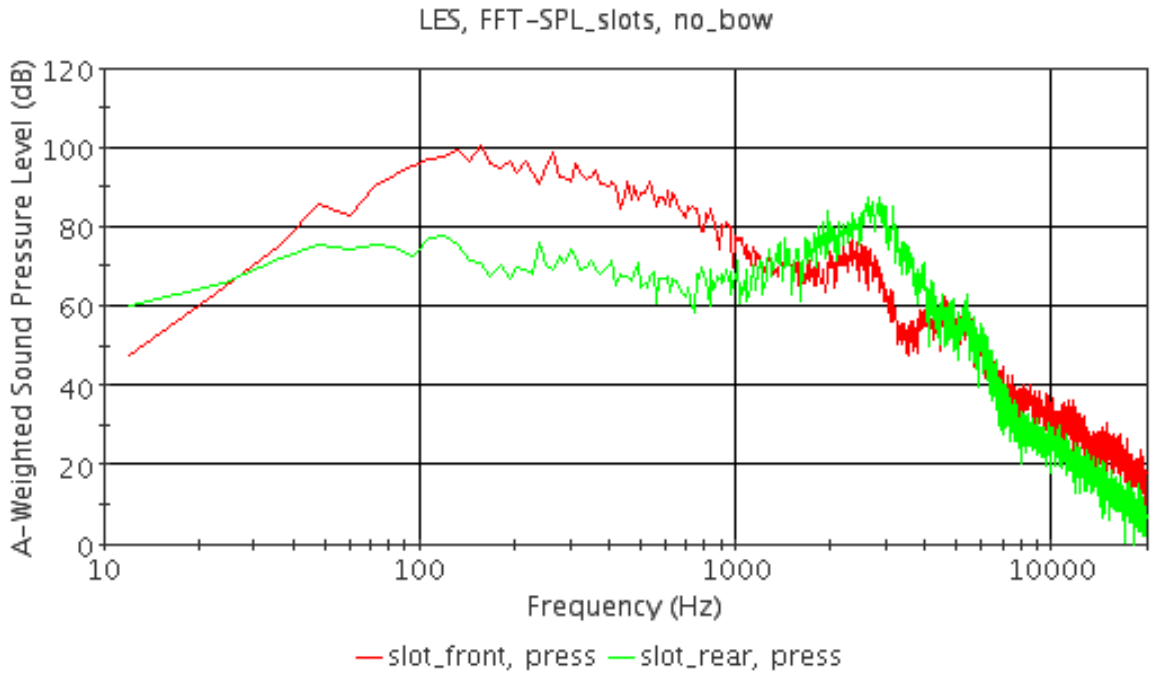

Figure 4.2.8: *SPL(A-weighted) in slots, without bow, using LES with pressure outlet*

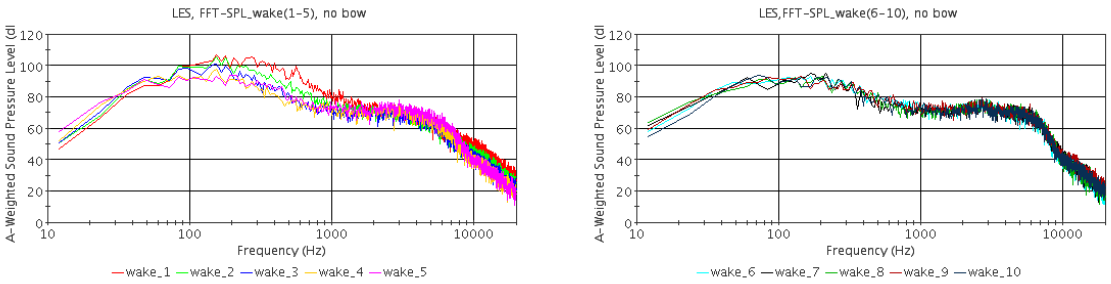

(a) wake 1-5

(b) wake 6-10

Figure 4.2.9: *SPL(A-weighted) for wake probes, no bow, LES*

4.3 DES

Presented here are the DES results, which serves as an alternative method to LES. As with LES it was tested both with and without roof bow.

4.3.1 Bow mounted

Only free stream outlet condition was tested for the case with bow, presented below.

Free stream outlet The pressures in the wake were monitored and the results for wakeprobe 1-5 can be seen in fig. 4.3.1. This picture shows an oscillating pattern for all probes, and within this "large" oscillation smaller inherent oscillations. Fig. 4.3.2 shows the frequency spectrum for the hatch. Highest amplitude is found at ∼150[Hz] for the front probe which then reaches ∼109dB. This is for the same frequency about 20dB higher than the rear probe, which also has its maximum there. From around 2 000[Hz] to ∼9 000[Hz] the SPL is almost the same for both probes. Both curves have a dip, for the rear probe at 1 000[Hz] and for front probe at ∼2 000[Hz].

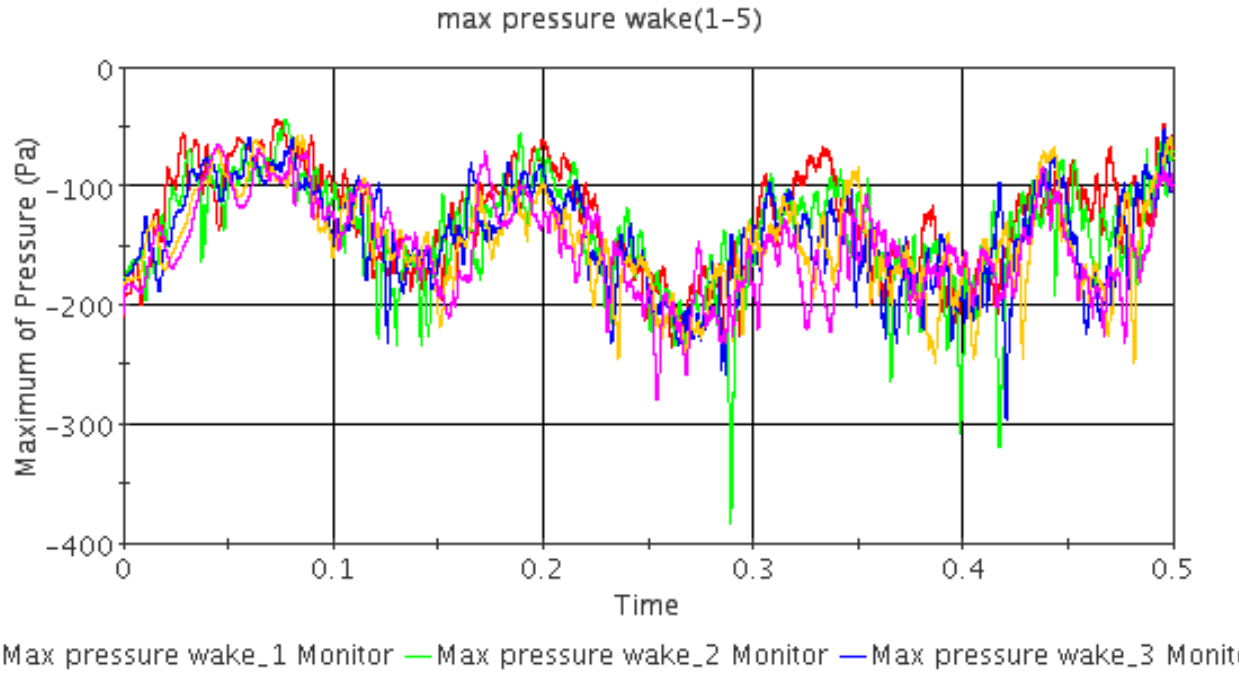

Figure 4.3.1: *Pressure in wake probes (1-5) for case with bow using DES and free stream outlet.*

Considering the slots seen in fig. 4.3.3 one can also here see that the rear slot generally has lower levels than the front probe. The peak in the rear probe curve is much more significant than the front one (if there even is a peak). A plateau, meaning almost constant SPL for a band of frequencies, is found for both front and rear probe in the interval ∼6 000[Hz]-7 000[Hz].

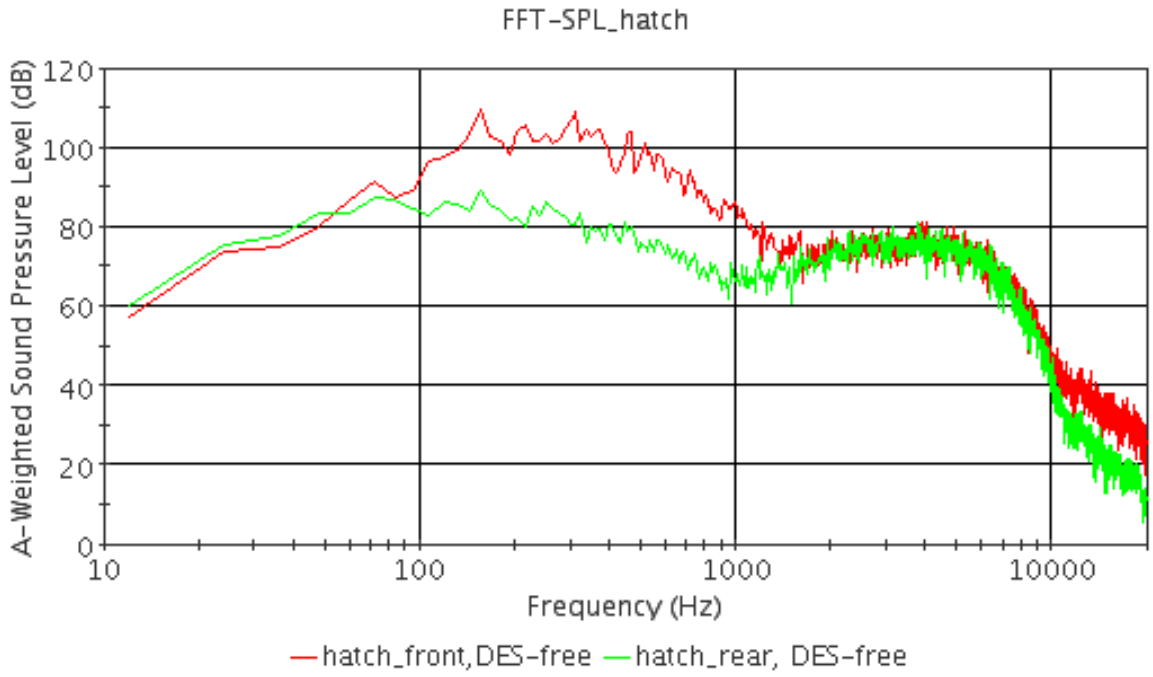

Figure 4.3.2: *SPL(A-weighted) on hatch for case with bow, using DES and free stream outlet.*

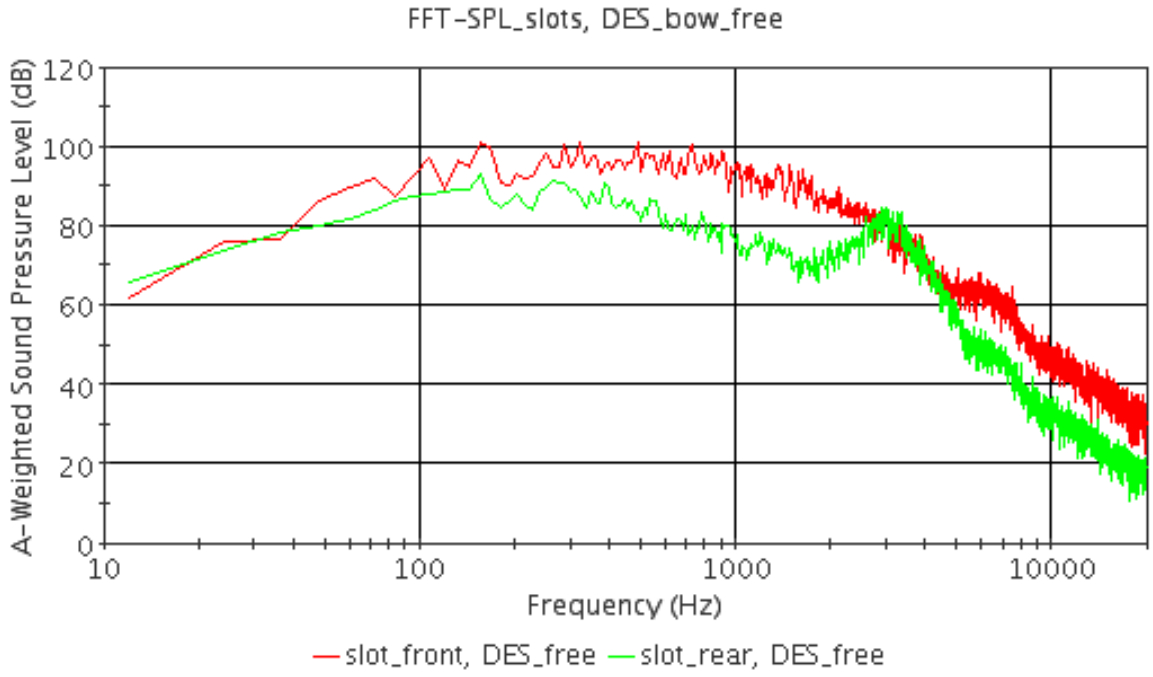

Figure 4.3.3: *SPL(A-weighted) in slots for case with bow, using DES and free stream outlet.*

4.3.2 Without bow

The case without the bow was tested with both pressure outlet and free stream outlet.

Free stream outlet When the bow is removed the sound pressure levels for the hatch probes are similar from ∼800[Hz] and up, fig. 4.3.4. The largest difference is obtained at around 70[Hz]. Similar behaviour can be seen when going down into the slots, fig. 4.3.5.

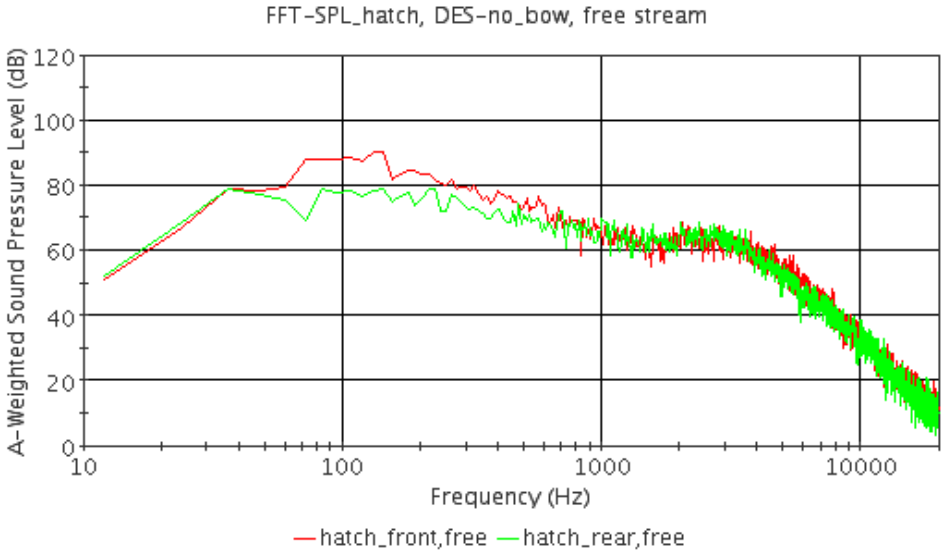

Figure 4.3.4: *SPL(A-weighted) on hatch for case without bow, using DES and free stream outlet.*

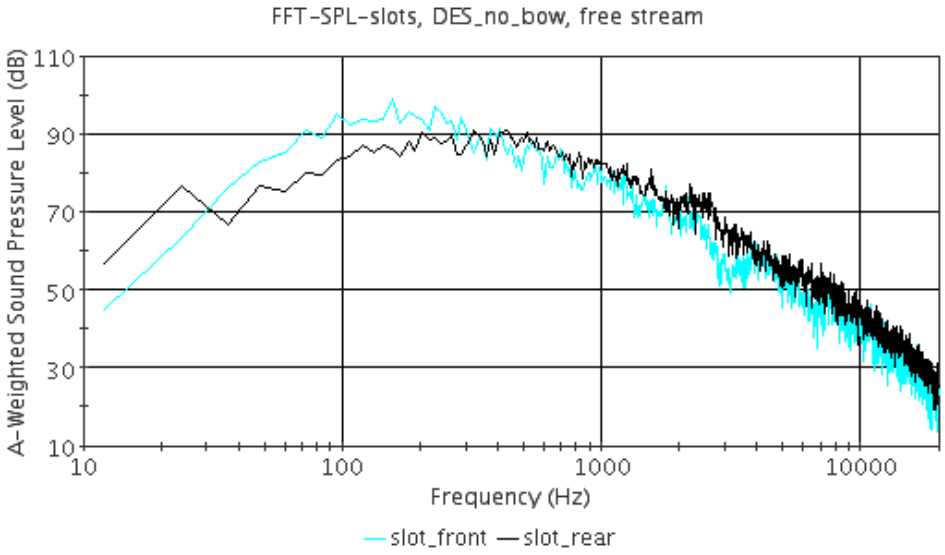

Figure 4.3.5: *SPL(A-weighted) in slots for case without bow, using DES and free stream outlet.*

Pressure outlet For the hatch the levels are similar for front and rear probe, except for in the frequency band ∼30[Hz]-200[Hz] where the front probe according to fig. 4.3.6 shows higher values. Maximum SPL is around 90dB for the front bow at ∼80[Hz]. The RMS variation for the rear hatch probe is just 2.8%.

The first slot experiences remarkably higher levels than the rear slot and the difference is ∼15dB at 100[Hz], fig. 4.3.7. Above 1 000[Hz] the curves for front and rear slot are almost parallel with an offset of ∼2-3dB.

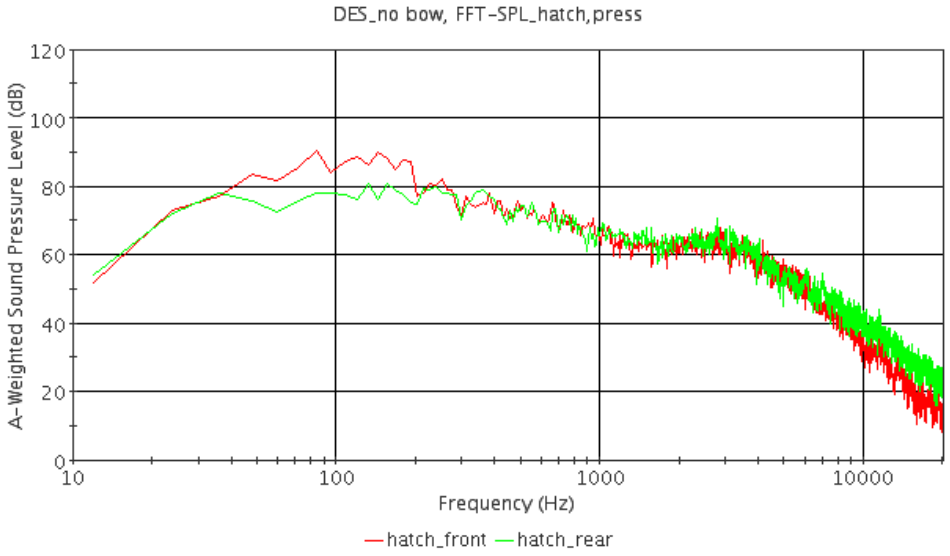

Figure 4.3.6: *SPL(A-weighted) on hatch for case without bow, using DES and pressure outlet*

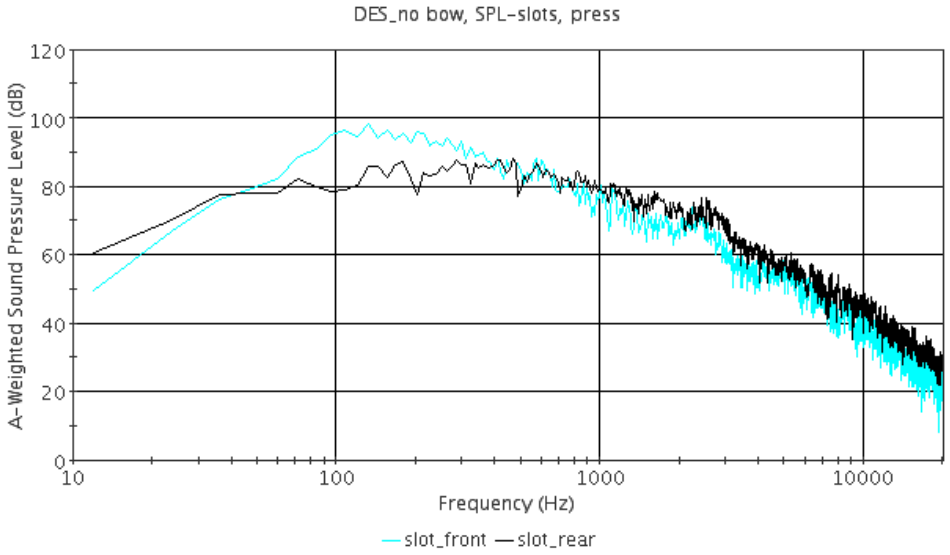

Figure 4.3.7: *SPL(A-weighted) in slots for case without bow, using DES and pressure outlet*

4.4 Comparison of bow versus no bow

This section combines plots from above LES simulations to make comparison easier. Removing the bow may not be a realistic option. But showing the difference may still be useful. The difference is large between the bow and no-bow case, which can be seen in fig. 4.4.1. For the front probe the variation is most substantial around 1 000[Hz], where the difference is as large as ∼30dB! For the rear probe the difference is not that extreme, it reaches a maximum of around 11dB at ∼90[Hz]. The "bump" for the front probe seems to reach a maximum level of ∼75dB, so it is not that prominent increase when the bow is added (but still ∼5dB).

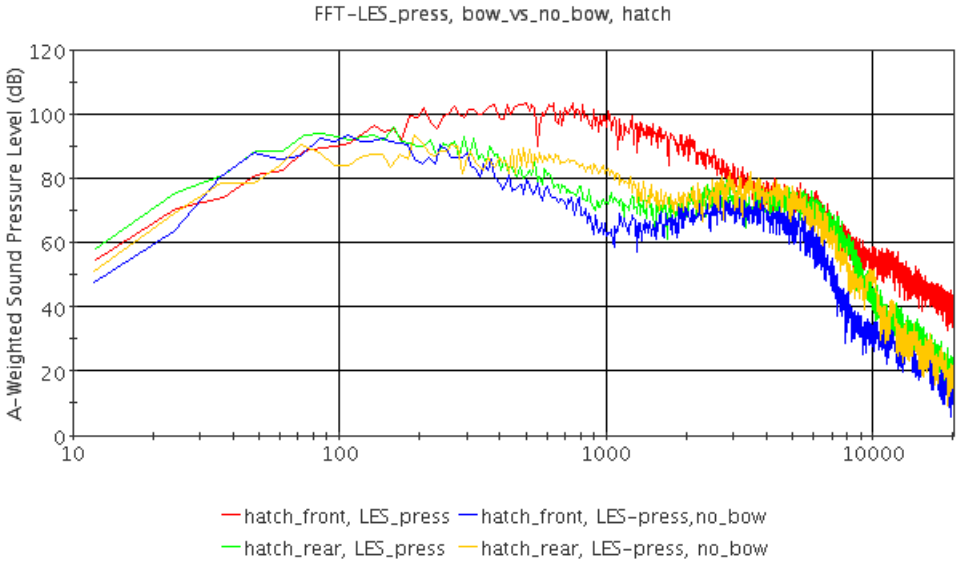

Figure 4.4.1: *Comparison between with- and without bow w.r.t SPL on hatch for LES using pressure outlet.*

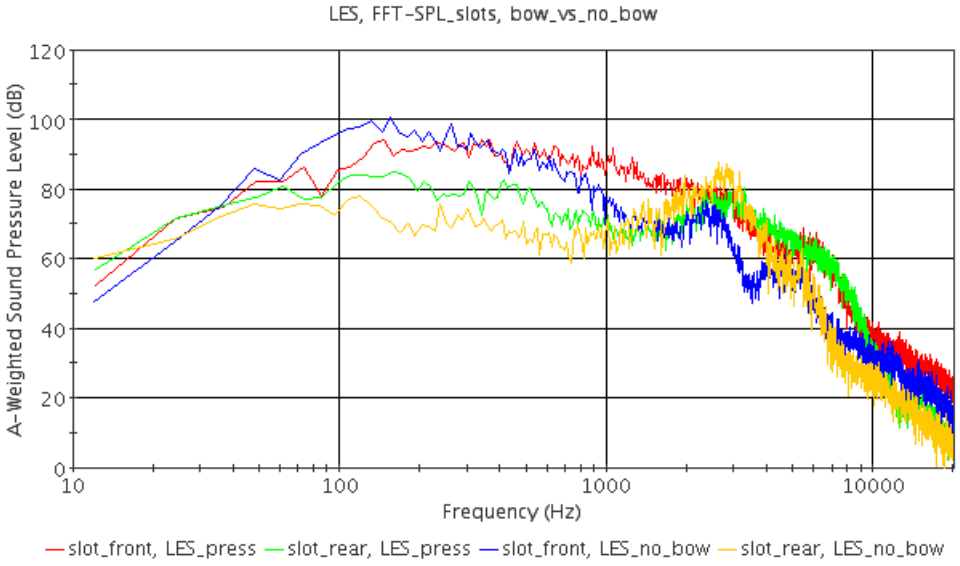

Figure 4.4.2: *Comparison between bow and now bow w.r.t SPL in slots for LES with pressure outlet*

4.5 Pressure- versus free stream outlet

It was tested to see how large the difference between pressure outlet (zero gauge) and mapped free stream is. The comparison was made using both LES and DES. When considering SPL on the hatch for the DES case without bow, one can in fig. 4.5.1 see that the difference is not prominent. Switching to LES with bow; the difference in SPL for various outlet settings seems to be more substantial when approaching the outlet, fig. 4.5.2. The free stream boundary should handle acoustics in a better way since it tries to be transparent to pressure waves and therefore not reflect them (under the right conditions).

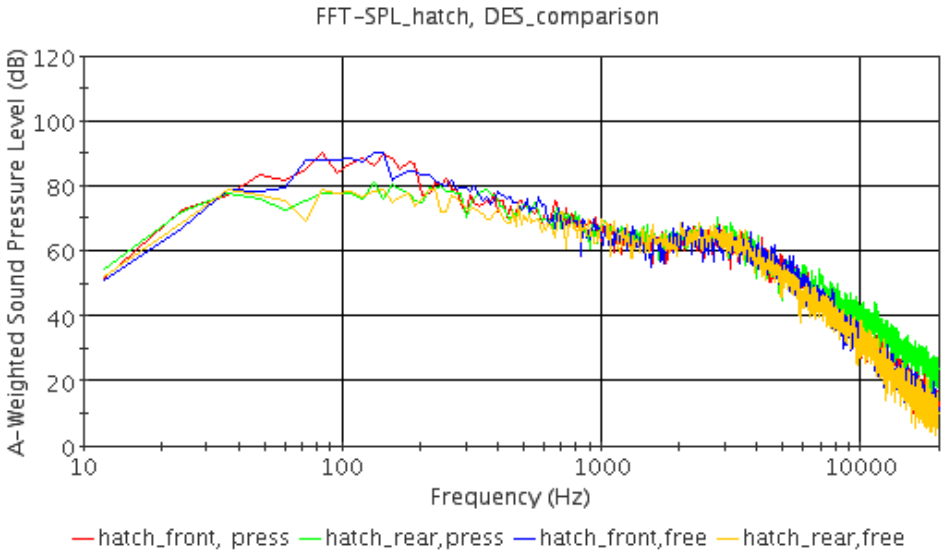

Figure 4.5.1: *Comparison between pressure- and free stream outlet w.r.t SPL on hatch for DES without bow*

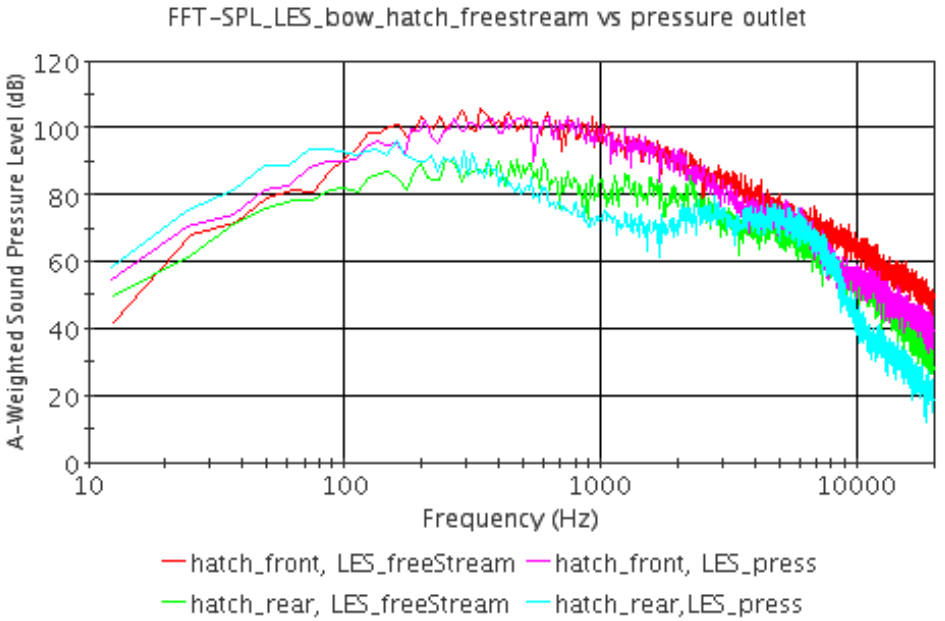

Figure 4.5.2: *Comparison between pressure- and free stream outlet w.r.t SPL on hatch for LES with bow*

4.6 LES versus DES

This section compares the LES and DES simulations in both with- and without bow case.

Bow From fig. 4.6.1 one can see that the prediction of both front and rear hatch probe is similar in the region ∼100[Hz]-300[Hz]. Up to 100[Hz] it is rather better match in calculation model (LES and DES) than probe position. The DES-solution seems to dip above 200[Hz] compared to corresponding LES solution, then it recovers up to LES levels again at ∼4500[Hz].

Considering the slots plot in fig. 4.6.2; the front slot shows higher levels than the rear slot, independent of calculation model. The LES solution predicts lower values for the rear slot than the DES and at the same time higher levels for the front slot. Both models seem to catch a peak at ∼3000[Hz]. Beyond this LES also captures another two peaks, the first at ∼1100[Hz] and the second one at ∼1300[Hz].

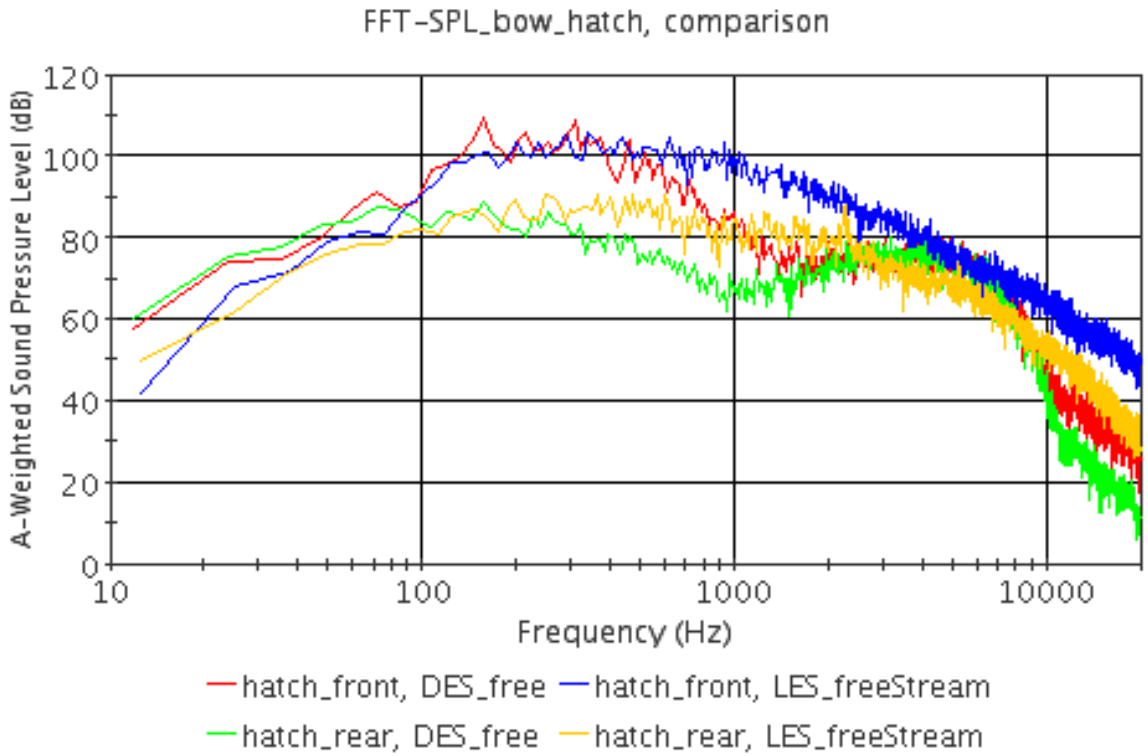

Figure 4.6.1: *Comparison between LES and DES w.r.t SPL on hatch for case with bow and free stream outlet*

No bow With the bow removed LES clearly predicts higher levels on the roof hatch compared to DES, fig. 4.6.3. LES also predicts larger differences between front and rear probe, which when using DES seems to be almost negligible above 1000[Hz]. This behaviour of larger variations in LES simulations can also be observed in the slots, fig. 4.6.4 on page 58.

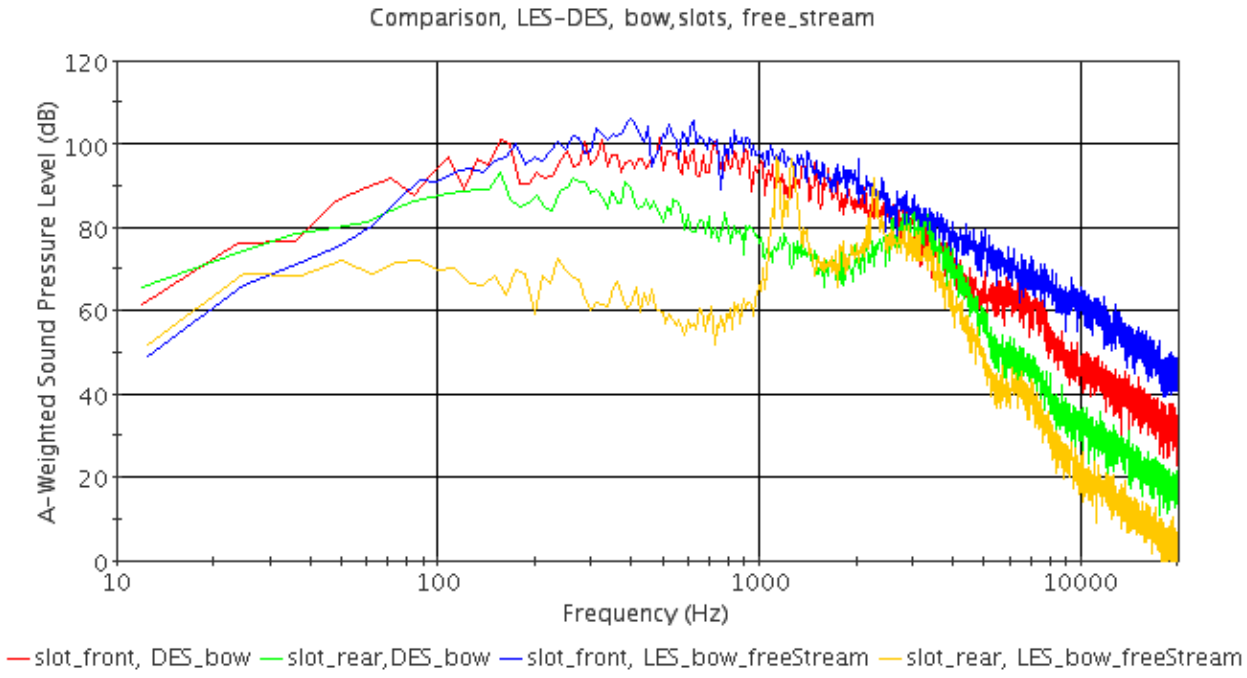

Figure 4.6.2: *Comparison between LES and DES w.r.t SPL in slots for case with bow and free stream outlet*

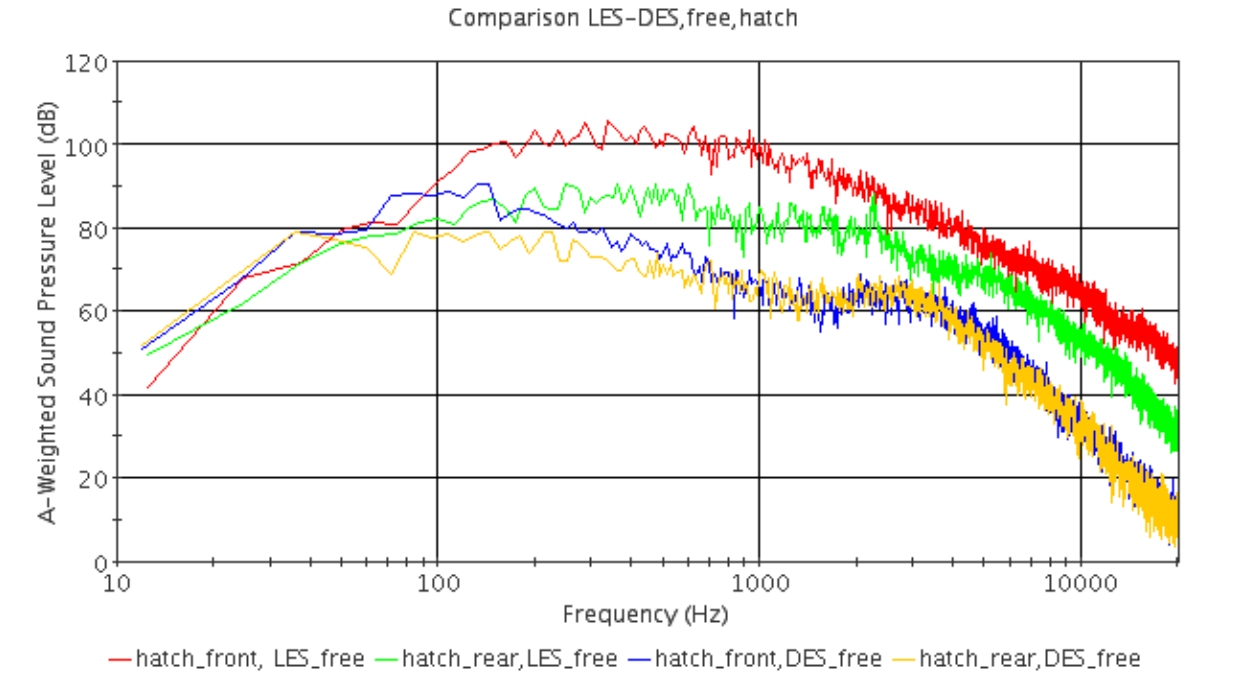

Figure 4.6.3: *Comparison between LES and DES w.r.t SPL on hatch for case without bow, using free stream outlet*

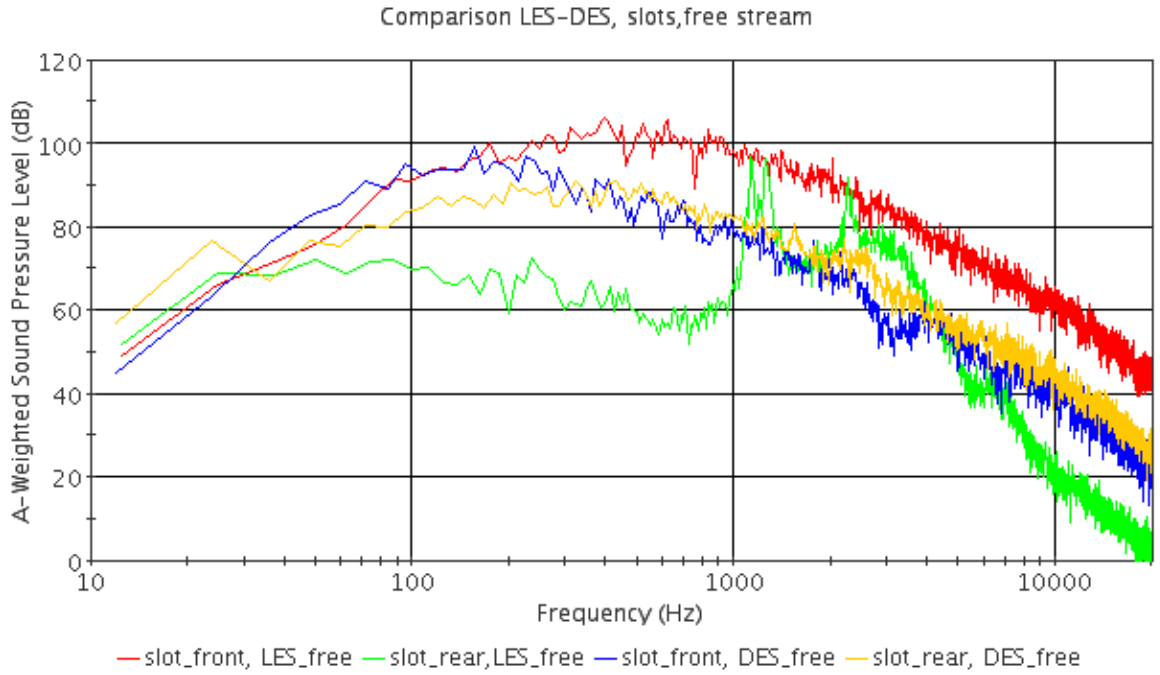

Figure 4.6.4: *Comparison between LES and DES in slots for case without bow, using free stream outlet*

4.7 Removed slots

Removing the slots means that the cavities were covered according to fig. 4.7.1 to form a flat plane as transition. When the slots are completely removed the response for the hatch probes can be seen in fig. 4.7.2. Both curves are then smooth and the front hatch probe indicates higher SPL than the rear probe for frequencies above ∼50[Hz]. Above ∼1000[Hz] something happens, the "bump" seen in fig. 4.7.2 is as much gone as the slots. Maybe due to the lack of cavity resonance. A plot with only the curves for case with removed slots can be found in fig. B.0.8 on page viii.

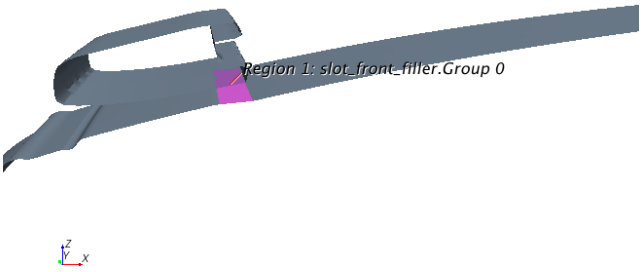

Figure 4.7.1: *Filler of front slot*

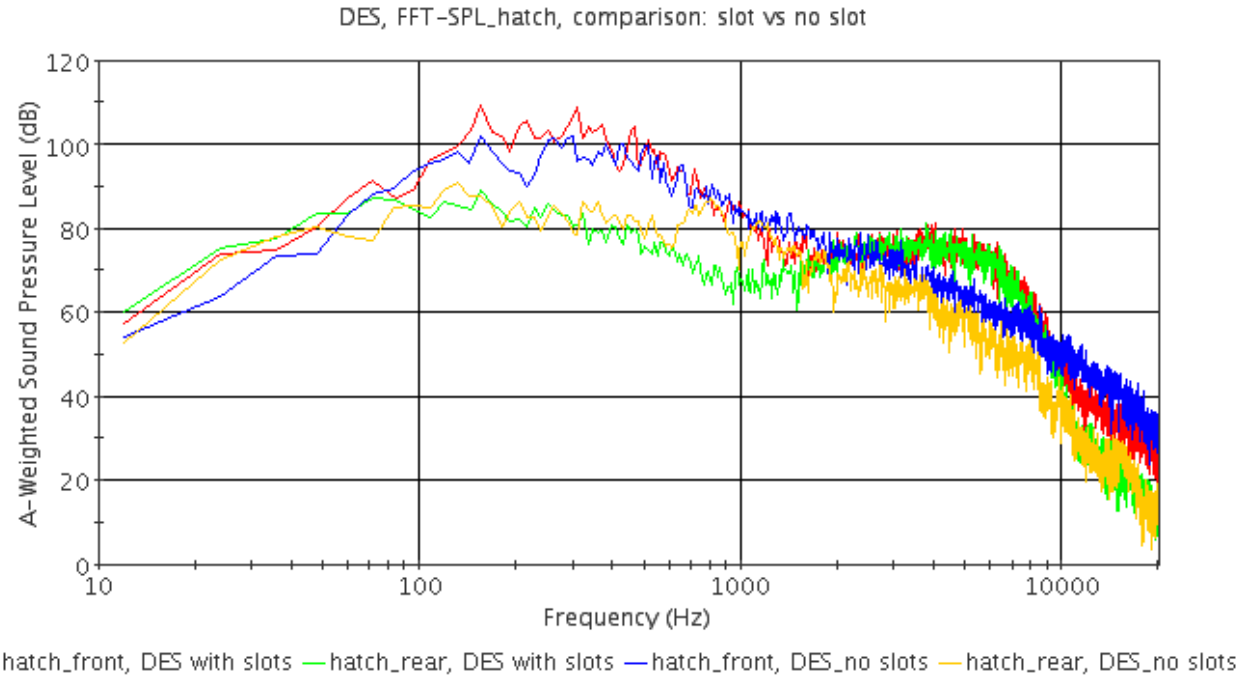

Figure 4.7.2: *Comparison between included and removed slots w.r.t SPL on hatch using DES and free stream outlet*

4.8 No bow versus no slots

When comparing what will reduce the SPL at the hatch the most, removing the bow **or** sealing the slots, fig. 4.8.1 reveals that removing the bow will have most impact on the whole spectrum above ∼50[Hz]. The case with the slots preserved still suffer from "the bump", but the levels of "the bump" is not as high as the ones for the case with only removed slots. Please be aware that both simulations uses DES and free stream outlet.

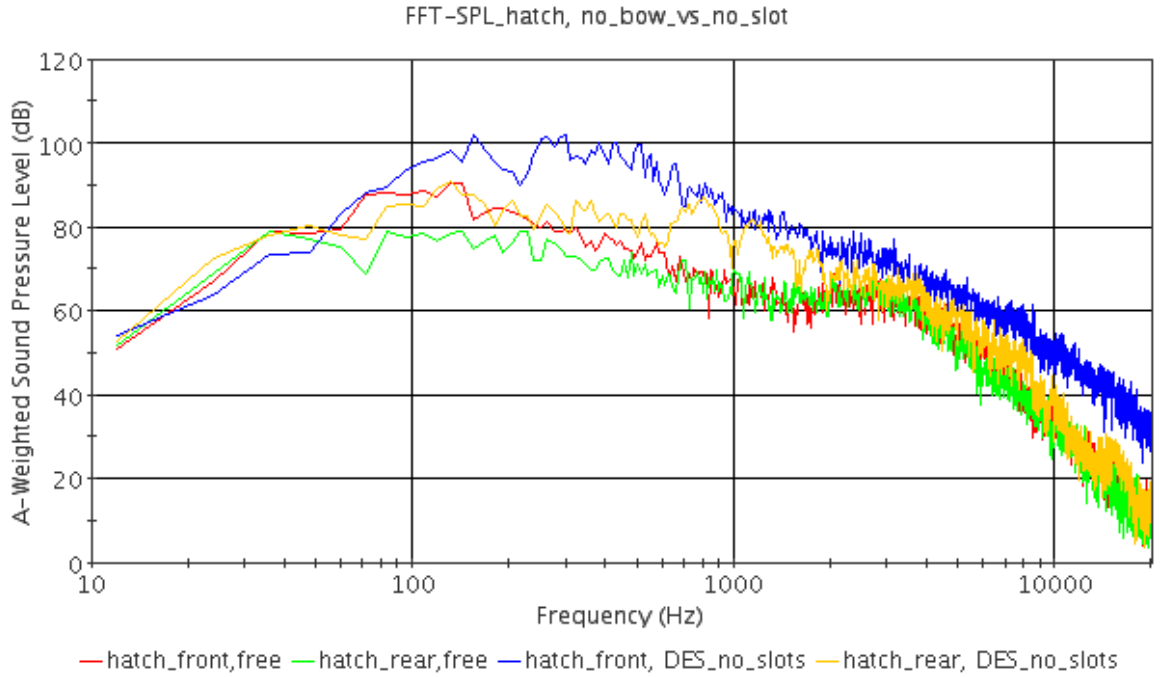

Figure 4.8.1: *Comparison of SPL on hatch for case with no bow and case with removed slots, free stream outlet*

4.9 URANS with bow

The bow was also run with URANS setting, to see if/where the prediction fails. From the yellow and blue curve in fig. 4.9.1 one can see that the prediction for the front and rear hatch probe is quite similar. The level of ∼80dB is held over a wide frequency band (80-2 000[Hz]). The decrease in SPL above 2 000[Hz] is then quite steep. For a plot of URANS solely, please see fig. B.0.16.

When comparing the results obtained with URANS to the ones obtained with DES, the first observation may be that URANS produces less difference between front and rear probe, fig. 4.9.1. The reason for comparing with DES and not LES, is that URANS was run on almost the same mesh as DES. Both curves of the URANS shows lower levels than DES up to 200[Hz]. The largest difference between URANS and DES at the front probe is not less than ∼20dB! The slope of the curves at the higher frequencies are similar. But they come with a frequency shift, meaning that they actually are far apart when looking at specific higher frequencies. The "bump" in URANS are much more narrow than its smeared out DES counterpart. When looking into the animations mentioned but unfortunately not shown in the report, the URANS simulation of the velocity field is looking almost stationary and just pulsate sometimes, compared to the DES animation which flares.

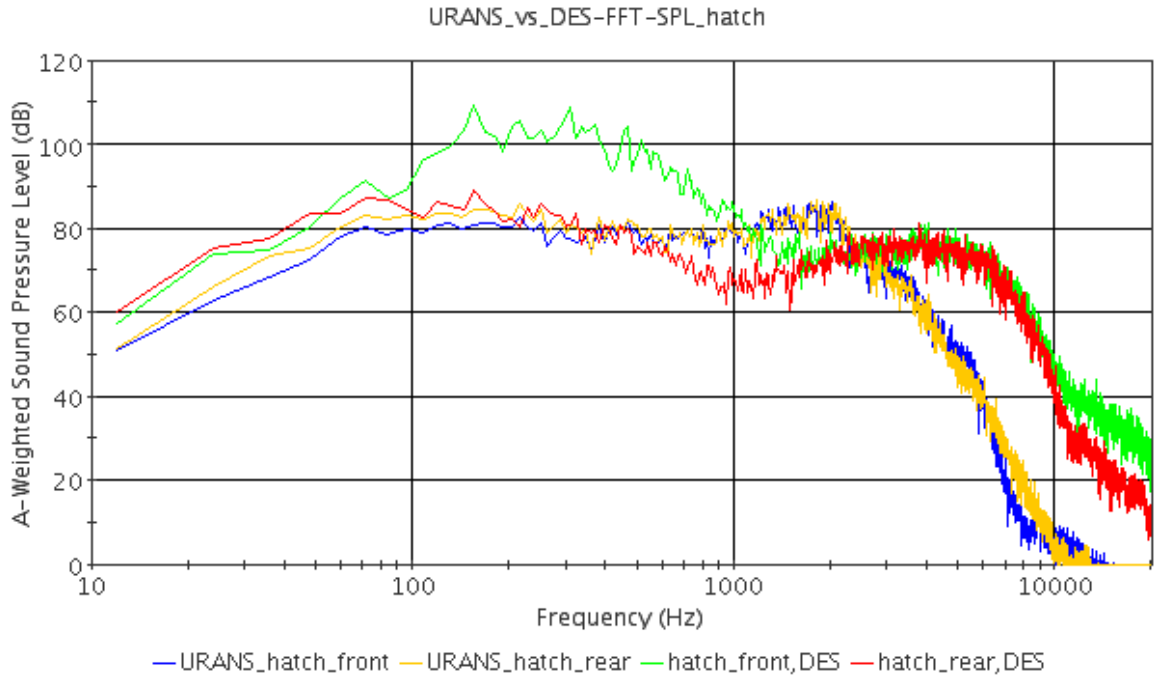

Figure 4.9.1: *Comparison of SPL on hatch for case with bow using URANS or DES, free stream outlet.*

4.10 DES, fast run

A couple of different solver settings were tested, to see how fast and aggressive the simulations can be run. The result is that longer time steps ($4{,}0 \cdot 10^{-5}$[s]) and fewer inner iterations (3) in combination with high under relaxation factors almost immidiately blows up[2] the calculation. The solver is segratated with temperature, which is what diverges (the temperature suddenly chase off in the bow region). Decreasing URFs and increasing the number of inner iterations will prolong the time before the calculation diverges. The idea of having a slightly longer time step ($2{,}5 \cdot 10^{-5}$[s]) and 4 inner iterations does not do the job either and the solution diverges after just a few iterations.

4.11 Time recordings

The simulation times varies a lot, which is an important factor for which model to use. Seen from the diagrams in fig. 4.11.1 the LES simulation for bow with pressure outlet is the most CPU-time consuming. This case was the first simulated, meaning that it was the only one that exported data (and mesh). Data was then exported every 11^{th} time step. The complete simulation was auto-saved every 1500^{th} time step. Even without exporting data, LES is the most time consuming, meaning that second most time consuming in this thesis is the LES for bow using free stream outlet. If instead considering the total solver time, the "leader" position i interchanged between these two. It may also be neccessary to mention that 2^{nd} simulation and onward was run with more pressure probes and with bounded central differencing scheme for advection instead of pure 2^{nd} order. The difference may also be derived from the time step length, seen in table 3.10.1. Worth mentioning is that capturing of pictures started already at around 0.13[s] for DES with bow and removed slots, which may have prolonged the total time. To set the total solver CPU-time into perspective: 50 000 000[s]∼13 889[h]∼578[days]. This is a long time! So the calculation was parallelized on a cluster to achieve the more manageable times seen in the diagram for total solver time, fig. 4.11.1. The scaling for this multicore usage is unfortunately not linear, so just having many cores wont help as good as first thought since the time for dividing, assemblying and communication between cores takes time from the actual calculation. The fastest simulation is however the one without roof bow, using DES and free stream outlet. One important result is also that the DES and URANS simulations will normally take less than half the time of an LES.

4.12 Miscellaneous

The first mode vortex shedding frequency calculation from the Strouhal number (2.9.2), using thickness of the bow and free stream velocity will approximetaly be:

$$f = \frac{St \cdot U}{L} = \frac{0.22 \cdot 25}{0.04} = 138[\text{Hz}] \tag{4.12.1}$$

which describes the oscillation frequency of the "tail" behind the bow. This seems to be close to the frequency belonging to maximum SPL-values in the frequency spectrum plot, for instance at the hatch, fig. 4.3.2 and the peak in the power spectral density plot at 156[Hz](multiple of 12[Hz]), fig. 4.12.1, which may indicate a fundamental frequency. Please note that this plot does not use a dB scale! Possible harmonics of this fundamental frequency, ∼300[Hz], 450[Hz] may be the peaks in the hatch front curve in fig. 4.9.1. There is no such distinct peak for the rear hatch probe. As a side track it could be calculated that the sampling time of 0.25[s] would capture 39 periods of this fundamental frequency of 156[Hz].

Regarding the cross-sectional area of the slot, it was estimated to 0,000 232[m^2] using simple summation of a quite ruff descretisation. The opening length is 0.015[m](same as l_0 in Rossiters model). The neck height is not precise, and therefore taken as the thickness of the hatch, 5[mm]. The Helmholtz resonance frequency (2.6.2) is with these data estimated to ∼2 600[Hz]. Which is within the "bump"-range, which can be seen in for example fig. 4.3.2 on page 44.

The vorticity transport velocity, u_{vc}, is approximetaly 15[m/s] over the cavity opening, estimated from velocity scenes. The gap length l_0 of 0,015[m] and modus 2 (estimated from velocity field scene, for example fig.

[2] make the solution diverge

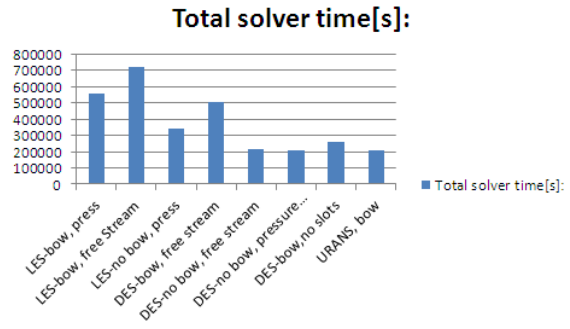

(a) Total solver time

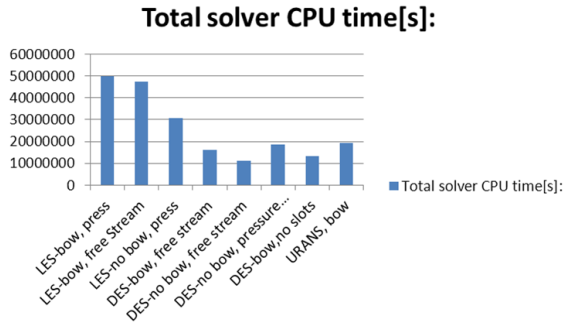

(b) Total solver CPU time

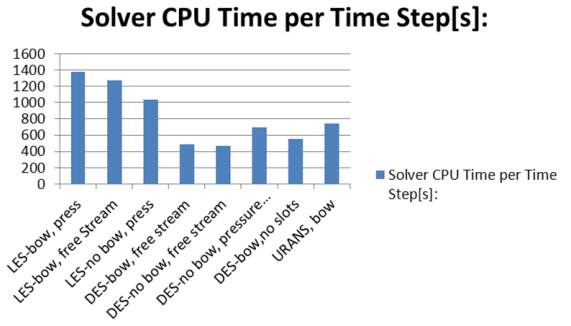

(c) Solver CPU time per timestep

Figure 4.11.1: *Time recordings for different setups*

B.0.18) will give a Rossiters frequency (2.6.3) of ∼2 000[Hz]. Sometimes it may also be of modus 3, which then corresponds to a Rossiters frequency of approximetaly 3 000[Hz]. These two frequencies are also within this "bump"-range.

Small displacements of the probes were noticed to have large impact on the SPL plots. Seen in fig. 4.12.2 the difference could be as much as ∼5dB for a probe dislocation of just 4[mm] along the hatch plane.

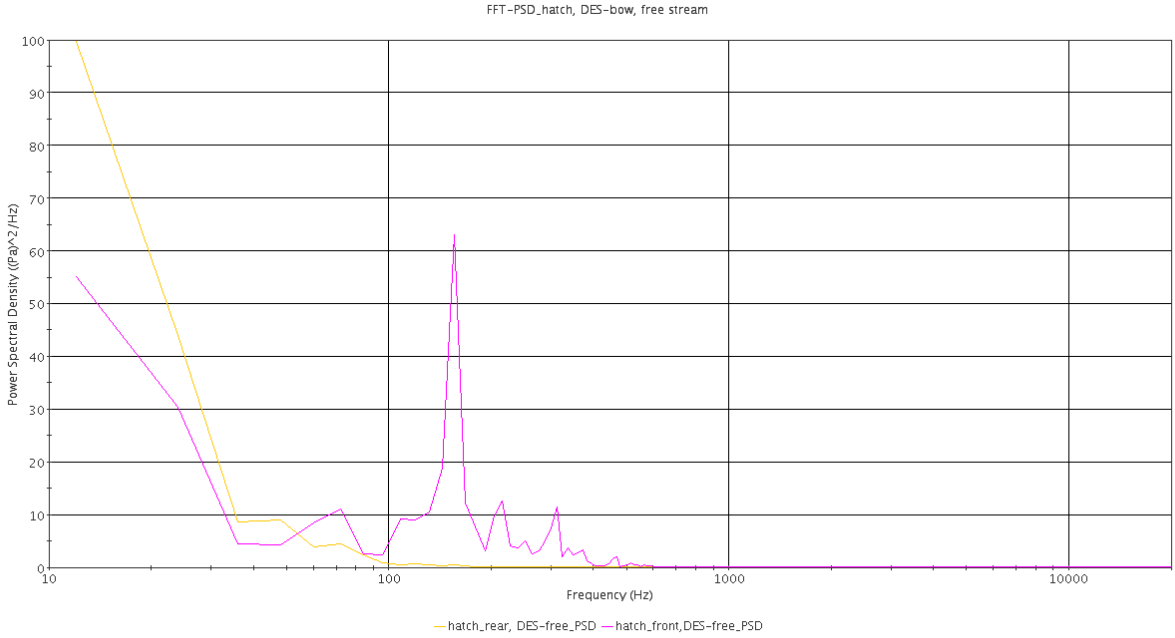

Figure 4.12.1: *PSD for hatch probes, with bow, using DES with free stream outlet*

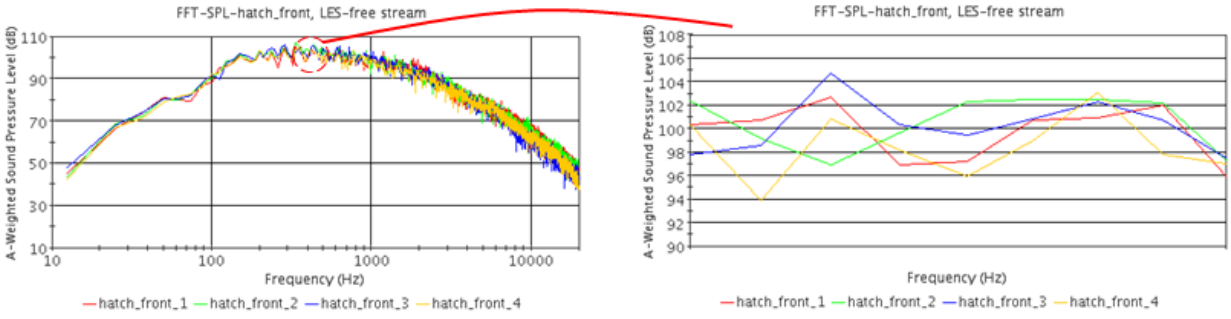

Figure 4.12.2: *Difference in SPL for closely located probes at the front of the hatch (left fig. is a zoom in).*

5 Discussion

There are some thoughts about both the methodology and the results, so for better readability this part is divided into subsections.

Methodology related

Trucks do not normally operate in speeds above 10 percent of speed of sound (∼34[m/s]), which would not introduce significant compressible effects. The volume sources (quadrupoles) are then likely to be subordinate to the dipoles on the surfaces when coming to sound emitted into the cabin. If further investigations after propagating the sound reveals/confirms this, a decision of accuracy versus cost can end up in large data storage savings. My recommendation if this is the case will then be to just export the data needed on the surfaces, for instance cab roof. This will as a bonus save a lot of time as well, both in exporting from CFD and mapping/reading into FEM (propagation)-part. If it turns out that the dipoles are dominant then maybe one also have to take another look on the near wall CFD-grid, especially where it has been coarsened. Classical rules of acoustics recommends 6 elements per wave length, in CFD this recommendation is around 20 and not to mention the boundary layer which requires a lot of cells. So there may also be data savings if mapping onto FEM-mesh and store it there instead of keeping it on the CFD-mesh. Maybe one can make use of the possibility of having this fine descretization for operations that may need fine spatial resolution, such as differences for derivatives and so forth before mapping. So if one can afford to test this it could be interesting to do a comparison (between FEM-based and CFD-based) of for instance the derivative of the Lighthill's stress tensor.

The field of aeroacoustics is now an interesting research topic, so a good idea would be to keep being up to date and constantly read recently published papers to avoid own pit falls and learn new things. This thesis uses up to date methods but dialogue with others about progress/processes might be good to capture new ideas.

I got the advise from an experienced CAE-engineer to export the data produced by special codes as soon as possible into Matlab and do your analysis there to keep track of what is happening, for instance the Fourier transform.

As ever a clear requirement specification would make result analysis easier. If one in advance knows the frequency range of interest and probably also the areas of interest, the complete work time may be reduced. The mesh may not be coarsened too much though, since it still has to capture the flow!

Fluid dynamics related

The initial boundary conditions used in this project are steady state ones. Getting somewhat right boundary conditions for transient solutions is crucial. One can now of course discuss the influence of mapping from steady state boundary conditions relative to a transient ones. Some information, such as sheddings might have been lost in action. I guess it will affect the flow both upstream and downstream, perhaps most downstream. The question here is then: how much? Can we reach even better convergence? Can one maybe make a cheat in the rest of the large domain and have a lower time-update frequency there? Take for instance every 5^{th} value and keep it constant for the remaining 4. This is in order to cut down computation cost for the rest of the domain if it's possible, and still provide transient boundary conditions.

The farther away from the truck one can afford to put the transient sub-domain the better I would say. The free stream boundaries used are intended to be transparent for pressure waves, but this is under the condition that it does not face any gradients. Which is not the case in this study. Since I do not know how an eventual pressure reflection would affect the result, I cannot at the moment tell how bad the reflections are, nor if they are present at all. These reflections are though believed to be at a minimum with available resources.

The fact that the gap between air directioner and cab roof was sealed may have raised the pressure in front of the air directioner, causing less mass to pass in the duct below the bow: this means less speed there!

DES sounds almost too good to be true, but some care has to be taken! It may give great results in some situations but not for sure in all. It requires a good grid, in that sence a grid which has it grid points at the right spots. This I will call "modern-time-handcraft" since it is almost a kind of an art producing these meshes.

I did program own field functions for mesh layout, it though required some pre-gridding and steady state results. It made its job generating grids, but later I realized that it made grids for steady simulations rather than transient ones. What I mean is that regions where small cells are needed in transients were not fixed in space. Since my mesh is time-independent its focus regions had to be larger than just steady state case. A time independent mesh still has the advantage of being just constant, which means it only need to be saved/ exported once for further post processing in other softwares.

The flow solver used in this thesis is based upon Navier-Stokes equations. There is another approach; using the Lattice Boltzmann method which solves the discrete Boltzmann equation using collision models for particles.

The Proudman formula is assuming isotropic turbulence without mean flow, so I wonder what the effect would be without this assumption. Further the structure in this thesis is rigid. I therefore wonder how much that influences the response if it was allowed to vibrate.

I have also read about limited numerical scales which also exhibits hybrid RANS-LES characteristics, but have a slightly different approach. It seems like this method is not as common as LES and DES, but still it can be interesting to have a closer look at. Another possible approach is to use the nonlinear disturbance equations (NLDE) which directly accounts for acoustic wave generation from subgrid scale structures.

It was quickly realized that StarCCM+ is a nice tool for fast generation of meshes. This is probably highly appreciated in most industrial situations.One has to be aware how the cutoff-length is calculated though. Sometime as $\Delta = max\left(\Delta x, \Delta y, \Delta z\right)$, it means that cubical cells would be optimal to keep Δ low.

Some may wonder why not simplifying this into a two-dimensional problem. The answer from me will then be that the flow is three-dimensional, and too much information might be lost when converting it. Further according to [30] LES requires three spatial dimensions and one time dimension, since it has its roots in DNS.

Small details may be negligible in the complete vehicle view, but of great importance when considering aeroacoustics. This means that when using a surface wrapper it is a good idea to tune it to capture for instance cavities even if they are not large contributors to a complete aerodynamic simulation. One big problem when performing computational aeroacoustics is the numerics. The large differences in energy content in aerodynamics compared to aeroacoustics may give numerical errors from aerodynamics which can be (mis)taken as loud sound. These diffusion and dispersion errors have to be as low as possible, since the amplitude of the aerodynamic field is several magnitudes larger than the acoustic amplitudes [58]. Further the acoustic wave lengths may be larger than the turbulence they arise from. They may also be broad banded with a large span in amplitude. Another difference between aerodynamics and acoustics is the propagation speed. Sound propagates in every spatial direction with its local speed of sound, whereas aerodynamics is more likely to spread with its mean flow. So a clear mismatch here!

One comment on the behaviour of the pressure samples: they are oscillating which is expected, though there is no obvious periodicity. When comparing this to articles published on less complex geometries such as cylinders, one may at first glance think there is something strange. But it is not, rather the opposite, one should actually start worrying if clear periodicity occurs.

The frequency cutoff function is based on RANS results, which may according to [58, chapter 6.8] miss some events such as sheddings. So it may be better for broadband excitations than narrow banded ones. But after all this is for helping the user and its a good tool. It also heavily relies on the kinetic energy. If not set properly it might give the frequency cutoff function some strange values.

Results related

Since the total physical time has not been verified to be enough, it might be wise to have that in mind when analysing and using the results.

In the FFT plots for example SPL around the bow using LES, one can see that three out of four curves above 10k[Hz] in fig. 4.2.4 on page 36 deflects to a lower gradient. This might be a result of numerical noise. The solutions are likely to be to well resolved in the FFT here.The remedy could therefore maybe be to lower the resolution in the higher frequency range of the FFTs. The probe located in front of the bow experiences highest Courant numbers and seen from same plot it does not deflect as steep as the others.

As [59] concludes "fluid dynamic feedback like the Rossiter-excitation can only be expected at surfaces with very small boundary thickness, or for cavities with very large volumes". This is not the case in this Master's thesis.

The difference in number of cells for case with bow and without bow is maybe not as big as first expected. This is believed to be a result of the fact that bow interior volume were not meshed (since no interior flow) and then replaced by mesh when the bow was removed.

Regarding the fundamental frequency and the absence of such distinct peaks in the PSD plot for the rear hatch probe as for the front hatch probe, it might be due to that the bow affects its surrounding the most.

From the results one can see that mounting a roof bow is not a good idea in an aeroacoustic point of view since it seems to raise the SPL on the hatch. So why not remove it? Why does it have to be located that high? Can it be enough to have just the slot on top of the bow for fastening, close attached to the roof without this duct in between? Would it not suffer less from drag? In corrosion sense, if one can manage the doors and the roof hatch, one would probably also manage this bow. One drawback would maybe be if some possible gaps act like flutes and produces annoying tones. It would be interesting to know if the duct itself could introduce vortex noise, such as whistling. One may also think of what happens if the angle of the roof is changed. Which may happen if the roof bow is designed to be universal and mounted onto other trucks. Would it be better or worse?

The frequency band for the slots in fig. 4.2.3 on page 34 is large, about 6 000[Hz] with two peaks in it. This seems to me to be a large span. Why does it happen? Why is there not such a behaviour in the front slot?

When changing (shortening) the time for doing the frequency transformation (original 0,25[s]) the curves changes somewhat. Maybe due to that large amount of data is lost when shortening it, or maybe due to that it actually misses some peaks. Maybe one can figure out a suitable time duration to capture complete cycles of significant structures.

FFT looks for periodicity, meaning then that some of the stochastic behaviour might be lost. But still this thesis may be able to draw some conclusions.

6 Conclusions

This Master's thesis has evaluated methods for aeroacoustics around a roof bow and concludes that:

Methodology related:

- Simulations show that there is a difference between LES and DES results. DES comes with a considerably cheaper price regarding time and data size. Which one of them that is most correct is though left un-validated.
- Large data storage capacity is needed if one decides to store data, even if this is done in a small scale.
- Domain size and correct boundary types can heavily affect the solution.
- Mapping also the outlet seems to have small affects, the difference is best seen near the outlet.
- The SPL is strongly dependent on measurement position. Just millimeters in offset will show large difference in levels. The SPL decreases with distance from "disturbed" regions.
- From the fast run it is seen that high Courant-numbers is devastating and that just lowering the URFs do not seem to be the remedy. So keep Δt low.
- LES seems to produce results with larger variation between probes than DES, fig. 4.6.3.
- URANS seems to produce results that deviates a lot from DES results at higher frequencies ($> 3\,000$[Hz]).
- Aeroacoustic simulations are time expensive.

Acoustics related:

- Removing the slots completely will flatten out the curve at higher frequencies, meaning the "bump" in SPL-plots disappears.
- There seems to be more activity in the front slot than in the rear slot, but the rear slot can still not be disregarded.
- Removing the bow reduces SPL more than just sealing the slot.
- No tones were found, the sound is considered to be broad banded noise. Though the calculated frequencies for resonance using both Helmholtz and Rossiter's models are within the range of the "bump".
- The frequency for maximum SPL on the hatch is found to be close to the vortex shedding frequency of the bow.
- From fig. 4.4.1 one can see that the bow has largest impact on the front hatch probe. So the swirl may die and just affect the closest surrounding to the bow the most, since the difference in the rear probe samples are much smaller.

There are of course more work to do here if one wants to. There are a lot more to write and read[1], but one must keep in mind that this is a Master's thesis and not a Ph.D report.

[1] and most likely some more conclusions to be drawn from persons with deeper knowledge.

7 Suggestions for further work

To verify that the total physical simulation time of 0.5[s] is enough, prolonged sampling durations can be tested. Try for instance a total physical time of 1[s] to see if any statistical steadiness is achieved. Different numbers of analysis blocks for windowing can also be tested, as well as different overlap and window functions for FFTs. The mesh is of great importance for the outcome of the simulations, both for elapsed time and accuracy, so investigate mesh dependency. The meshes are tailored for respective solver, but one can experiment with the coarseness and see how much it influences. Is it good/ worth it to have a very fine mesh? How coarse mesh can be accepted?

Naturally physical tests would be great to validate the numerics. These measurements then have to be carried out with great care. In order to try keep the error sources as low as possible only microphones that do not disturb the flow themselves are recommended. Flush mounted microphones with cavities will induce noise! Of course if one wants to compare with measurements inside the cab, the 2^{nd} half of the hybrid approach has to be done.

The solutions can most likely be better tuned using different settings for the sub grid scales models. To see the dependency of number of inner iterations, a run with a lot of iterations can be executed. It will probably take a lot of calculation time, so an investigation of what was gained from it is also recommended to make a decision if it is worth doing it in the nearest future. More inner iterations may lead to the possibility of taking longer time steps.

An investigation of how well steady state aeroacoustics performs and correlates to transient solutions would be an interesting thing to do. Steady state solutions for these cases are significantly faster to obtain than transient ones. You will of course not get time dependency and maybe not enough accuracy for input for further analysis. But at least be able to compare design solutions against each other in an aeroacoustical sense, which is believed to be a nice tool in iterative product development processes. Be aware that acoustical power and sound pressure level are not the same thing.

Since the inner part of the slots were removed, it would be interesting to investigate how that extra volume influences the sound field, and thereby if it was correct to remove it. Same thing for the sealing of the gap beneath the air directioner.

Another thing is to change the geometry, one can try other radii at the edges around the slot, have difference in height of trailing and leading edge of the cavity, putting trailing edge lower.

The boundary layers upstream as well as speed will likely change the acoustic behaviour. So if possible a larger spaced duct would be interesting to simulate. Or maybe no duct at all, see discussion. This thesis treated a duct that may be compared to a converging nozzle, so a diverging model would be interesting to see as well.
Since both aspiration noise and shape noise are important for the sound pressure level inside the cabin, it might be a good idea to investigate them simultaneously in order to see if/how they cooperate. If the shape noise is near the aspiration noise source, i. e. if close to a leakage channel to interior it might be easier for it to transmit. So maybe play around with the distances between the sources and cavities where possible leakages can be present. In other words, try to get the highest surface pressure fluctuations away from seals.

The DES grid can be checked in the transition region between the RANS region and the focus region. The risk is that the RANS region goes to far out with too fine grid and LES goes to close to wall. Expected is to go from modelled turbulence to resolved abruptly. Change this transition and see whether/how it affects the results. Check the turbulent viscosity ratio to try find grid induced separation.

To better understand the distribution of noise sources when interacting with structures (Aero-Vibro Acoustics) a wave-number analysis can be performed, which tries to separate the flow and acoustics embedded in CFD.

Two-point correlation is recommended to try to judge if the turbulence is somewhat correctly predicted, i. e. if the domain width is enough. Similar can be done with the autocorrelation function in time. Since LES and DES gives somewhat different results, discussions leading to guidelines of in which situations each model will be applied might be great help for the engineer.

Further a figure of merit may be great to judge different solutions. For example summing the acoustical energy in a certain frequency range (or several). It is also recommended to take a mean of several probes, or maybe a mean from a part surface. If plotting the SPL on surfaces, for instance the hatch, presumed interesting spots for measurements during test may be found. One could also investigate the SPL as function of distance from the bow and try to find a correlation. It would also be interesting to look into these aeroacoustical phenomena and methodology applies to other cabin details such as for instance rear-view mirrors and windscreen wipers as well.

From Rossiter's paper [46] it was concluded that a small spoiler ahead of the cavity could suppress the periodic pressure fluctuations. So one could do such a physical test or simulation to try find the impact on a truck like geometry as the one in this thesis. Also edge tones from the air jet hitting the front of the hatch could be interesting to look into. It is investigated/described by for instance [42, 21, 6]

8 Division of work

This project was carried out as a one-man project. Though an essential part has been provided by Volvo GTT. This part provided is the full truck model which generated the mapped boundary conditions.

List of Figures

List of Tables

References

[1] R. Allen, F. Mendonça, and D. Kirkham. "RANS and DES turbulence model predictions of noise on the M219 cavity at M=0.85". In: *International Journal of Aeroacoustics* (2005).

[2] J. Ask. "Predictions of Aerodynamically Induced Wind Noise Around Ground Vehicles". PhD thesis. Chalmers University of Technology, 2008.

[3] A.Travin et al. "Physical and numerical upgrades in the detached-eddy simulation of complex turbulent flows". In: *Fluid mechanics and its applications*. Ed. by R.Friedrich and W.Rodi. Vol. 65. Proceedings of te Euromech Colloquium 5. Munich, Germany: Kluwer Academic publishers, Oct. 2002, pp. 239–254.

[4] L. L. Beranek and T. Mellow. *Acoustics: Sound Fields and Transducers*. first. Elseiver Inc, 2012.

[5] G. Beta CAE Systems SA Thessaloniki. *ANSA*. version 13.2.1. Jan. 2012.

[6] J. Brackenridge and W. L.Nyborg. "Acoustical Characteristics of Oscillating Jet-Edge Systems in Water". In: *The Journal of the acoustical society of america* 29.4 (Apr. 1957), pp. 459–463.

[7] M. Brennberger. "Experimentelle und numerische Grundsatszuntersuchung zum Scheibedachwummern". In: *Haus der Technik, Aerodynamik*. Essen, Oct. 2004.

[8] F. M. ca et al. "CFD Predictions of narrowband and broadband cavity acoustics at M=0.85". In: *9th AIAA/CEAS Aeroacoustics Conference and Exhibit* (2003).

[9] M. Cabrol et al. "STAR-CCM+/ACTRAN for computational Aero-Acoustics". In: *Star American conference 2011*. CD-Adapco, Free Field Technologies. June 2011.

[10] D. Caridi. "Industrial CFD simulation of aerodynamic noise". PhD thesis. UNIVERSITA DEGLI STUDI DI NAPOLI FEDERICO II, DIPARTIMENTO DI INGEGNERIA AEROSPAZIALE, 2008. URL: http://www.fedoa.unina.it/3249/2/Tesi_Dottorato_Caridi-2008.pdf.

[11] S. Caro, P. Ploumhans, and X. Gallez. "Implementation of Lighthill's Acoustic Analogy in a Finite/infinite Elements Framework". In: *AIAA/CEAS Aeroacoustics Conference*. 10th. Conference were held in Manchester UK. AIAA/CEAS Aeroacoustics Conference. Manchester: Free Field Technologies SA, May 2004.

[12] S. Caro et al. "TBL Noise generated by a simplified side mirror configuration and acoustic transfer through the window: medelling using Actran and Fluent". In: *AIAA/CEAS Aeroacoustic Conference*. Ed. by 12th. 2006-2490. Cambride MA, USA: American Institute of Aeronautics, May 2006.

[13] S. Caro et al. "Validation of a New Hybrid CAA strategy and Application to the Noise Generated by a flap in a Simplified HVAC Duct". In: *skipbib=true*. Vol. 15th. 09-3352. Miami: AIAA/CEAS Aeroacoustics Conference, May 2009.

[14] U. CD-adapco Melville NY. *Star CCM+*. version 6.6.11.

[15] N. Curle. "The Influence of Solid Boundaries upon Aerodynamic Sound". English. In: *Proceedings of the Royal Society of London. Series A, Mathematical and Physical Sciences* 231.1187 (1955), pp. 505–514. ISSN: 00804630. URL: http://www.jstor.org/stable/99804.

[16] N Curle. "The influence of Solid Boundaries upon Aerodynamic Sound". In: *Proceedings of the Royal Society of London*. Vol. A231. 1187. The Royal Society, Sept. 1955, pp. 505–514.

[17] L. Davidson. e-mail. total physical time. Mar. 2012.

[18] L. Davidson. *Fluid mechanics, turbulent flow and turbulence modeling*. division of fluid mechanics, department of applied mechanics. Chalmers University of Technology, 2012.

[19] L. Davidson. "large Eddy Simulations: How to evaluate resolution". In: *International Journal of Heat and Fluid Flow* 30 (Oct. 2009). The 3rd International Conference on Heat Transfer and Fluid Flow in Microscale, pp. 1016–1025.

[20] V. D.Narasimhamurthy. "Unsteady-RANS Simulation of Turbulent Trailing-Edge Flow". MA thesis. Chalmers University of Technology, Department of Thermo and Fluid Dynamics, 2004.

[21] S. Elder. "Edgetones versus pipetones". In: *The journal of Acoustical Society of America* 64.6 (Dec. 1978), pp. 1721–1723.

[22] F.Mendonça et al. "Aeroacoustic Simulation of Double Diaphragm Orifices in an Aircraft Climate Cooling System". In: *AIAA-2005*. AIAA-2005 2976. 2005.

[23] W. P. Graebel. *Advanced fluid mechanics*. Elsevier, 2007. ISBN: 978-0-12-370885-4.

[24] K. M. GÜLEREN. "Large-eddy simulation of wall-bounded flows subjected to curvature and rotation". PhD thesis. School of Mechanical, Aerospace and Civil engineering, The University of Manchester, May 2007.

[25] J. Guyer. "Fundamentals of Acoustics". Course no:M02-022. 2009.

[26] A. Hirschberg and S. Rienstra. "Theoretical background: Aeroacoustics". In: ed. by C. Wagner, T. H. ttl, and P. Sagaut. Cambridge Univeristy Press, 2007. Chap. 2, pp. 24–89.

[27] M. J. Lighthill. "On Sound Generated Aerodynamically. I. General Theory". English. In: *Proceedings of the Royal Society of London. Series A, Mathematical and Physical Sciences* 211.1107 (1952), pp. 564–587. ISSN: 00804630. URL: http://www.jstor.org/stable/98943.

[28] F. Mendonça et al. "Efficient CFD Simulation Process for Aeroacoustic Driven Design". In: *SAE Technical paper series* (2010).

[29] C. Mockett, M. Fuchs, and F.Thiele. "Progress in DES for wall-modelled LES of complex internal flows". In: *Computers & Fluids* 65 (Mar. 2012), pp. 44–55.

[30] C. Mockett. "A comprehensive study of detached-eddy simulation". PhD thesis. Fasanenstr. 88 (im VOLKSWAGEN-Haus), D-10623 Berlin: Von der Fakultät V- Verkehrs- und Maschinensysteme der Technischen Universität Berlin, Apr. 2009. ISBN: 978 3 7983 2159 5. URL: http://opus.kobv.de/tuberlin/volltexte/2009/2326/.

[31] M.S.Howe. *Theory of Vortex Sound*. Cambridge University Press, 2003.

[32] F. M.White. *Fluid Mechanics*. Sixth. McGraw-Hill, 2008.

[33] B. Nebenführ. "Aerodynamic and Aeroacoustic Analysis of a Multi-Element Airfoil using Hybrid RANS/LES Modeling Approaches". Licentiate Thesis. Chalmers university of technology, 2012.

[34] F. Nicoud and D. Ducros. *Subgrid-scale stress modelling based on the square of the velocity gradient tensor*. Flow, Turbulence and Combustion. Apr. 1999.

[35] N. Nikitin et al. "An approach to wall modeling in large-eddy simulations". In: *Physics of Fluids* 12.7 (July 2000). 1070-6631, pp. 1629–1632.

[36] E. N.Marieb and K. Hoehn. "Human anatomy & physiology". In: seventh. Pearson Education, Inc, 2007. Chap. 1 The human body:An orientation, p. 15.

[37] *Noise and vibration control*. Joint departments of the Army and Airforce. Headquarters, department of the army and the air force, Washington DC, May 1995.

[38] N. R. Oettle et al. "The Effects of Unsteady On-Road Flow Conditions on Cabin Noise: Spectral and Geometric Dependence". In: *SAE International. Passenger Cars-Mechanical Systems* 4.2011-01-0159 (Apr. 2011), pp. 120–130. DOI: 10.4271/2011-01-0159.

[39] A. V. Oppenheim, A. S. Willsky, and S. H. Nawab. *Signals and systems*. second. Vol. international edition. Prentice-Hall signal processing series ISBN 0-13-651175-9. Upper Saddle River, New Jersey 07458: Prentice-Hall. Inc. A Pearson Education company, 1997.

[40] W. K. Patrik Andersson. "Introduction to Sound and Vibration". In: Lecture material. unpublsihed, Oct. 2009. Chap. Lecture 1.

[41] U. Piomelli et al. "The inner-outer layer interface in large-eddy simulations with wall-layer models". In: *International Journal of Heat and Fluid flow* 24 (Aug. 2003). issue 4, pp. 538–550.

[42] A. Powell. "Lord Rayleigh's foundation of aeroacoustics". In: *The Journal of Acoustical Society of America* 98.4 (Oct. 1995), pp. 1839–1844.

[43] I. Proudman. "The Generation of Noise by Isotropic Turbulence". English. In: *Proceedings of the Royal Society of London. Series A, Mathematical and Physical Sciences* 214.1116 (1952), pp. 119–132. ISSN: 00804630. URL: http://www.jstor.org/stable/99163.

[44] O. Reynolds. "On the Dynamical Theory of Incompressible Viscous Fluids and the Determination of the Criterion". English. In: *Philosophical Transactions of the Royal Society of London. A* 186 (1895), pp. 123–164. ISSN: 02643820. URL: http://www.jstor.org/stable/90643.

[45] R.Friedrich and W.Rodi, eds. *Advances in LES of complex Flows*. Proceedings of te Euromech Colloquium 412. Munich, Germany: Kluwer Academic publishers, Oct. 2000.

[46] J. Rossiter. "Wind-Tunnel Experiments on the Flow over Rectangular Cavities at Subsonic and Transonic Speeds". In: *Aeronautical research council reports and memoranda*. 3438. Replaces R.A.E. Tech Report No.64037 -A.R.C.26 621. London:Her majesty's stationary office: Ministry of aviation, Oct. 1964.

[47] L. Råde and B. Westergren. *Mathematics Handbook for Science and Engineering, BETA*. Fourth. Studentlitteratur, Lund, 1998.

[48] M. L. Shur et al. "A hybrid RANS-LES approach with delayed-DES and wall-modelled LES capabilities". In: *International Journal of Heat and Fluid Flow* 29 (July 2008), pp. 1638–1649.

[49] J. O. Smith. *Spectral Audio Signal Processing*. online book accessed 0601. 2012. URL: http://ccrma.stanford.edu/~jos/sasp/.

[50] E. S.Oran and J. P. Boris. *Numerical simulation of reactive flow*. Second. Cambridge university press, 2001.

[51] P. R. Spalart. *Young-Person's guide to Detached-Eddy Simulation grids*. NASA/CR-2001-211032. Boeing Commercial Airplanes. Seattle Washington, July 2001.

[52] S.Sarkar and M.Y.Hussaini. *Computation of the sound generated by isotropic turbulence*. Tech. rep. Institute for Computer Applications in Science and Engineering, NASA Langley Research Center Hampton, 1993.

[53] W. Stapleford and G. Carr. *Aerodynamic Noise in Road Vehicles. 1: The Relationship Between Aerodynamic Noise and the Nature of the Airflow*. MIRA research report. 1971.

[54] *Star-CCM+ manual v.7*. CD-Adapco. 2012.

[55] J. A. Stratton. "Electromagnetic theory". In: IEEE Press Series on Electromagnetic Wave Theory. John Wiley & sons, Institute of Electrical and Electronic engineers, 2007/1941. Chap. 8.1.

[56] T. V. de Ven et al. "Computational aeroacoustic analysis of a 1/4 scale G550 Nose landing gear and comparison to NASA & UFL wind tunnel data". In: *30th AIAA Aeroacoustics Conference*. 15th AIAA/CEAS Aeroacoustic conference 2009-3359. Miami, Florida, May 2009.

[57] H. K. Versteeg and W Malalasekera. *An Introduction to COMPUTATIONAL FLUID DYNAMICS: The Finite Element Method*. Second. Pearson Education Limited, 2007.

[58] C. Wagner, T. H. ttl, and P. Sagaut, eds. *Large eddy simulations for Acoustics*. Cambridge Univeristy Press, 2007.

[59] G. Wickern and M. Brennberger. "Helmholtz Resonators Acting as Sound Source in Automotive Aeroacoustics". In: *SAE Technical Papers* 2009-01-0183 (2009). DOI: 10.4271/2009-01-0183.

[60] G. Wickern and M. Brennberger. "Scaling Laws in Automotive Aeroacoustics". In: *SAE Technical Paper* 2009-01-0180 (Apr. 2009). DOI: 10.4271/2009-01-0180.

Appendices

A Software

Main softwares used in this thesis are:

Pre-process:	ANSA version 13.2.1 by Beta CAE Systems SA, [5].
	Star-CCM+ version 6.6.11 by CD-adapco, [14].
Solver:	Star-CCM+ version 6.6.11 by CD-adapco, [14].
Post-processing:	Star-CCM+ version 6.6.11 by CD-adapco, [14].

B Pictures from simulations

Presented here are some pictures that could be of interest, but did not found their places in the results chapter. The layout will therefore be almost the same as in the results part. Their location and captions will talk for themselves.

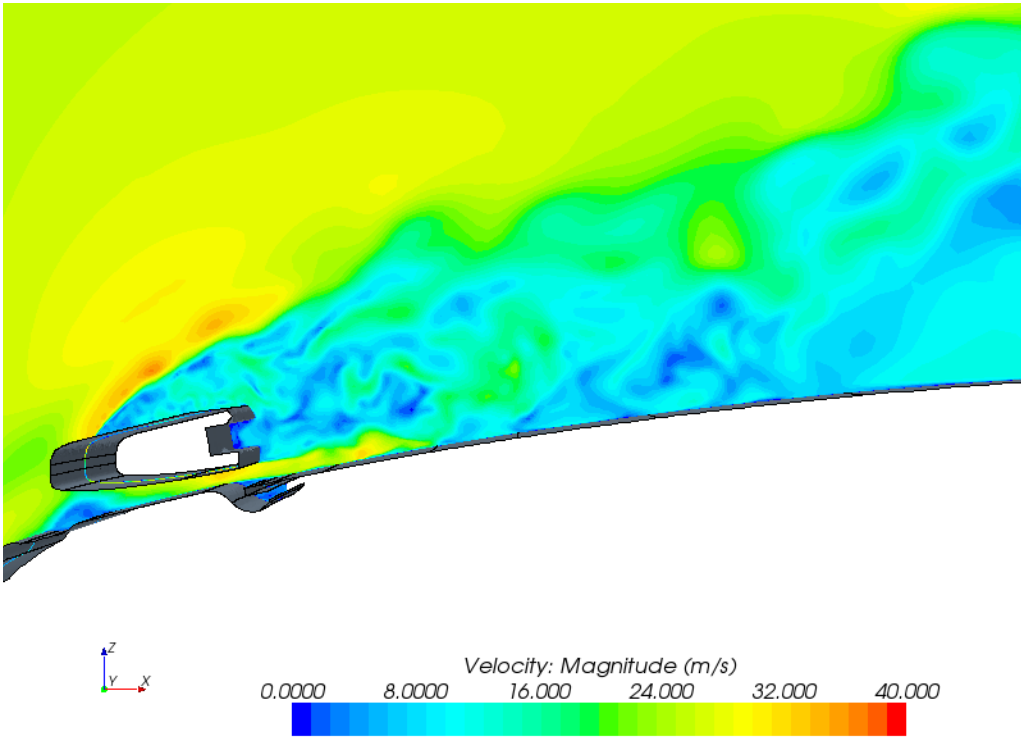

Figure B.0.1: *Velocity in mid-plane, LES-pressure outlet*

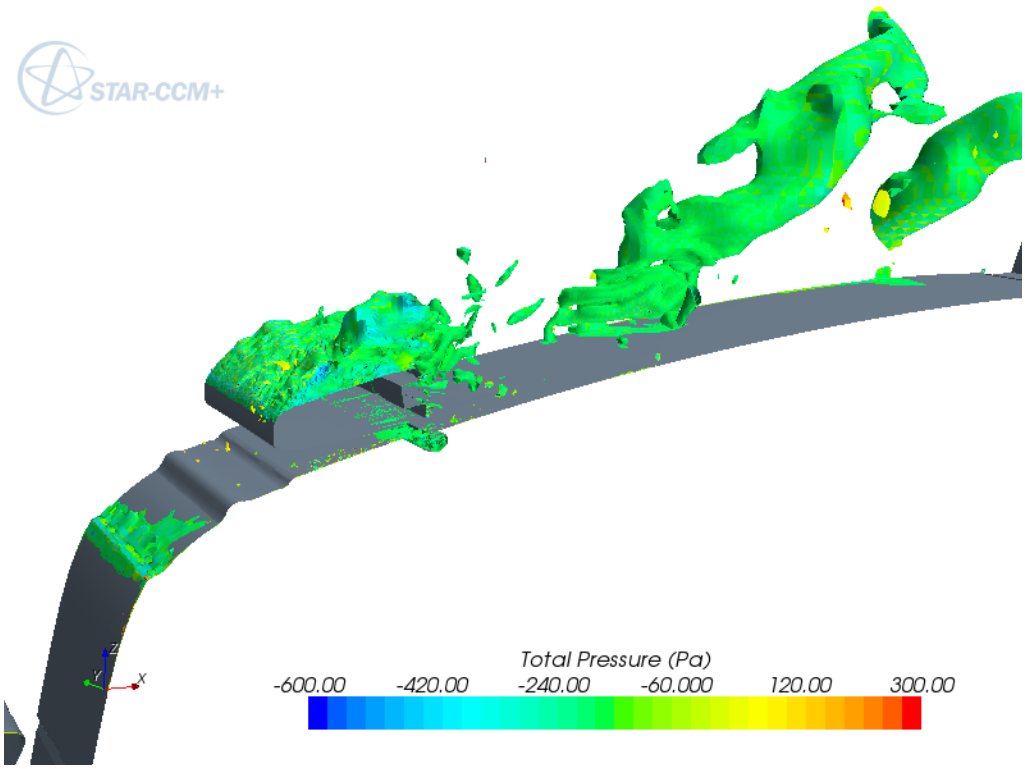

Figure B.0.2: *Total pressure on iso surfaces, LES-pressure outlet*

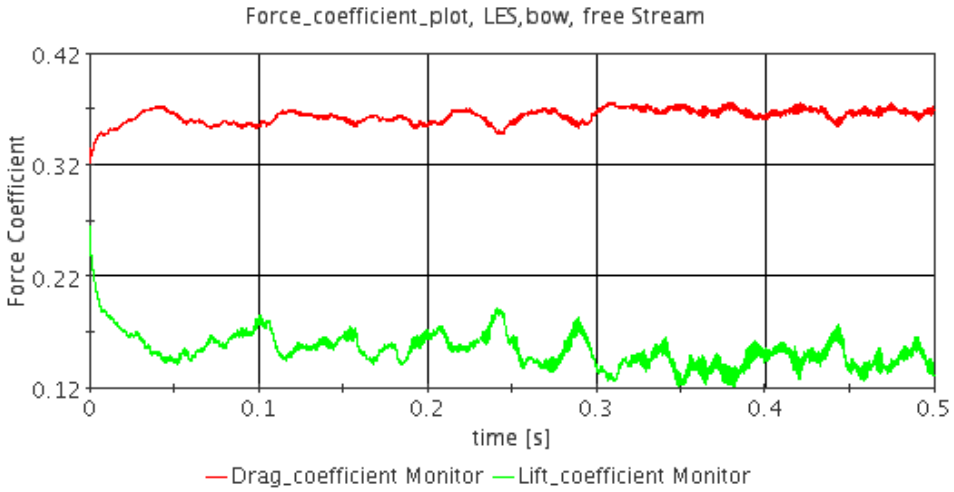

Figure B.0.3: *Force coefficients (lift and drag)*

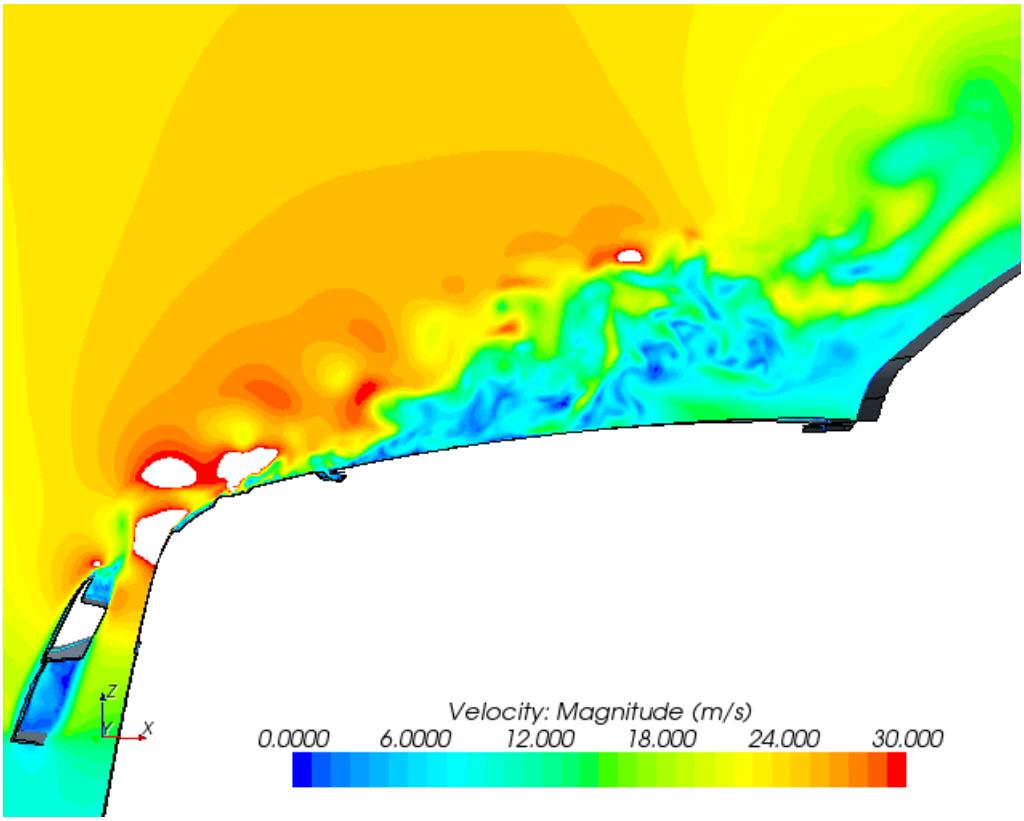

Figure B.0.4: *Velocity in mid-plane, no bow, LES-pressure outlet, please note scaling*

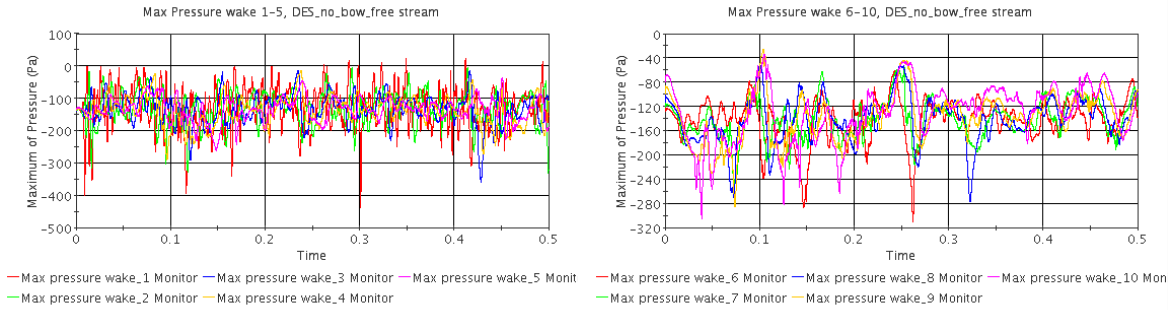

(a) wake 1-5

(b) wake 6-10

Figure B.0.5: *Pressures for wake probes (1-10) in case without bow, using DES with free stream outlet*

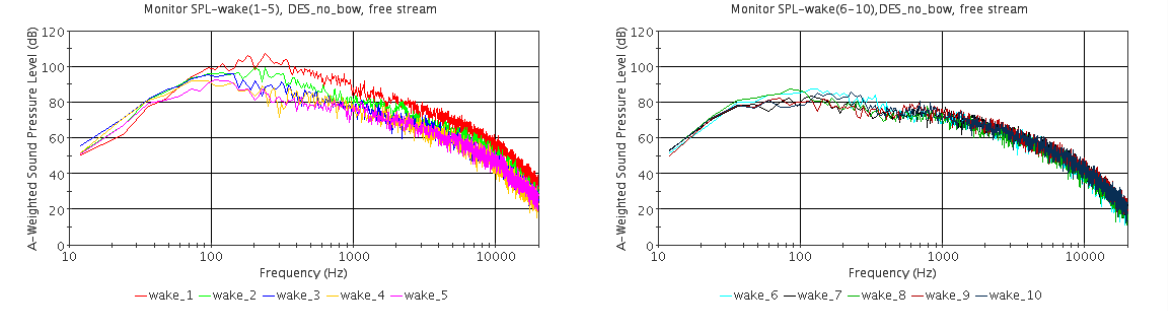

(a) wake 1-5

(b) wake 6-10

Figure B.0.6: *SPL(A-weighted) for wake probes, no bow, using DES*

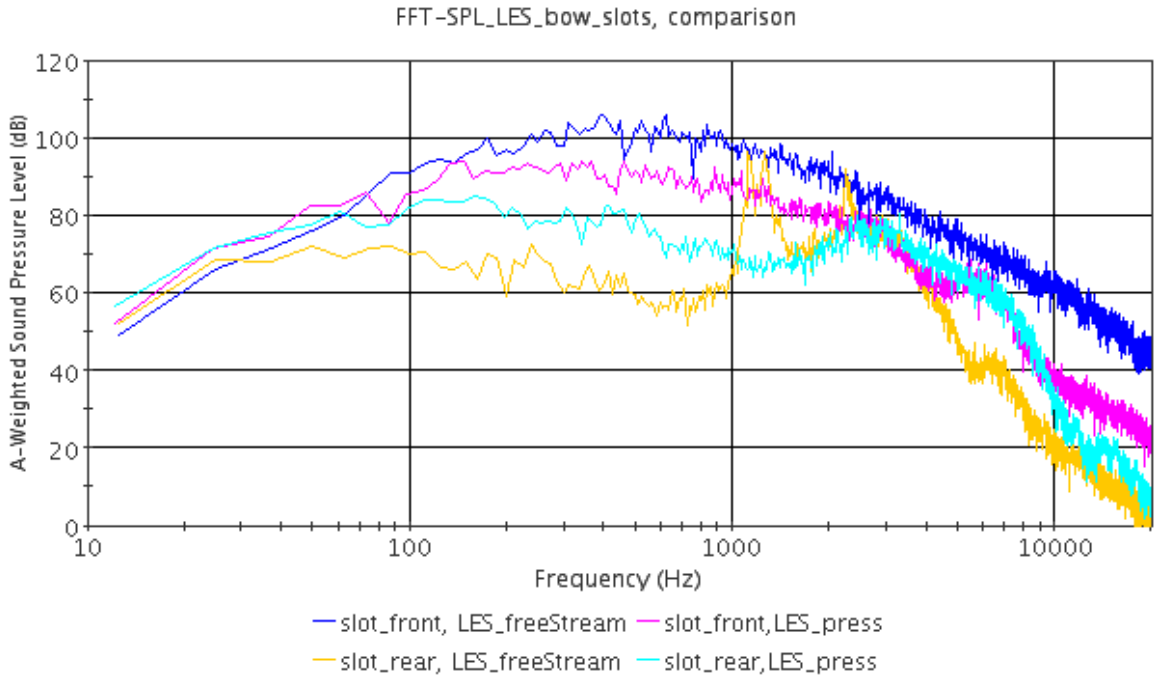

Figure B.0.7: *SPL(A-weighted) comparison between pressure- and free stream outlet in slots for case with bow, using LES*

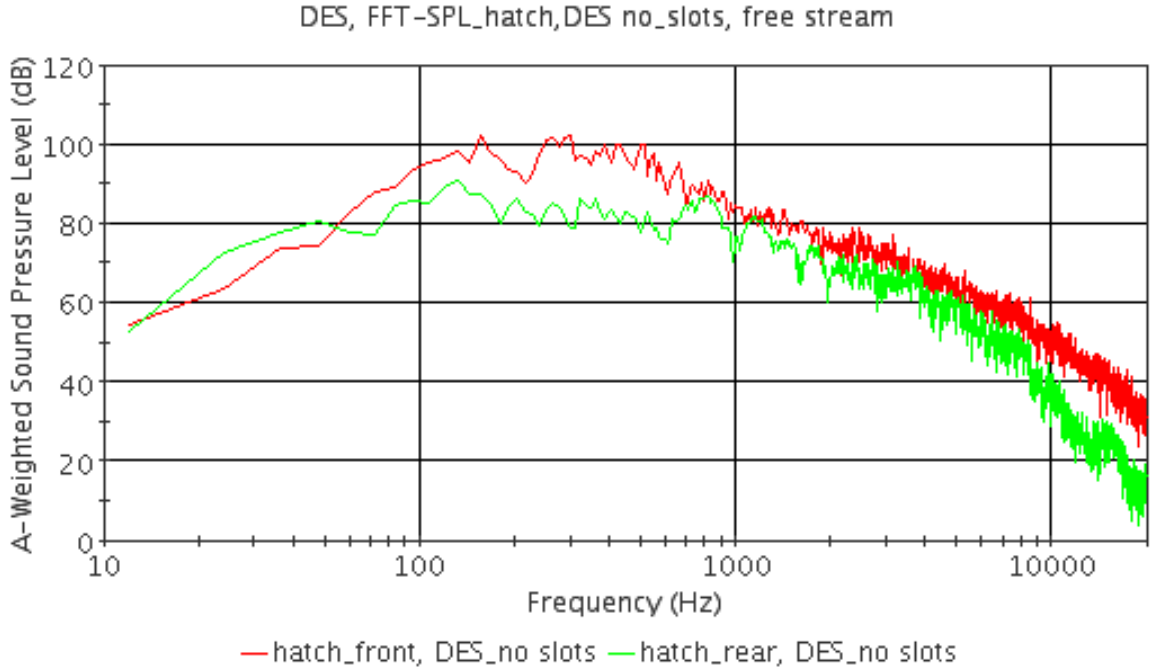

Figure B.0.8: *SPL(A-weighted) on hatch for case with bow and removed slots, using DES and free stream outlet.*

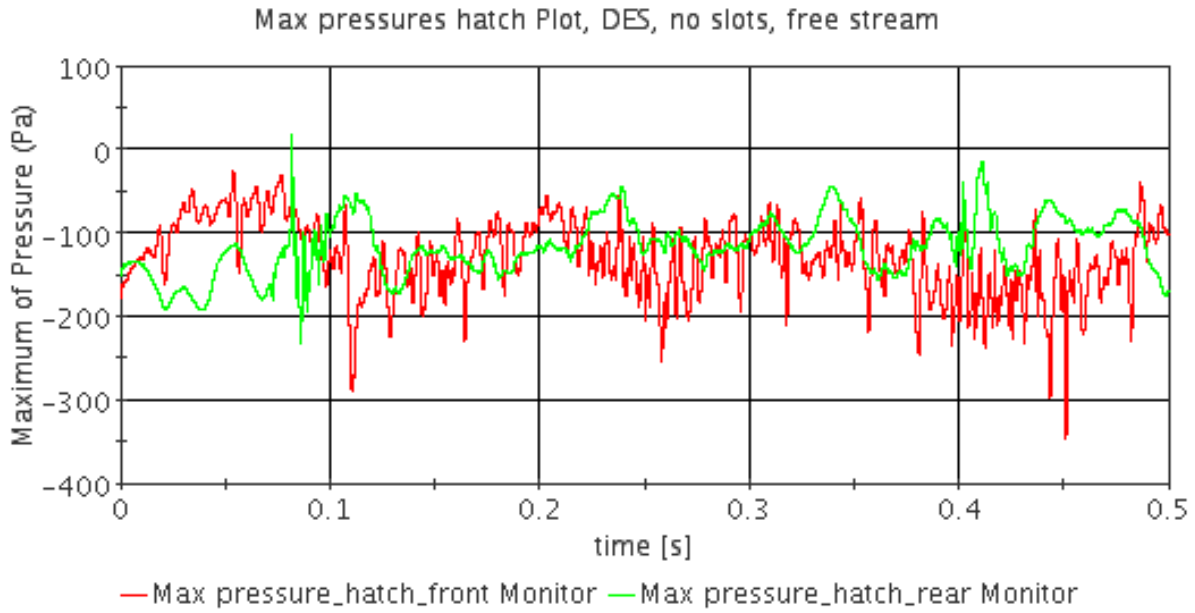

Figure B.0.9: *Pressures on hatch for case with removed slots using DES and free stream outlet*

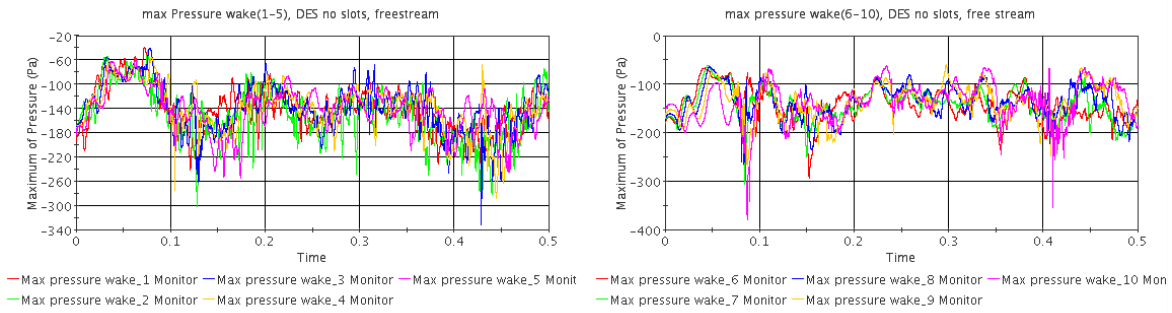

(a) wake 1-5

(b) wake 6-10

Figure B.0.10: *Pressures for wake probes (1-10) for DES with bow and removed slots*

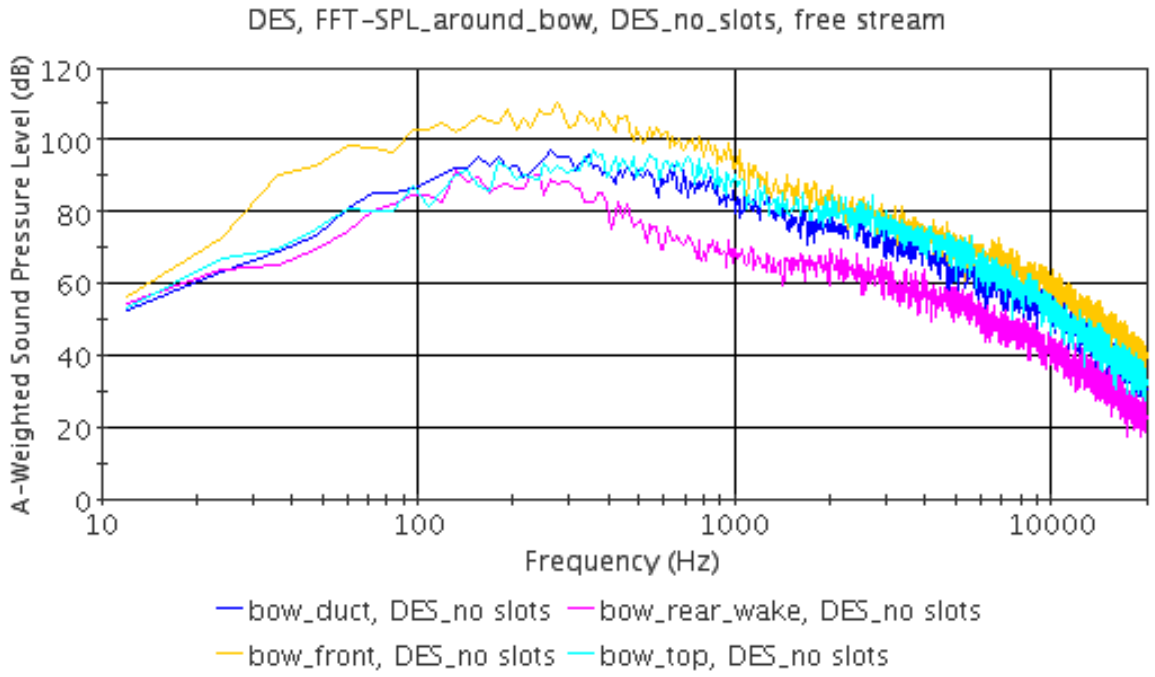

Figure B.0.11: *SPL(A-weighted) around bow for case with removed slots using DES with free stream outlet.*

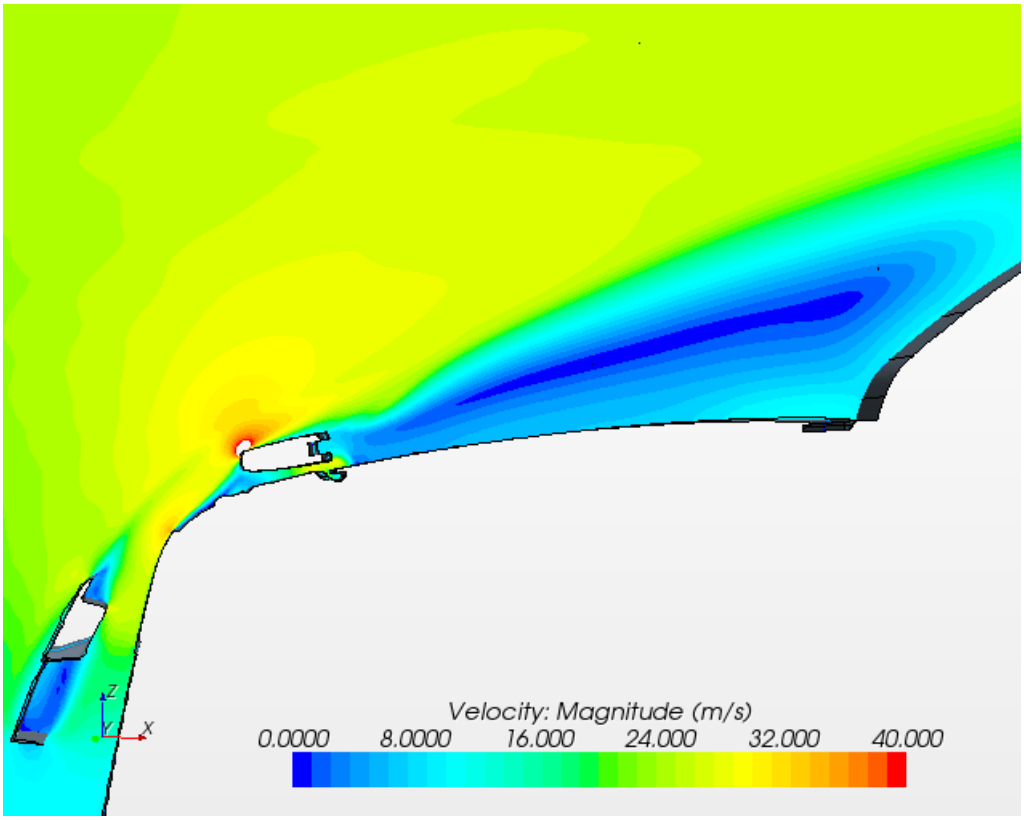

Figure B.0.12: *Velocity scene in mid-plane, using URANS with free stream outlet.*

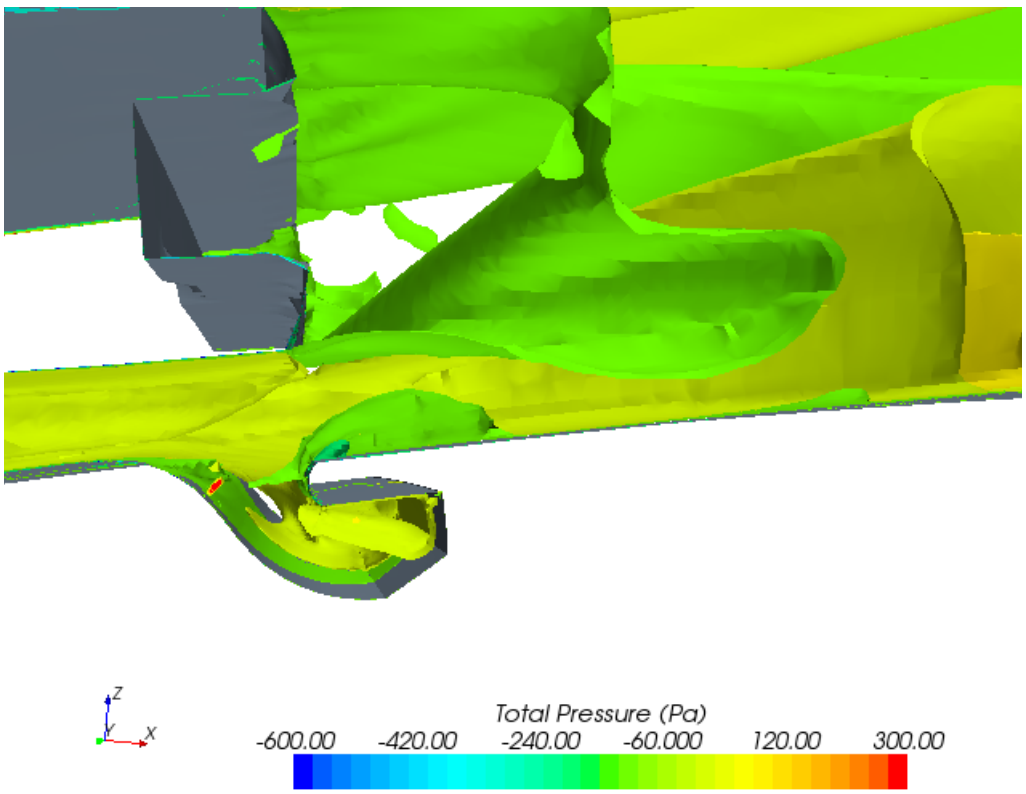

Figure B.0.13: *Total pressure scene zoomed into slot, using URANS with free stream outlet*

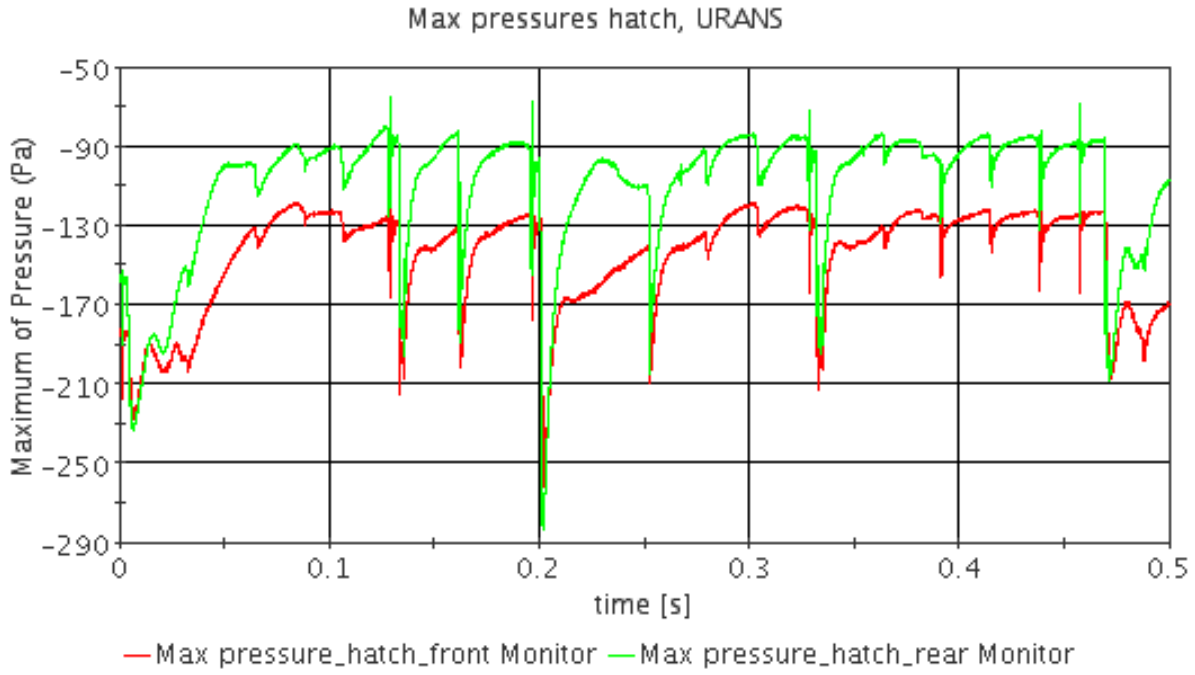

Figure B.0.14: *Pressures on hatch for case with bow, using URANS with free stream outlet.*

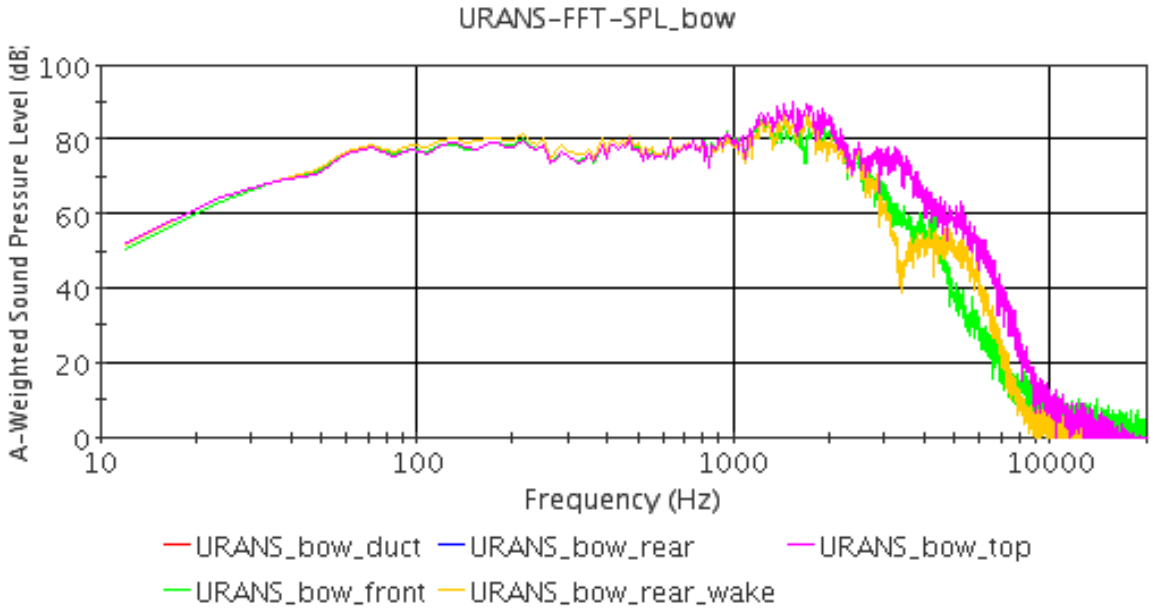

Figure B.0.15: *SPL(A-weighted) around bow for case, using URANS with free stream outlet.*

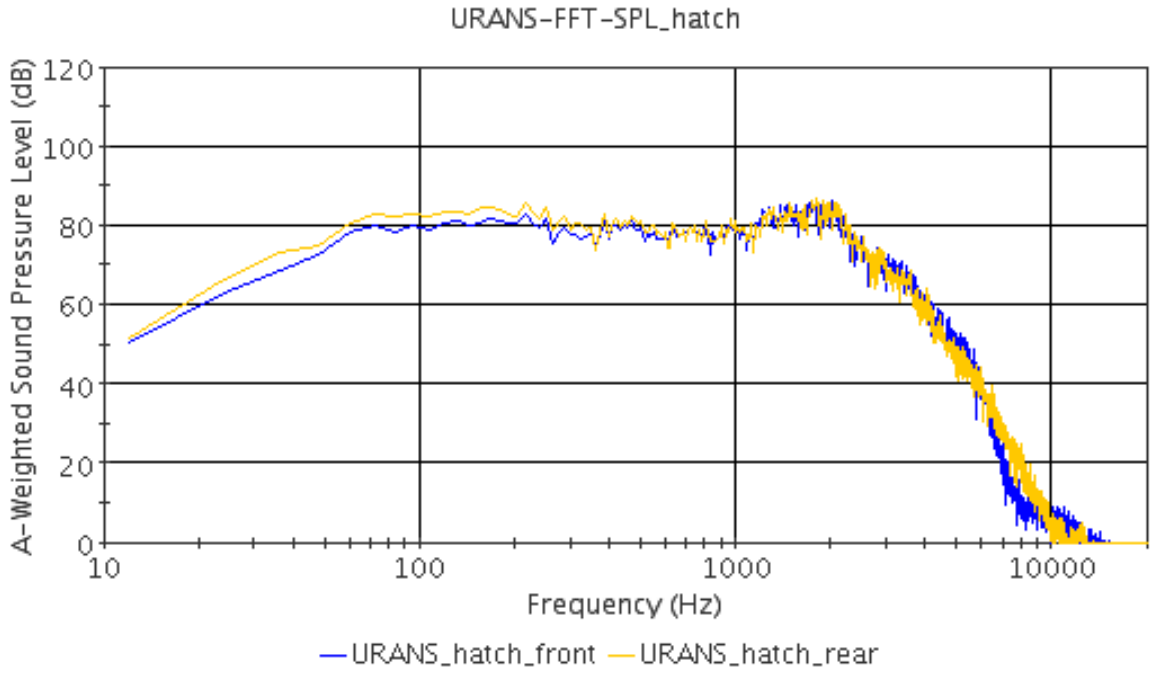

Figure B.0.16: *SPL(A-weighted) on hatch for case with bow using URANS and free stream outlet.*

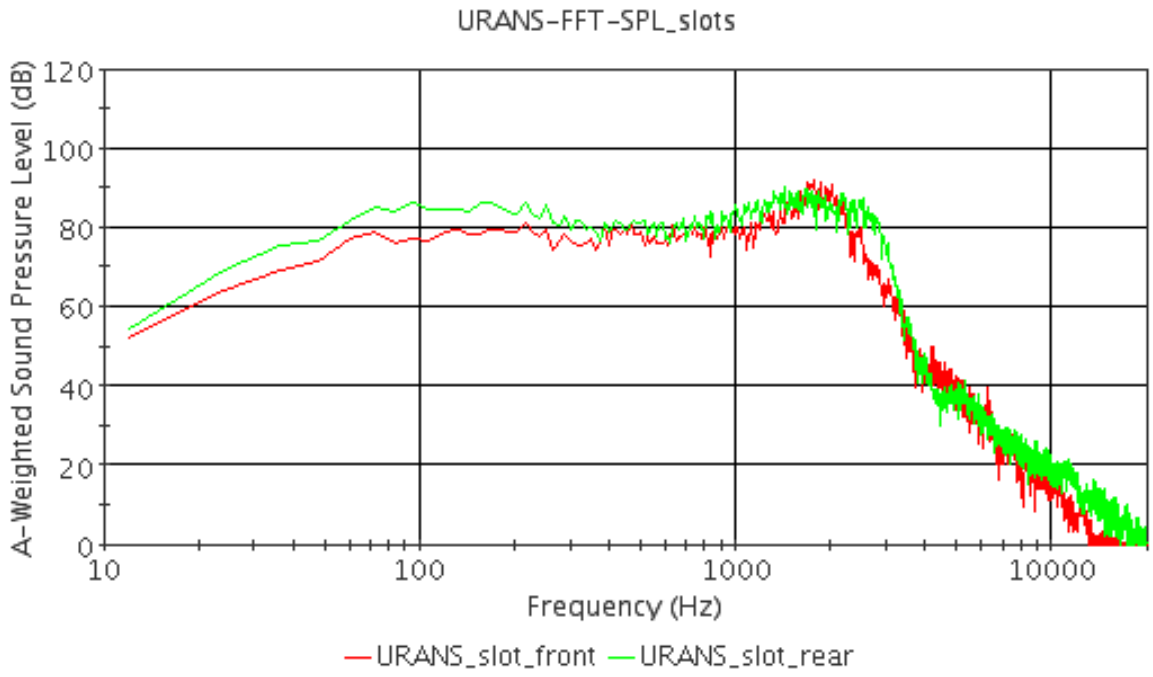

Figure B.0.17: *SPL(A-weighted) in slots for case with bow, using URANS with free stream outlet.*

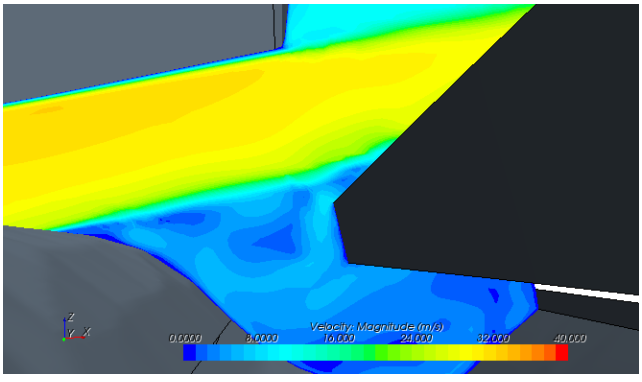

Figure B.0.18: *Vortices in front slot, LES*